

---

Doctoral Dissertations

Student Theses and Dissertations

---

Spring 2024

## Synthesis and characterization of quantum materials

Yunsheng Qiu

*Missouri University of Science and Technology*

Follow this and additional works at: [https://scholarsmine.mst.edu/doctoral\\_dissertations](https://scholarsmine.mst.edu/doctoral_dissertations)



Part of the [Condensed Matter Physics Commons](#)

Department: Physics

---

### Recommended Citation

Qiu, Yunsheng, "Synthesis and characterization of quantum materials" (2024). *Doctoral Dissertations*. 3288.

[https://scholarsmine.mst.edu/doctoral\\_dissertations/3288](https://scholarsmine.mst.edu/doctoral_dissertations/3288)

This thesis is brought to you by Scholars' Mine, a service of the Missouri S&T Library and Learning Resources. This work is protected by U. S. Copyright Law. Unauthorized use including reproduction for redistribution requires the permission of the copyright holder. For more information, please contact [scholarsmine@mst.edu](mailto:scholarsmine@mst.edu).

SYNTHESIS AND CHARACTERIZATION OF QUANTUM MATERIALS

BY

YUNSHENG QIU

A DISSERTATION

PRESENTED TO THE GRADUATE FACULTY OF THE

MISSOURI UNIVERSITY OF SCIENCE AND TECHNOLOGY

IN PARTIAL FULFILLMENT OF THE REQUIREMENTS FOR THE DEGREE

DOCTOR OF PHILOSOPHY

In

PHYSICS

2023

Approved by:

Yew San Hor, Advisor

George D. Waddill

Daniel Fischer

Aleksandr Chernatynskiy

Amitava Choudhury

© 2023

Yunsheng Qiu

All Rights Reserved

## ABSTRACT

In this study, attempts were made to grow quantum materials that have recently undergone a profound change of perspective. These materials are involved in intricate macroscopic properties rooted in the subtle nature of quantum physics. To explore our understanding of quantum materials, this study includes three projects: Magnetic Topological Insulators, Topological Superconductors, and high-temperature superconductors.

A Cr-doped  $\text{Sb}_2\text{Te}_3$  is added to the category for the magnetic topological insulators project. Their transport properties are studied, and the origin of ferromagnetism is studied. Anomalous Hall effect is observed in the Hall measurements, and several factors (cooling rate, dopant deficiency) were added in the study. The materials turned into n-type carriers were reported and explained.

For the Topological Superconductor project, Nb-doped  $\text{Bi}_2\text{Se}_3$  is added into the category, with a critical temperature of 3.4K. The combination of Topological Insulators and superconductors provides a platform for Majorana Fermions. The symbiosis of ferromagnetism and superconductivity is observed and leads to an abnormal Hall measurement. A possible qualitative mechanism is proposed for the cause.

For the high-temperature superconductor project, several new growth techniques are examined on the delafossite materials  $\text{CuAlO}_2$ . We provide new design principles on growth techniques that would enable the development of transparent conductors.

## ACKNOWLEDGMENTS

I want to thank my research advisor, Dr. Yew San Hor, for his invaluable patience and guidance in supporting my studies and research. I appreciate his rigor-quality-control attitude and bitter discipline to bring me in line with the scientific world. Working with him has been a great learning experience, and his philosophy helped foster a morally sound value in my young mind. Not only did he show me the necessary skills and correct solutions over the past years, but he also prepared me for future obstacles and challenges.

I am also grateful to my other Ph.D. committee members, Dr. George D. Waddill, Dr. Daniel Fischer, Dr. Aleksandr Chernatynskiy, and Dr. Amitava Choudhury, for their time reviewing my work and for their support in sorting out my confusion in a time of need.

Special thanks to Mr. Ronald Woody and Mr. Fred Eickelmann for all their professional technical support and relentless kindness during this study period. Their mechanical skills and knowledge put irreplaceable significance in my research.

Finally, I extend my gratitude to all my colleagues at S&T, who have made my graduate-student life experiment richer. And last but not least, I am deeply grateful to all S&T faculty members for their countless efforts and support that have built up this salutary environment in Rolla.

## TABLE OF CONTENTS

	Page
ABSTRACT.....	iii
ACKNOWLEDGMENTS .....	iv
LIST OF ILLUSTRATIONS .....	viii
LIST OF TABLES .....	xi
NOMENCLATURE .....	xii
 SECTION	
1. INTRODUCTION .....	1
1.1. HISTORY OF TOPOLOGICAL INSULATORS .....	1
1.2. TOPOLOGICAL INSULATORS PROPERTIES .....	2
1.2.1. Bulk and Surface State .....	3
1.2.2. Spin-Orbit Coupling .....	5
1.2.3. Quantum Spin Hall Effect .....	6
1.2.4. 3D Strong Topological Insulators .....	8
1.3. DISSERTATION OUTLINE .....	9
2. EXPERIMENTAL METHODS.....	10
2.1. CRYSTAL GROWTH METHODS .....	10
2.1.1. Modified Bridgeman Method (MB) .....	10
2.1.2. I <sub>2</sub> -mediated Chemical Vapor Transport .....	12
2.1.3. Pressure Seal Swagelok.....	13
2.1.4. Double-Seal Ampoule .....	14

2.2. MEASUREMENT METHODS.....	16
2.2.1. Scanning Tunneling Microscope (STM).....	16
2.2.2. X-Ray Powder Diffraction (XRD).....	19
2.2.3. Angle-Resolved Photoemission Spectroscopy (ARPES).....	23
2.2.4. Physical Properties Measurements Systems (PPMS).....	25
2.2.4.1. AC/DC magnetization.....	27
2.2.4.2. Resistivity measurement.....	30
2.2.4.3. Hall measurement.....	31
3. MAGNETIC TOPOLOGICAL INSULATORS.....	33
3.1. BREAKING TIME-REVERSAL SYMMETRY.....	34
3.2. ANOMALOUS HALL EFFECT.....	36
3.3. QUANTUM ANOMALOUS HALL EFFECT (QAHE).....	38
3.3.1. The Quantum Hall Effect (QHE).....	38
3.3.2. Quantum Spin Hall Effect (QSH).....	39
3.3.3. Realization of QAHE.....	40
3.4. MAGNETIZATION ANALYSIS.....	41
3.5. HALL EFFECT ANALYSIS.....	47
4. TOPOLOGICAL SUPERCONDUCTORS.....	55
4.1. MAJORANA FERMION.....	55
4.2. SUPERCONDUCTIVITY.....	56
4.2.1. Meissner Effect.....	56
4.2.2. Type II Superconductor.....	57
4.2.3. P-wave Superconductivity.....	58

4.2.4. Experiment Confirmation.....	59
4.3. SURFACE STATE.....	61
4.4. MAGNETIZATION.....	63
4.4.1. AC Meissner Effect.....	63
4.4.2. Ferromagnetic-like Order.....	65
4.5. HALL MEASUREMENT.....	69
5. HIGH TEMPERATURE SUPERCONDUCTORS.....	77
5.1. CuO <sub>2</sub> PLANE.....	77
5.1.1. Mott Insulator.....	78
5.1.2. Experiment Frontier.....	79
5.2. HOLE DOPING.....	79
5.3. DELAFOSSITE OXIDE.....	81
5.4. SOLID STATE REACTION.....	82
5.5. PRESSURE-SEAL SWAGELOK.....	84
5.6. DOUBLE-SEAL AMPOULE.....	85
5.7. CRYSTAL THERMAL TRANSPORT.....	87
6. CONCLUSIONS.....	90
6.1. MAGNETIC TOPOLOGICAL INSULATOR PROJECT.....	90
6.2. TOPOLOGICAL SUPERCONDUCTING PROJECT.....	91
6.3. HIGH TC SUPERCONDUCTOR PROJECT.....	92
BIBLIOGRAPHY.....	95
VITA.....	108

## LIST OF ILLUSTRATIONS

	Page
Figure 1-1 Sketch for Topological Insulator.....	2
Figure 1-2 Illustration of E-k diagram for Bulk state and Surface state.....	3
Figure 1-3 Illustration for Band inversion .....	4
Figure 1-4 Quantum Spin Hall effect on Graphene .....	6
Figure 1-5 Quantum Spin Hall effect on Magnetic topological insulators.....	7
Figure 2-1 Schematic picture of the Bridgman method.....	11
Figure 2-2 Schematic picture of the Modified Bridgman method.....	11
Figure 2-3 Schematic picture of the I <sub>2</sub> -mediated Chemical Vapor Transport .....	12
Figure 2-4 Picture of Swagelok method .....	14
Figure 2-5 Sketch and picture of the Double-Seal ampoule.....	15
Figure 2-6 Schematic of Scanning tunneling microscopy .....	16
Figure 2-7 Tunneling current approximation.....	17
Figure 2-8 STM image for Nb <sub>0.25</sub> Bi <sub>2</sub> Se <sub>3</sub> .....	19
Figure 2-9 Sketch of the X-ray diffractometer .....	20
Figure 2-10 XRD results for Nb <sub>0.25</sub> Bi <sub>2</sub> Se <sub>3</sub> .....	22
Figure 2-11 XRD results for Cr-doped Sb <sub>2</sub> Te <sub>3</sub> .....	23
Figure 2-12 XRD results for CuAlO <sub>2</sub> .....	23
Figure 2-13 Sketch of ARPES .....	24
Figure 2-14 Sketch of the PPME cooling Dewar.....	26
Figure 2-15 Sketch of PPMS .....	27

Figure 2-16 Schematic AC mode.....	28
Figure 2-17 Schematic DC mode.....	29
Figure 2-18 Sketch of a 4-probe sample puck .....	30
Figure 2-19 Sketch of 5-probe sample puck .....	32
Figure 3-1 Comparison of RKKY and BR mechanisms.....	34
Figure 3-2 Massive Dirac Fermions by Magnetic Interaction .....	35
Figure 3-3 Intrinsic deflection effect, side jump effect, and skew scattering effect .....	38
Figure 3-4 Comparison of AHE, SHE, and QAHE .....	41
Figure 3-5 Samples of $\text{Cr}_{0.2}\text{Sb}_2\text{Te}_3$ .....	42
Figure 3-6 $M_{\text{DC}}$ vs T for $\text{Cr}_{0.2}\text{Bi}_2\text{Te}_3$ .....	43
Figure 3-7 $1/X_{\text{mol}}$ for phase transition around 35K.....	43
Figure 3-8 $1/X_{\text{mol}}$ Comparison of $\text{Cr}_{0.2}\text{Sb}_2\text{Te}_3$ and $\text{Cr}_{0.2}\text{Sb}_2\text{Te}_{2.9}$ .....	45
Figure 3-9 DC magnetization for $\text{Cr}_{0.22}\text{Sb}_2\text{Te}_3$ .....	46
Figure 3-10 Magnetic hysteresis for $\text{Cr}_x\text{Sb}_2\text{Te}_3$ with different Cr concentrations.....	47
Figure 3-11 Anomalous Hall effect for $\text{Cr}_{0.2}\text{Sb}_2\text{Te}_3$ .....	48
Figure 3-12 Resistivity comparison For $\text{Cr}_{0.2}\text{Sb}_2\text{Te}_3$ and $\text{Cr}_{0.2}\text{Sb}_2\text{Te}_{2.9}$ .....	49
Figure 3-13 Hall resistance .....	50
Figure 3-14 Carrier density for $\text{Cr}_{0.2}\text{Sb}_2\text{Te}_{3/2.9}$ .....	52
Figure 4-1 Magnet Flux model for Meissner effect.....	57
Figure 4-2 Comparison of Type-I and Type-II superconductors .....	58
Figure 4-3 Resistivity vs Temperature at zero magnetic fields for $\text{Nb}_{0.25}\text{Bi}_2\text{Se}_3$ .....	59
Figure 4-4 Resistivity vs Magnetic field at 2K for $\text{Nb}_{0.25}\text{Bi}_2\text{Se}_3$ . .....	60
Figure 4-5 ARPES result for TSC .....	62

Figure 4-6 AC magnetization for $\text{Nb}_{0.25}\text{Bi}_2\text{Se}_3$ with FC and ZFC.....	64
Figure 4-7 AC magnetization for $\text{Nb}_{0.25}\text{Bi}_2\text{Se}_3$ with 2-step growth method.....	64
Figure 4-8 DC magnetization for $\text{Nb}_{0.25}\text{Bi}_2\text{Se}_3$ .....	65
Figure 4-9 Magnetic field loop treatment .....	66
Figure 4-10 Total magnetic moment for $\text{Nb}_{0.25}\text{Bi}_2\text{Se}_3$ .....	67
Figure 4-11 The cause of ferromagnetic moment.....	68
Figure 4-12 Hall resistivity for $\text{Nb}_{0.25}\text{Bi}_2\text{Se}_3$ .....	70
Figure 4-13 Refined Hall resistivity for $\text{Nb}_{0.25}\text{Bi}_2\text{Se}_3$ .....	71
Figure 4-14 Mean-field phase diagram for $\text{Nb}_{0.25}\text{Bi}_2\text{Se}_3$ .....	72
Figure 4-15 Hall voltage comparison with $\text{NbSe}_2$ .....	73
Figure 4-16 Refined Hall voltage comparison.....	74
Figure 4-17 Schematic for the cause of non-zero Hall voltage .....	75
Figure 5-1 Schematic picture for Parent Mott insulator with $\text{CuO}_2$ plane .....	78
Figure 5-2 Sketch for hole doping effect on Parent Mott insulator .....	80
Figure 5-3 Results of Traditional Solid-State Reaction.....	83
Figure 5-4 Results of Pressure-Seal Swagelok.....	84
Figure 5-5 Picture of the open ampoule.....	86
Figure 5-6 Crystals of $\text{CuAlO}_2$ .....	86
Figure 5-7 Crystals of $\text{CuAlO}_2$ after second sintering.....	87
Figure 5-8 Results after Crystal Thermal Transport.....	88
Figure 5-9 Zoomed Crystal Thermal Transport results .....	89

**LIST OF TABLES**

	Page
Table 3-1 linear fitting for different cooling speed .....	44
Table 3-2 linear fitting for different Te concentration .....	46
Table 6-1 Comparison of used methods .....	94

**NOMENCLATURE**

Symbol	Description
$e$	Elementary Charge
$c$	Speed of Light in Vacuum
$h$	Planck Constant
$\hbar$	Reduced Planck Constant
$m_e$	Electron Mass
$\mu_B$	Bohr Magnetron
$k_B$	Boltzmann Constant

# 1. INTRODUCTION

## 1.1. HISTORY OF TOPOLOGICAL INSULATORS

In condensed matters, intentional doping impurities into materials is one of the most reliable methods to manipulate their structural, electronic, and mechanical properties. The effects of doping were long known as empirically unpredictable. As we have more understanding of the laws of nature, the doped effect on materials becomes more predictable and with confirmed changes in properties, the theories for the laws of nature can be verified and renovated. For example, the story of the Topological Superconductor discovery [1]. The first 3D topological insulator model was proposed in 1985 [2] and its feasible solution using binary compounds involving bismuth and selenium was proposed in 2007, [3] and experimentally realized and confirmed in 2008 [4] [5]. As more candidates for 3D topological insulator was discovered, intentional doping transition elements into these new materials starts to shed light on their potential. By doping Cu intercalated in van der Waals quintuple layers of  $\text{Bi}_2\text{Se}_3$ , the doped materials show superconductivity with a critical temperature of 3.4K and a connection between the superconductor and topological insulator comes on stage with no warning.

The study of the Topological Insulator is of great interest in physics. With numerical successful doping reports [6] [7], this material is then evolved into Magnetic Topological Insulators, Topological Superconductors, Weyl semimetals, Dirac Semimetals, etc. The topological band theory has been proposed and confronted by experimental reports. From a research perspective, doping impurities into topological materials have no doubts will benefit the condensed matter physics field.

## 1.2. TOPOLOGICAL INSULATORS PROPERTIES

In the rapid development of science and technology, Topological Insulators (TI) have driven great interest in the field of condensed matter physics. The TI has the QSH state at room temperature and a non-trivial band structure and this new phase of matter inevitably leads to the upsurge in condensed matter physics research. [8]

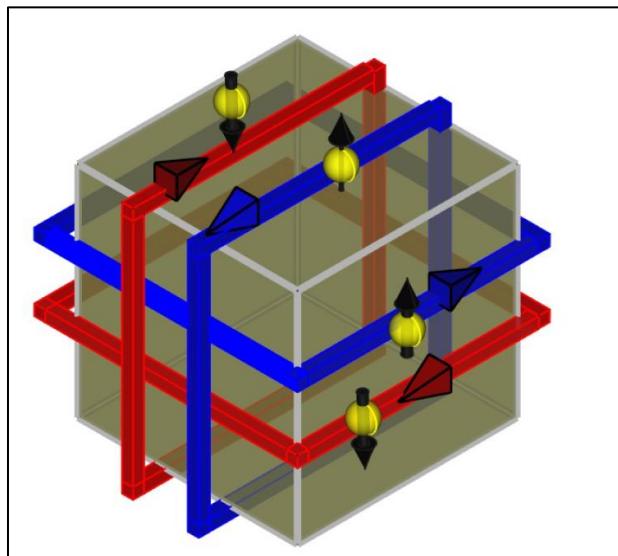


Figure 1-1 Sketch for Topological Insulator

In band theory, solid materials are classified into three categories based on their conductivity: conductor, insulator, and semiconductor. When the gap between the conduction band and valence band is wide, materials are insulators, because electrons cannot absorb enough energy to cross the gap and move freely. And when there is no gap, free electrons (or holes) can move without crossing the band gap and the material is now a conductor. The band gap of the semiconductor is between the conductor and the insulator. Under certain modifications (doping or gating), a semiconductor can be

changing its valence band status and have variable electrical conductivity. However, TI cannot be simply classified in the categories above. As shown in Figure 1-1, an ideal TI would have an insulating bulk, while its surface is conducting with currents that have spin-momentum locking.

**1.2.1. Bulk and Surface State.** In Topological Insulators, the surface and the bulk of the sample have different band structure. As shown in Figure 1-2, in the bulk state, there is a band gap between the conduction band and valence band, which restricts any free electrons to carry any current. The bulk of an ideal TI would be a perfect insulator. However, the surface of TI is conductive, with a gapless metallic surface state. This special surface state is formed due to its internal strong spin-orbit coupling and possesses time-reversal symmetry. [9].

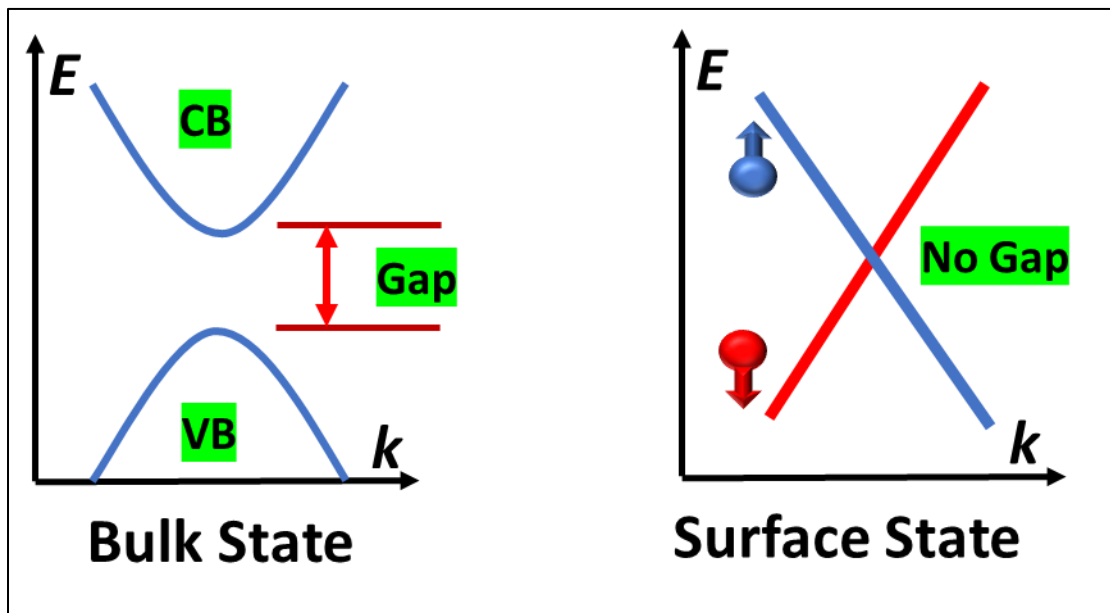


Figure 1-2 Illustration of E-k diagram for Bulk state and Surface state

It is noted that this gapless surface state distinguished itself from regular conductor band structure and obey the linear Dirac equation [10]. The Dirac equation is a relativities quantum mechanical equation for elementary spin  $\frac{1}{2}$  particle. Modified the Dirac equation with the  $Z_2$  index [11], a series of solutions were solved to predict the physics property on this surface state, including the linear energy dispersion relationship near the Dirac point. In the 2D example, the eigenstates for spin-up and spin-down electrons are found to have opposite momentum directions, as the system is protected by time-reversal symmetry, these two states form a pair of helical edge states that can be used to describe the quantum spin hall effect. Nonetheless, in 3D examples, the linear dispersion relations have rotational symmetry and form a Dirac cone. These predictions have been experimentally observed using APRES in the  $\text{Bi}_{1-x}\text{Sb}_x$ , and  $\text{Bi}_2\text{Se}_3$  [12] systems and now serve as the validation for topological materials.

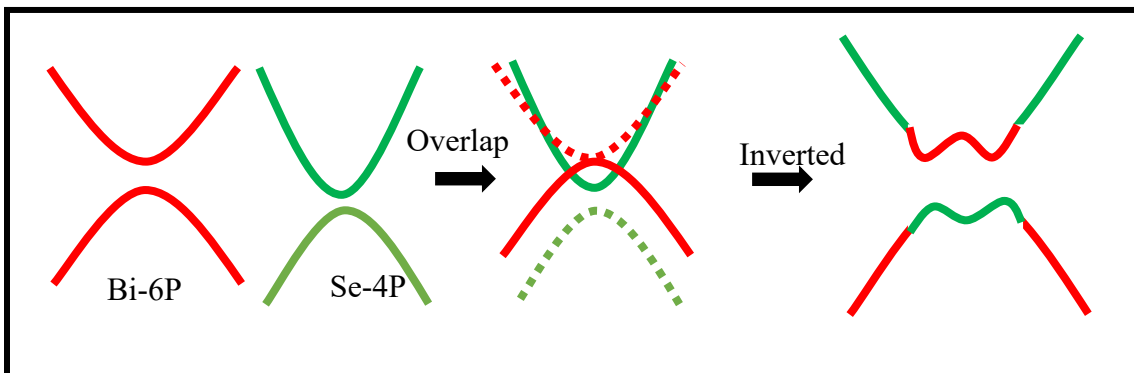


Figure 1-3 Illustration for Band inversion

Band inversion is a crucial ingredient for the non-trivial surface state. [13]Figure 1-3 shows the sketch for band inversion in  $\text{Bi}_2\text{Se}_3$ -like materials. The orbital contributions from the Bi atoms (6P orbit bands) and Se atoms (4P orbit bands) form a

mixed state with lattice distortion. The hybridization [14] of the atomic orbitals aligned the bands and gave rise to the band inversion while a gap remained open after the alignment.

It has been argued that this band inversion is insufficient to have a topological insulator [15], for it is possible to witness band inversion in materials with low spin-orbit coupling energy. Furthermore, the band inversion is caused by a couple of factors: (i) scalar relativistic effect such as mass velocity and Darwin terms and (ii) lattice distortion in the crystals. Moreover, this non-trivial surface state would also require the occurrence of Spin-Orbit coupling.

**1.2.2. Spin-Orbit Coupling.** The interaction between electron's spin and the nuclei's orbits is called the Spin-orbit coupling. This interaction starts with the effective magnetic moment of electron as it circles around the nucleus orbits. The strength of Spin-Orbit Coupling (SOC) can be represented by the SOC Hamiltonians. The total interaction energy of spin-orbit coupling takes the form of the sum of Larmor interaction energy and Thomas Interaction energy. Their result for the spin-orbit coupling energy of an electron in a central field with potential  $U(r)$  is shown below: [16]:

$$\Delta H \equiv \Delta H_L + \Delta H_T \equiv \frac{\mu_B}{\hbar m_e c^2} \frac{1}{r} \frac{\partial U(r)}{\partial r} \mathbf{L} \cdot \mathbf{S} \quad (1)$$

where  $L$  is the orbital angular momentum and  $S$  is the spin.

A direct consequence of the spin-orbit coupling is the Anomalous Zeeman splitting pattern [8]. Note that the size of the energy splitting is different for the different orbitals, and it increases rapidly with the angular momentum quantum number  $l$ . In heavy atoms (large  $Z$ ), SOC becomes non-negligible and plays an essential role in the Quantum spin hall effect and TI.

**1.2.3. Quantum Spin Hall Effect.** Two decades ago, a new class of quantum states emerged, called Quantum Spin Hall (QSH) states. This new state characterized itself with pairs of helical edge states that carry spin currents perpendicular to an applied electric field. Time-reversal symmetry plays an important role in the dynamics of the helical edge states, and it leads to the  $Z_2$  classification of the QSH state [17].

Whereas the QSH state shares many similarities with the QH state, it differs in important ways. [18] The QH effect occurs when a strong magnetic field is applied to a 2D gas of electrons, and the system has two degrees of freedom (spin and momentum) by the indicated forward and backward arrow. The QSH effect occurs when the strong spin-orbit coupling forms the spin currents, and the systems lose one degree of freedom (spin) due to time-reversal symmetry.

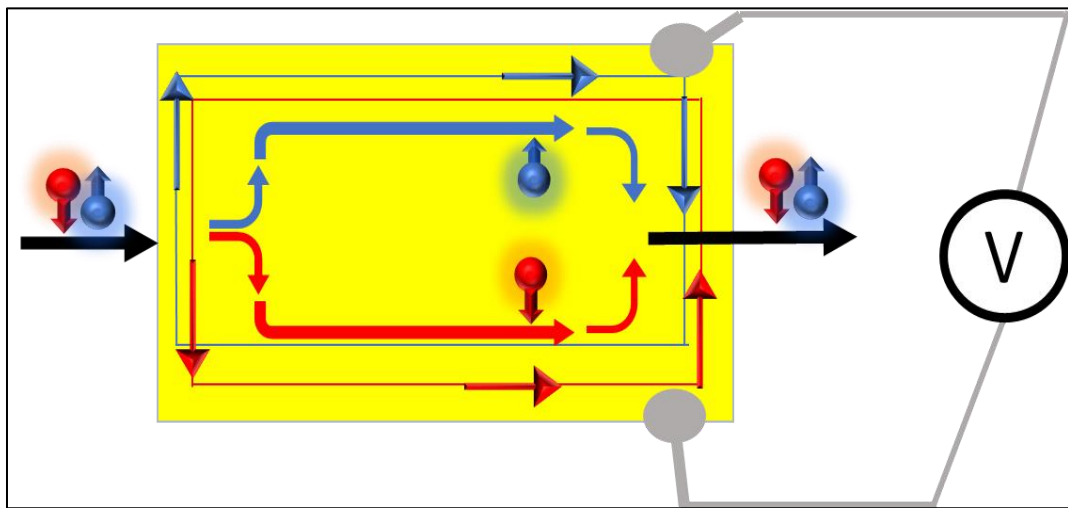


Figure 1-4 Quantum Spin Hall effect on Graphene

QSH was initially proposed in graphene [19] but was later experimentally realized in Topological Insulators through strong spin-orbit coupling [20]. However, the concept

of this experimental detection triggers an intense theoretical debate. In this section, I agree to use Zhang's claim and support the experimental evidence from HgTe/CdTe [20] while some scientists may remain skeptical.

As shown in Figure 1-4, when the Hall voltage of the materials with QSH state is measured with a voltmeter, there will be a non-measurable Hall voltage difference. However, the applied current will experience a "spin-filter" effect. This effect will cause the spin-up and spin-down electrons to take different paths on the material, and the spins of the Hall voltage contact sites will be opposite.

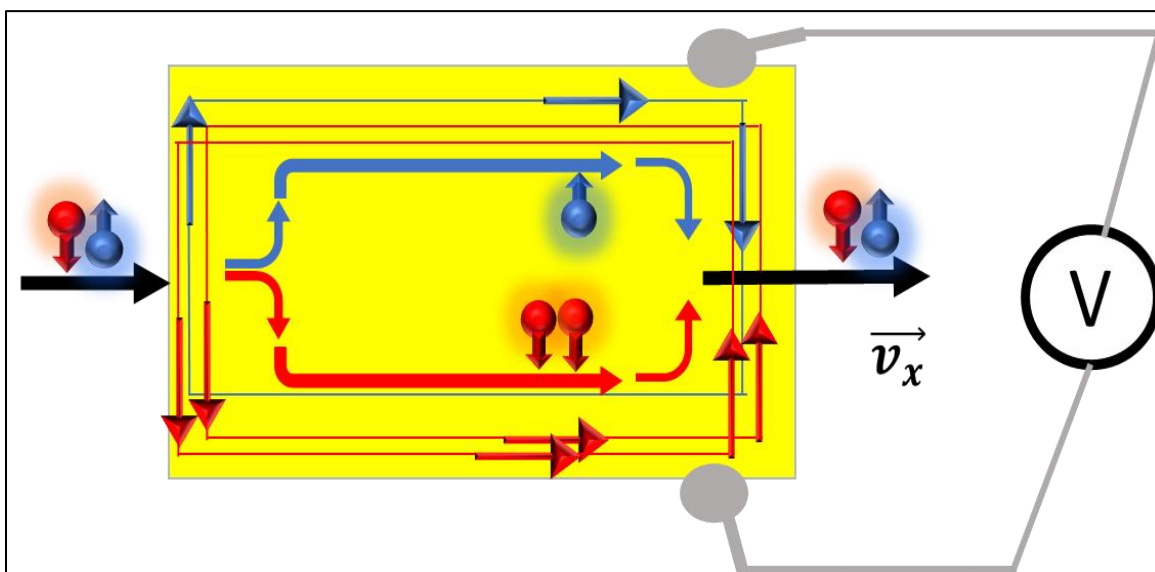


Figure 1-5 Quantum Spin Hall effect on Magnetic topological insulators

To confirm the existence of the QSH effect, Zhang proposes an experimental approach using Magnetic Topological Insulators. The spin-up and spin-down electrons in the applied current will have a numerical difference with magnetic impurity doped. As

the Hall voltage is measured, this numerical difference can cause a non-zero Hall voltage, as shown in Figure 1-5.

**1.2.4. 3D Strong Topological Insulators.** The development of the Topological Insulators is rapid, and it began with the two-dimensional(2D) topological state, which is theoretically derived from the 2D graphene materials. The first generation of 3D Topological Insulators was  $\text{Bi}_{1-x}\text{Sb}_x$  binary alloy ( $x=0.07\sim 0.22$ ). The ratio  $x$  requires fine-tuning because the chemical property of such an alloy is unstable. Despite it being the first Topological Insulators confirmed with ARPES, the gap between the conduction band ( $\sim 10\text{meV}$ ) and valence band in its bulk state is narrow, and the Fermi level intersects multiple times in its surface state. [21] Hence, scientists must find other optimized Topological Insulators.

The second generation of TI, including  $\text{Bi}_2\text{Se}_3$ ,  $\text{Bi}_2\text{Te}_3$ , and  $\text{Sb}_2\text{Te}_3$ , was proposed. These  $\text{V}_2\text{VI}_3$  compounds' single crystals all belong to the group  $R\bar{3}M$ . They were first studied for their thermoelectric effect [22] and is known for their excellent chemical stability in laboratory condition. The band gap for the second generation of TI is much wider (up to  $300\text{meV}$ ) and makes them more suitable for research and application. Additionally, the bulk and surface electronic structure for  $\text{Bi}_2\text{Se}_3$  and  $\text{Bi}_2\text{Te}_3$  has been experimentally confirmed to their theoretical prediction and numeric cases of doping results have been established to prove research value. 3D Topological Insulators are robust to disorder scattering through extensive numerical calculations. [23]

By being crystalline insulators, 3D Topological Insulators has 6 conducting surfaces compared to the two conducting surfaces in 2D TI, a-second order classification

for 3D TI has been proposed and theoretically established. [24] As the classification system is still under development, a general introduction will require further research.

### **1.3. DISSERTATION OUTLINE**

With the basic understanding of Topological Insulators, in this dissertation, the experimental methods used in this dissertation will be introduced. Crystal growth methods and measurement methods are laid out in schematic details.

Subsequently, three individual projects were reported in this study. Started with extra background information on their topics and followed by the discoveries and results.

In the end, a summary for each project will be concluded.

## 2. EXPERIMENTAL METHODS

### 2.1. CRYSTAL GROWTH METHODS

In this section, the crystal growth methods used in the three projects will be introduced.

**2.1.1. Modified Bridgeman Method (MB),** This method is employed to grow the large size of  $\text{Nb}_x\text{Bi}_2\text{Se}_3$  and  $\text{Cr}_x\text{Sb}_2\text{Te}_3$  single crystals. In the original Horizontal Bridgeman method [25] [26], SnSe was heated into liquid solution and vapor and crystallized under a temperature gradient to room temperature. The temperature gradient in this reference is create by the distance between the solution to the heater. In other Bridgeman method, the temperature gradient can also be created by pulling the solution out of the furnace.

We modified this method using a high-vacuumed quartz ampoule and a suitable temperature profile to fit our targeted product. A reliable laboratory vacuum system was built to purge the quartz ampoule with high-purity argon and seal the stoichiometric compounds in the  $10^{-3}$  mm Hg vacuum. The quartz ampoule is then placed into a muffle furnace and heated above the melting point of the mixture and then slowly cool down. As the furnace is cooled, the temperature near the furnace door drops faster than the temperature at the center of the furnace. And crystallization occurs in the temperature gradient created between different locations of the furnace.

The resulting crystals are generally of good quality. However, the ease of result will strongly depend on the atomic forces, intermolecular forces, and intramolecular forces of the substances. Additionally, the quality of crystals can be interfered with by

varying factors such as temperature, cooling rate, and thermodynamic equilibrium of the liquid phase. The result of the Modified Bridgman method does not guarantee crystal formation, but it can ensure the ratio for atoms as initial input.

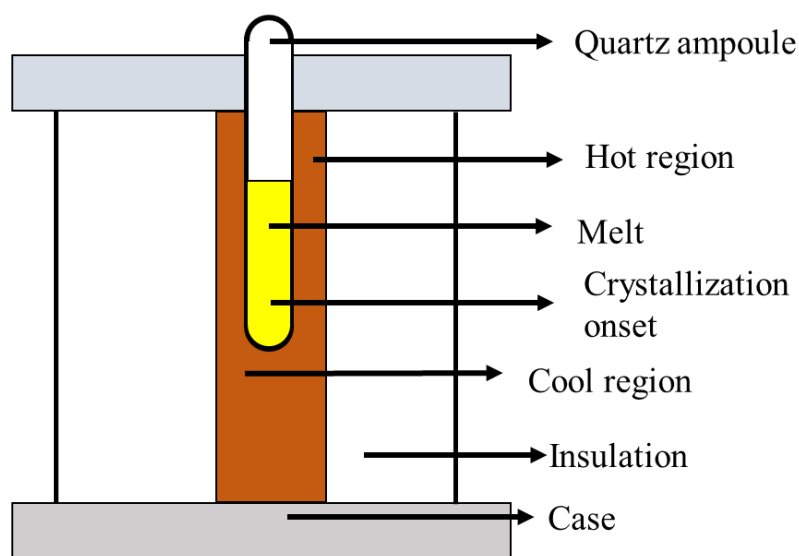


Figure 2-1 Schematic picture of the Bridgman method

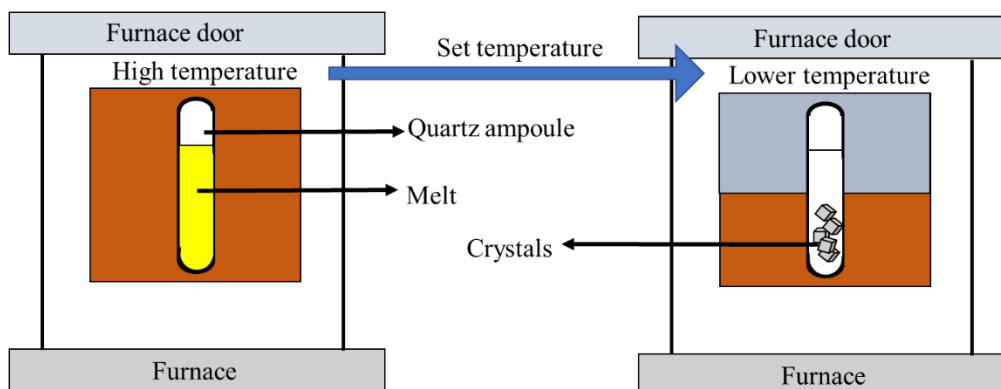


Figure 2-2 Schematic picture of the Modified Bridgman method

The schematic pictures of the original and modified Bridgman methods are shown in Figures 2-1 and Figure 2-2. In most cases, the original Bridgman methods apply the temperature gradient on the melted liquid by pulling the sample out of a Hot zone (furnace) or pushing it into a Cold zone. The change of sample positions causes the temperature gradient. In the modified Bridgman methods, the temperature gradients are caused by the furnace's natural cooling as the furnace temperature is changed, where it starts from the furnace door to the furnace heating center.

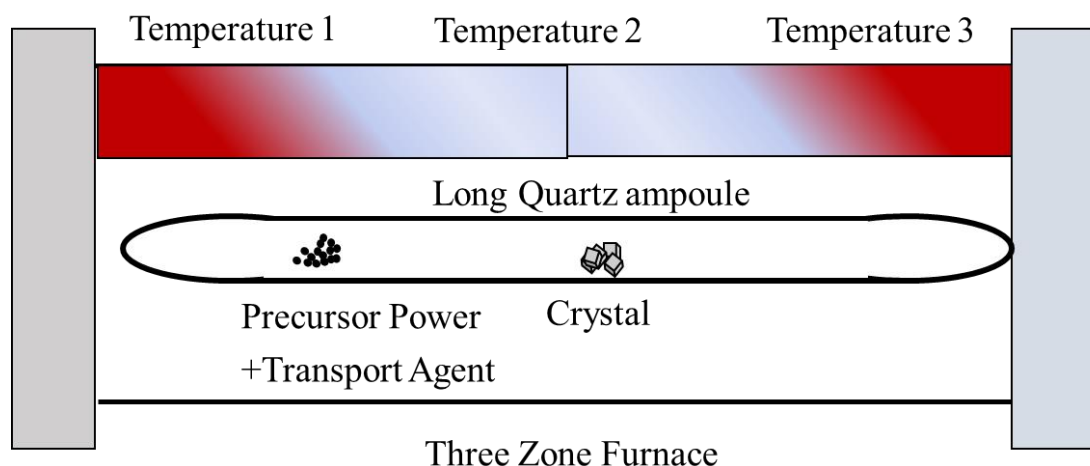


Figure 2-3 Schematic picture of the  $I_2$ -mediated Chemical Vapor Transport

**2.1.2.  $I_2$ -mediated Chemical Vapor Transport.** This is a vacuum deposition method used to produce high-quality solid materials. In a typical Chemical vapor transport (CVT), the substrate is exposed to one or more active precursors which react or decompose on the substrate surface. In the utilization of the CVT operating principle, polycrystal power precursors were placed in the heat zone and reacted with  $I_2$  to form aerosol with tiny crystals, and large-sized single crystals can be deposited on the

“substrate” (quartz ampoule wall) in the cold zone. A three-zone furnace is available to allow the transport agent to circulate within the seal ampoule as shown in Figure 2-3.

This method has been proven to synthesize highly crystalline, uniform, and layered single crystals but the ratio of atoms may be altered during transportation.

[27] Additionally, the process requires a fair amount of heating time due to the slower pace.

**2.1.3. Pressure Seal Swagelok.** This is a method invented by Dr. Hor when we attempted to grow the  $\text{CuAlO}_2$  polycrystalline. Due to the uncooperative escaping Cu atoms, we found a trace of Cu vapor when using a traditional solid-state reaction. Our attempts to apply pressures on the pellet in the heating process are using a customized Swagelok compression fitting with a high-strength steel rod. The procedure is as follows:

- A pellet is made from an 8mm compressing die after mixing the stoichiometric micro size power for 1 hour.
- The pellet is then wrapped in tantalum foil and then placed in the center of the Swagelok (10mm ID) tube.
- The Swagelok tube is placed in a hydraulic press with two high-strength stainless steel rods.
- A 2000-ton force is applied on both ends of the rod for 5 min and then released, repeated 5 times.
- The Swagelok compression fitting nuts are then tightened while the force remains on both ends of the seal.
- The pressure seal is then placed in a quartz ampoule and sealed in high vacuum ( $10^{-3}$  mm Hg).

Figure 2-4 shows the schematic plan view and the modified Swagelok for the pressure-seal Swagelok setup. The Swagelok is modified to increase its inside diameter to fit the sample pellet and the dowel pin. The compressed pellet is wrapped with Tantalum Foil and then placed inside the Swagelok and compressed by two dowel pins under a hydraulic press. While the applied pressure from the hydraulic press reaches 20Tons. The Swagelok Nut and Ferrule are tightened with a wrench. The pellet inside the Swagelok is restricted to 70% of its original volume. Partial pressure is applied to the sample pellet in this method.

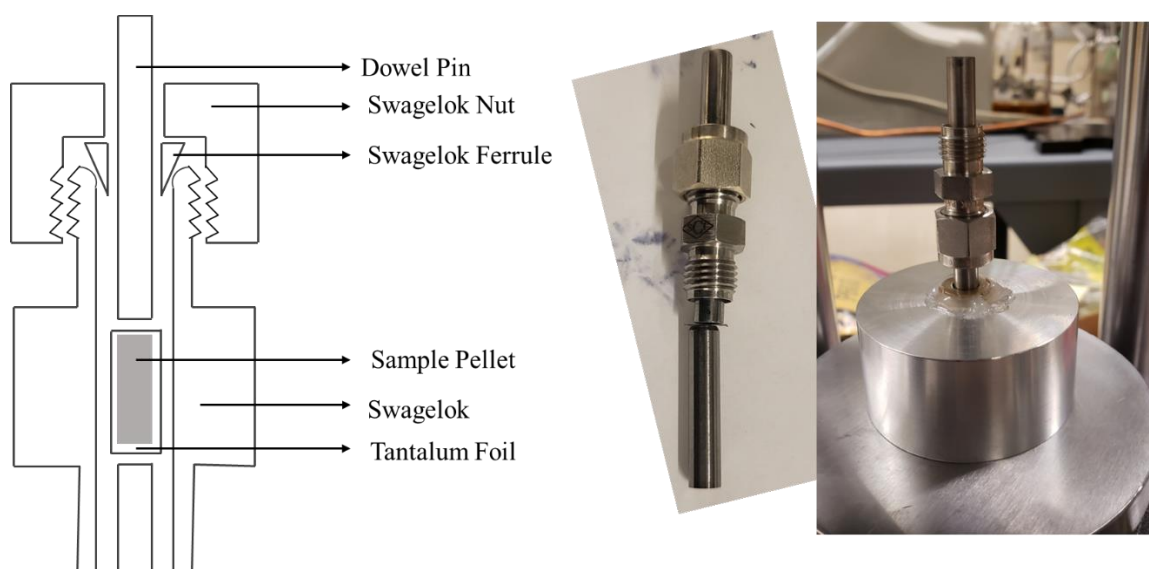


Figure 2-4 Picture of Swagelok method

**2.1.4. Double-Seal Ampoule.** This method is invented by Dr.Hor on the purpose to apply pressure on the compressed pellet during the heat treatment in solid-state reaction.

As shown in Figure 2-5, the compressed pellet is first sealed in a vacuum Pyrex glass ampoule and then seal with sulfur powder in another vacuum quartz ampoule. And the calculated amount of sulfur powder from the ideal gas law:  $PV = nRT$  is added to the large quartz ampoule. The pressure used is obtained from Barlow's Formula and the maximum is about 5 atm. The temperature for calculation is based on the temperature for the heat treatment. To protect the melted Pyrex glass, a circle of quartz wool is used to wrap the Pyrex glass ampoule to prevent its thermal extrusion with the quartz wall. Afterward, a second quartz ampoule is sealed in a high vacuum.

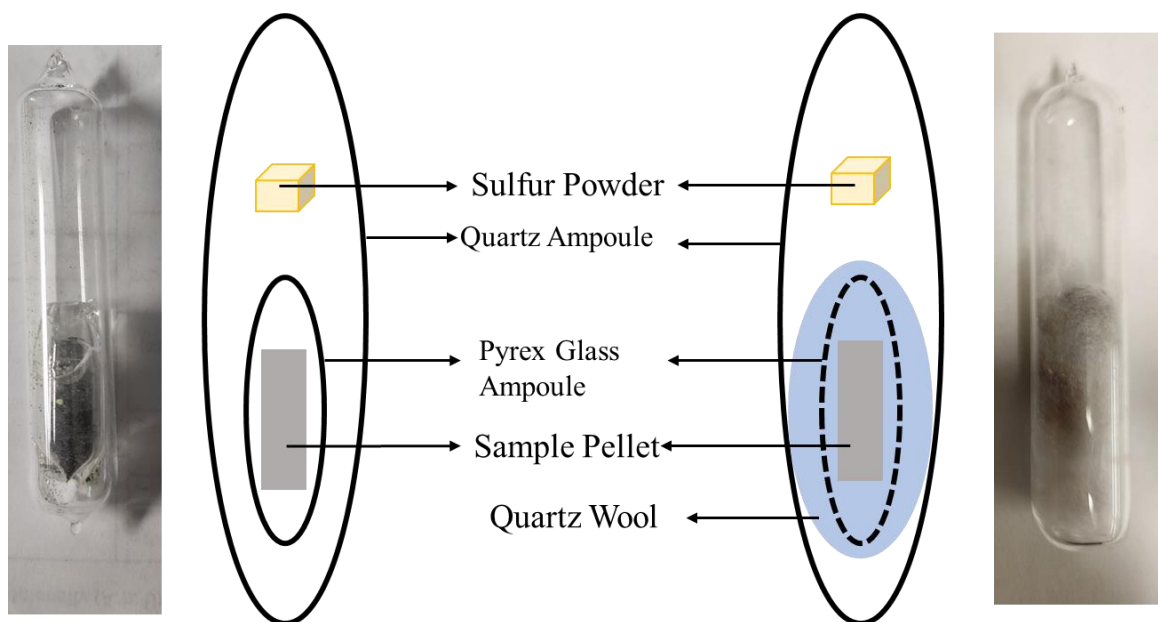


Figure 2-5 Sketch and picture of the Double-Seal ampoule

With this double-seal ampoule method, during the heating process, the Pyrex glass tube would soften and wrap the pellet, while the sulfur turns into a gas and applies

pressure to the first ampoule. The pellet is compressed in the heat treatment and the pressure can be modified by the amount of sulfur introduced or the temperature.

## 2.2. MEASUREMENT METHODS

In this section, physical properties measurements methods will be introduced with their basic mechanism.

**2.2.1. Scanning Tunneling Microscope (STM).** STM was developed in the 1980s. As shown in Figure 2-6, this instrument consists of a sharp conducting wire tip over a very closed surface. By applying an electrical voltage to the tip or the sample, the surface electronics information can be imaged at the atomic scale.

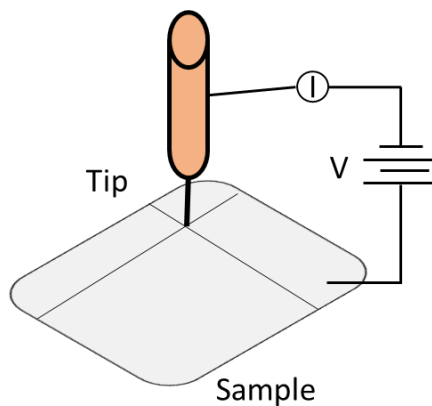


Figure 2-6 Schematic of Scanning tunneling microscopy

STM uses the quantum mechanical effect of tunneling, in which a tunneling current occurs when an electron wave moves through a potential barrier (space between tip and sample). The probability of electron tunneling depends on the thickness of the barrier and drops off exponentially with the barrier thickness. Hence the wire tip is

brought close to the surface. The tunneling current across the tip and sample was monitored as the wire tip is scanned with angstrom-level control.

The tunneling current [28] to a reasonable approximation is below:  $I \approx$

$$\frac{4\pi e}{h} e^{-2\sqrt{\frac{4m_e\phi}{h^2}}} \rho_t(0) \int_{-eV}^0 \rho_s(\varepsilon) d\varepsilon,$$

where  $\phi$  is the height of the tunneling wavefunction,

which is some mixture of the work functions of the tip and sample. As shown in Figure 2-7, the tunneling current is proportional to the density of the state and reveals electronic information over the whole surface. By adjusting the biased voltage, the effective fermi level of the sample electron for the tip electrons can be altered and reveal electronic information near the surface.

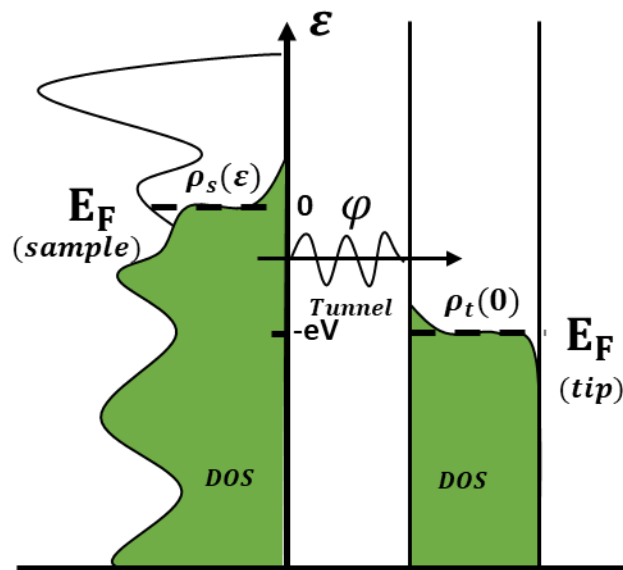


Figure 2-7 Tunneling current approximation

The STM operates in two distinct [29] modes: constant height mode and constant current mode. Constant height mode is generally used when the sample surface is very

smooth. The probe tip stays at a fixed height in this mode while quickly rastering across the sample. By measuring changes in the intensity of the tunneling current as a function of (x,y) position and bias voltage, researchers can construct an image of the electronic density of states of the sample surface, defects, frontier molecular orbitals, and more.

The constant current mode. In this mode, the tunneling current is held constant using a feedback loop system that adjusts the distance between the tip and the surface. If the tunneling current exceeds the target value, the feedback control system will increase the distance between the tip and the sample; if the tunneling current is less than the current target value, the feedback control system will bring the tip closer to the surface of the sample. The resulting three-dimensional distance profile is a function of the (x,y) position and can reveal the conformation of molecules on the surface.

We used the constant current mode to determine whether the Nb atoms are intercalated between the quintuple layers of Bi<sub>2</sub>Se<sub>3</sub>. The measurement is performed on the newly cleaved surface under vacuum. Figure 2-8 shows the STM images taken on the cleaved Se surface of a Nb<sub>0.25</sub>Bi<sub>2</sub>Se<sub>3</sub> single crystal. The clean surface was obtained by in-situ cleaving under UHV conditions ( $\sim 10^{-11}$  torr) at room temperature. And the topographic images are taken at the cleaved surface at a bias voltage of -0.4V and +0.5V with constant current of 10 pA. This STM measurement is done at Rutgers University by J,Dai. By changing the bias voltage, to maintain the current, images are taken at different height with respect to the sample surface.

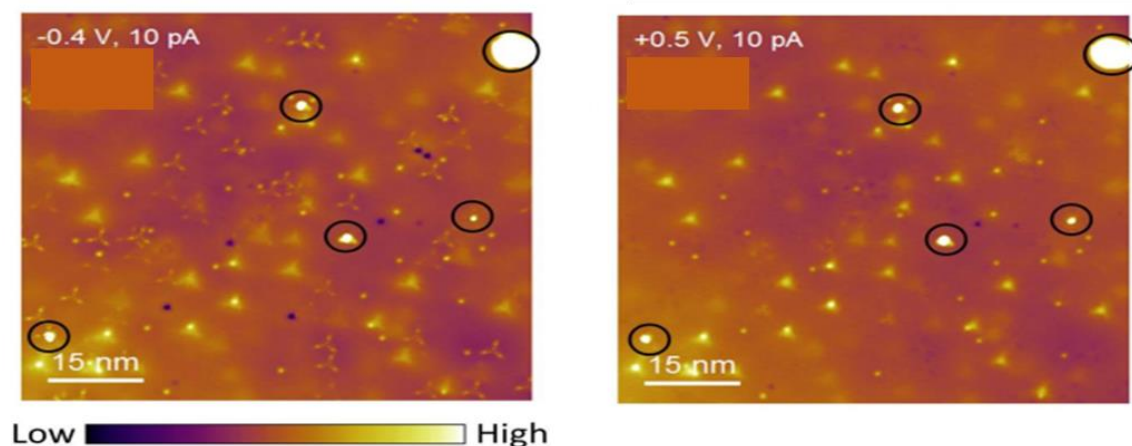


Figure 2-8 STM image for  $\text{Nb}_{0.25}\text{Bi}_2\text{Se}_3$

The cloverleaf-shaped three-fold symmetric defects have been identified as BiSe antisites. [30] [31] The dark three-fold symmetric features can be attributed to the substitution of Bi with Nb or the Se vacancy. The various-sized protrusions indicate clusters of Nb atoms; and their heights are bias-independent, suggesting the Nb atoms are formed above the cleaved surface.

It is noted that the substitutional Nb samples do not show superconductivity at temperatures down to 2K. This confirms that the intercalating Nb atoms are responsible for the superconductivity.

**2.2.2. X-Ray Powder Diffraction (XRD).** XRD is an analytical technique used for phase identification of a crystalline material and can provide information on unit cell dimensions. The analyzed materials are finely ground into homogenized powder. The crystal structure information is collected and stored in the database for reference.

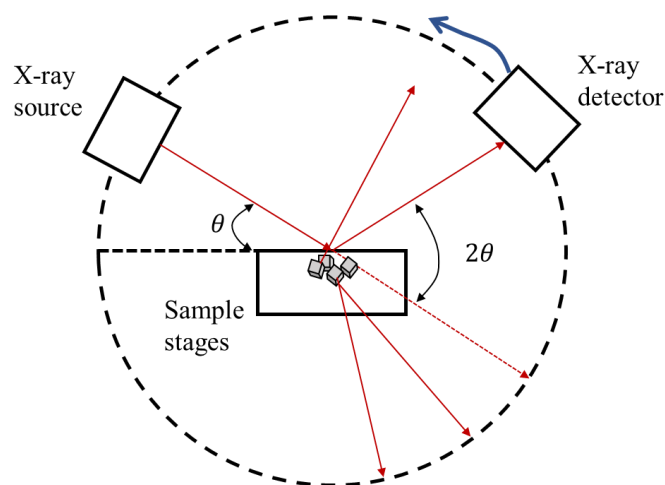


Figure 2-9 Sketch of the X-ray diffractometer

As shown in Figure 2-9, an X-ray diffractometer consists of three basic components: An X-ray source, a sample holder, and an X-ray detector. The X-ray source generates a known wavelength electron beam. When these waves reach the sample, are neither reflected off the surface nor enter the lattice and are diffracted by the atoms. According to Bragg's law, the reciprocal lattice vector  $G$  scaled with the equation:  $G = \frac{4\pi}{\lambda} \sin\theta$ . By scanning the rotating powered samples through a range of  $2\theta$  angles, all possible diffraction directions of the lattice should be recorded by the detector and converts to a count rate.

For  $\text{Nb}_x\text{Bi}_2\text{Se}_3$ ,  $\text{Cr}_x\text{Sb}_2\text{Te}_3$  and  $\text{CuAlO}_2$  projects, X-Ray powder diffraction is used to identify the crystal structure and impurity phases. A Multi-purpose Diffractometer with a copper source of  $\lambda = 0.15418$  nm with a minimum step size of  $2\theta = 0.06$  is used. The pattern is taken at 25 degrees Celsius, and the compared standard X-ray pattern peak is obtained from the JCPDS database.

Figure 2-10 shows that  $\text{Nb}_{0.25}\text{Bi}_2\text{Se}_3$  corresponds to the standard  $\text{Bi}_2\text{Se}_3$  XRD patterns. The film peaks of (0 0 n) with  $n=3, 6, 9$ , and so forth., are indicated on the plots. The matched peaks show that the crystal is in the space group R3m. The lattice parameters are obtained from the Xper software and  $a(\text{\AA})=4.1396$ ,  $b(\text{\AA})=4.1396$ ,  $c(\text{\AA})=28.6360$ . The c parameter is slightly increased by doping compared to the un-doped  $\text{Bi}_2\text{Se}_3$  ( $c(\text{\AA})=28.53288$ ).

The red triangle below the figure shows the additional peak compared to the un-doped  $\text{Bi}_2\text{Se}_3$ , and they are identified as the Nb-Se and Nb-Bi bonding. Possible byproducts within the sample are  $\text{NbSe}_2$  and  $\text{NbBiSe}_3$ . The  $\text{NbSe}_2$  has been reported with a critical temperature of 6.8K. [32], and  $\text{NbBiSe}_3$  has a critical temperature of 2.3K. [33] As the single crystal quality improves, these possible byproducts in the superconductivity measurements can be avoided. Some undesired signals may appear in the AC magnetization measurement when examining the Meissner effect due to the limit of the Modified Bridgman method. Those samples are discarded and considered invalid measurements.

Figure 2-11 shows the XRD results for the Magnetic Topological Insulator projects.  $\text{Cr}_{0.2}\text{Sb}_2\text{Te}_{2.9}/\text{Cr}_{0.2}\text{Sb}_2\text{Te}_3$  corresponds to the standard  $\text{Sb}_2\text{Te}_3$  XRD patterns. The c-axis lattice parameter of undoped  $\text{Sb}_2\text{Te}_3$  was reduced from 30.458 Å to 30.419 Å for  $\text{Cr}_{0.2}\text{Sb}_2\text{Te}_{2.9}$  and 30.402 Å for  $\text{Cr}_{0.2}\text{Sb}_2\text{Te}_3$ . The lattice parameters for these structures are not much different from that of the undoped  $\text{Sb}_2\text{Te}_3$  lattice.

Figure 2-12 shows the XRD results for  $\text{CuAlO}_2$  prepared by the solid-state reaction method with the different sintering temperatures. Multi-crystals samples were grounded for measurements. The peaks of 900C and 1200C follow the standard  $\text{CuAlO}_2$

XRD pattern, but the 1500C samples show a significant deformation in the pattern. This is expected because, during the heat treatment, visible copper is deposited into the aluminum crucible from the compressed pellet. This phenomenon is also mentioned in reports for thin film growth, and the extra peak is assigned to the CuO XRD pattern. [35] The mostly likely cause is the  $\text{CuAlO}_2$  decomposes into  $\text{CuAl}_2\text{O}_4$  and  $\text{CuO}$ . [36]

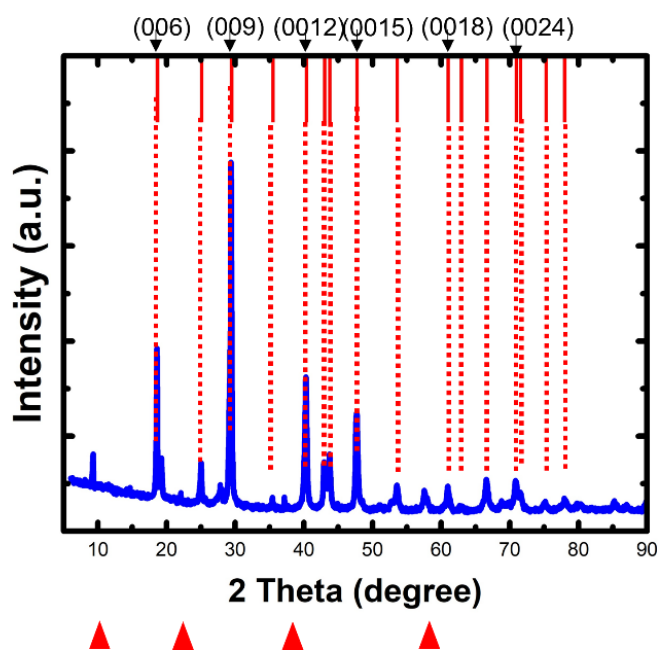


Figure 2-10 XRD results for  $\text{Nb}_{0.25}\text{Bi}_2\text{Se}_3$

Bulk samples of  $\text{Bi}_2\text{Se}_3$  and  $\text{Sb}_2\text{Te}_3$  have a rhombohedral crystal structure in the space group  $D3d5 R3m$ , which consists of 5 quintuple layers (QLs) [34]. The interlayer bonding within the QLs is stronger than the bonding between QLs, and it is natural to expect the doping atoms (Nb/Cr) are located at the cleavage plane between two QLs. This fact has been well confirmed by recent experiments on doped topological insulators thin films.

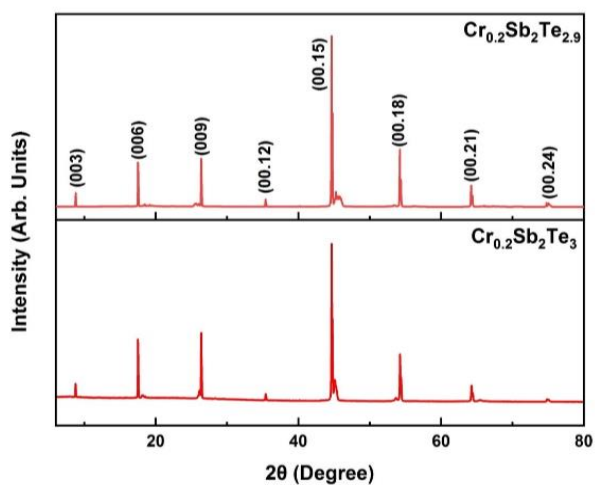


Figure 2-11 XRD results for Cr-doped  $\text{Sb}_2\text{Te}_3$

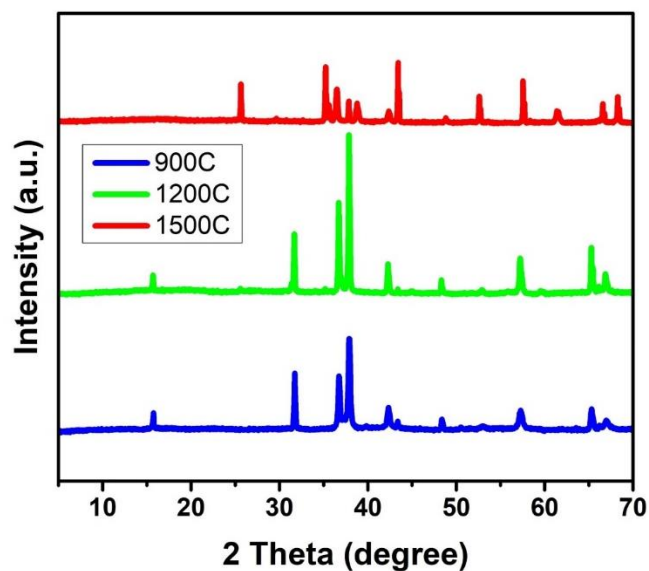


Figure 2-12 XRD results for  $\text{CuAlO}_2$

**2.2.3. Angle-Resolved Photoemission Spectroscopy (ARPES).** ARPES [37] is an experimental technique based on the photoelectric effect and a powerful method for measuring the electronic structure of solids. With rapid development, soft-X-ray ARPES,

time-resolved ARPES, spin-resolved ARPES, and spatially resolved ARPES emerge as indispensable experimental probes in the study of topological materials. Over the past few years, ARPES has had a crucial role in the discovery and identification of topological materials.

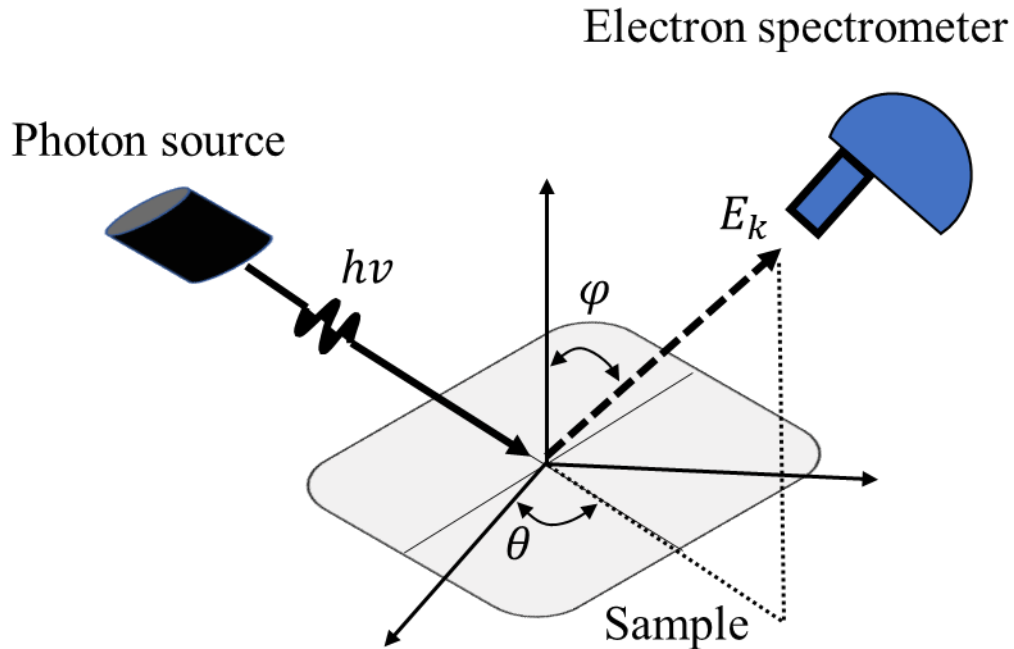


Figure 2-13 Sketch of ARPES

A typical ARPES consists of a light source, sample holder, and electron spectrometer and performs in an ultra-high vacuum, as shown in Figure 2-13. The light source delivers, usually polarized, focused, and high-intensity beam of photons to the sample. The electrons on the sample will absorb sufficient energy and ejects with kinetic energy  $E_k = h\nu - E_B$  and the electrons' momentum  $P$  is given by the equation,  $|P| = \sqrt{2m_e E_k}$ . The sample holder facilitates the cleavage to expose clean surfaces and precise positioning (rotate for the sample). The electron spectrometer, using the sample surface as

a reference frame, provide the emission angle  $\theta$  and  $\varphi$ .  $k_{\parallel} = \frac{1}{\hbar}P_{\parallel} =$

$$\frac{1}{\hbar}\sqrt{2m_e E_k}(\sin\theta\cos\varphi\hat{k}_x + \sin\theta\sin\varphi\hat{k}_y), k_{\perp} = \frac{1}{\hbar}\sqrt{2m_e(E_k\cos^2\theta + V_0)},$$

$V_0$  is a constant called the inner potential and can be determined from photon-energy-dependent measurement by fitting the experimental periodicity along the  $k_{\perp}$  direction. [38]

In this dissertation, ARPES measurement were performed at the Planar Grating Monochromator (PGM) beamline of the Synchrotron Radiation Center (SRC). SRC uses a Scienta R4000 analyzer with an energy resolution of <5 meV and angular resolution of <0.2°. The single crystal sample is transferred and cleaved under ultra-high vacuum conditions by the techniques available at the beam line.

#### **2.2.4. Physical Properties Measurements Systems (PPMS). Quantum**

Designed PPMS provides a flexible programmable workstation to perform a variety of experiments that require precise thermal or magnetic control. The PPMS can execute AC/DC magnetization, Resistivity, electro-transport, or thermos-electric measurements based on the connected module and measurement options. With the integrated Model 6000, the PPMS software MultiVu software incorporates the hardware and module to execute measurement sequences on demand. Figure 2-14 and Figure 2-15 show the sketch setup for the PPMS. PPMS uses the Liquid Helium as a cooling source. A high-capacity nitrogen-jacketed Dewar is equipped to provide the liquid-helium bath for the PPMS probe. The operating efficiency of liquid helium relies on a layer of liquid nitrogen sandwiched between the superinsulation and the liquid helium. The PPMS probe functions as a superconducting magnet, helium level meter and basic temperature-controlled hardware and a sample chamber.

PPMS sample environment includes a magnetic field up to  $\pm 9$  T and a 1.8 - 400K temperature range. The magnet is powered and controlled by Model6700 Magnet Controller. Temperature is reported in the attached manual with an accuracy of  $\pm 0.5\%$  and can be varied with full weep and slew rates from 0.01K/min up to 12K/min. Temperature stability is  $<0.2\%$  for temperature  $<10$ K and  $<0.02\%$  for temperature  $>10$ K. The magnetic field resolution is 0.03mT. Both temperatures and magnetic fields have three standard approaching mode: linear, oscillating and No overshoot.

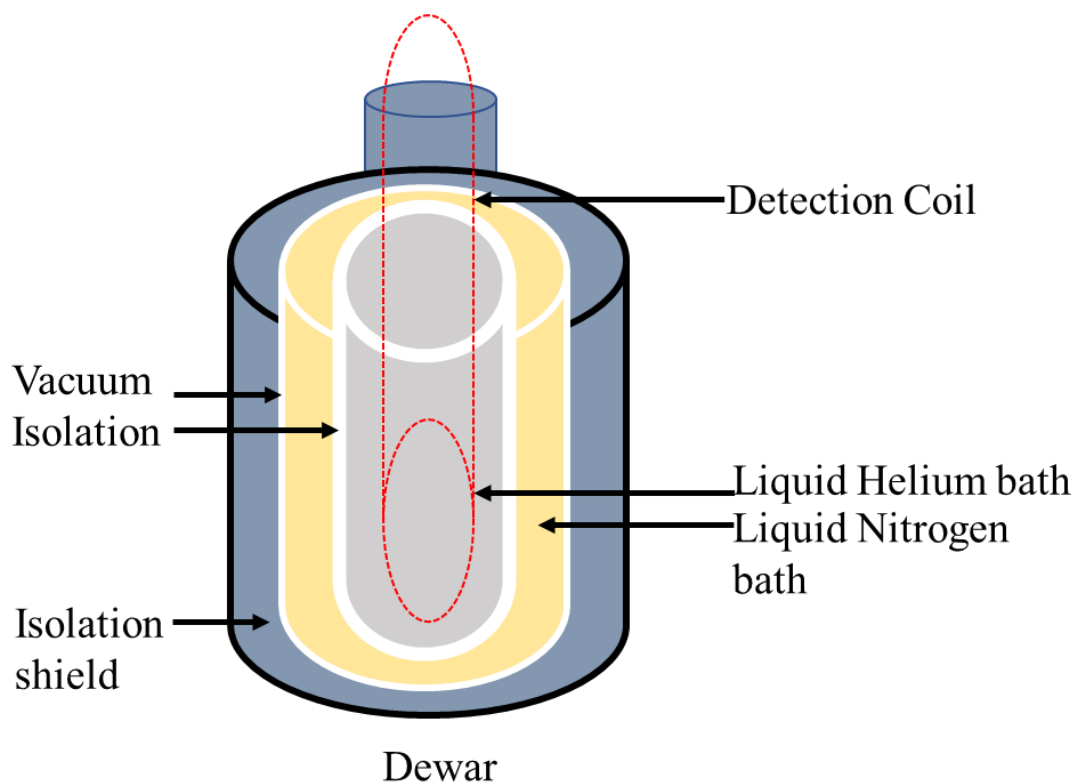


Figure 2-14 Sketch of the PPME cooling Dewar

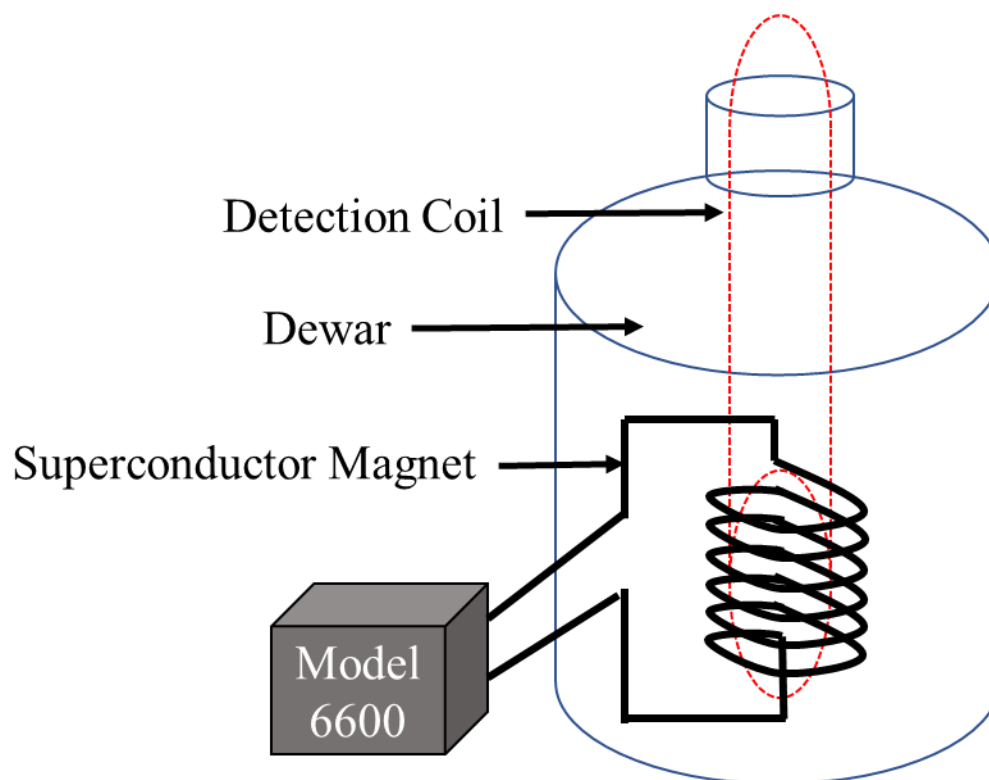


Figure 2-15 Sketch of PPMS

**2.2.4.1. AC/DC magnetization.** In PPMS, the ACMS module is used for magnetization measurement, and it contains AC/DC modes. An ACMS drive coil is inserted to the host PPMS platform. The drive coil provides an alternating excitation field and a detection coil set. The detection coil responds to the combined sample moment and excitation field, where its measuring region has a high field homogeneity with the PPMS superconducting magnets.

The detection coils are arranged in a first-order gradiometer configuration to help isolate the sample's signal from the alternating excitation field and other background sources. This configuration utilized two sets of counterwound copper coils connected in

series and separated by several centimeters. They will receive the same excitation signal and a net field remains.

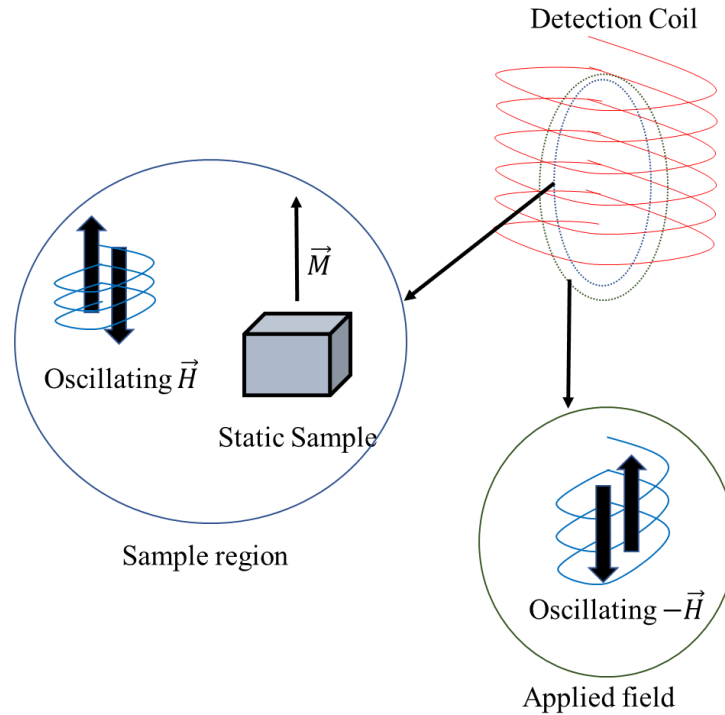


Figure 2-16 Schematic AC mode

During DC mode, a constant field is applied to the measurement region, and the sample is moved quickly through both sets of coils, inducing a signal according to Faraday's law, as shown in Figure 2-17.

As shown in Figure 2-16, during AC mode while the coil generates an alternating field, the sample is positioned in the center of each detection coil. Another compensation coil is situated outside the AC drive coil. The drive coil and the compensation coil are connected in series, so they maintain the same excitation signal. A net field remains within the measurement region, but outside the measurement region, the magnetic field remains net zero, so the detection coils only measure the moment from the sample.

The detection coil also contains a low-inductance calibration coil, a calibration will be made before the sample is inserted to increase the accuracy of the amplitude of the phase.

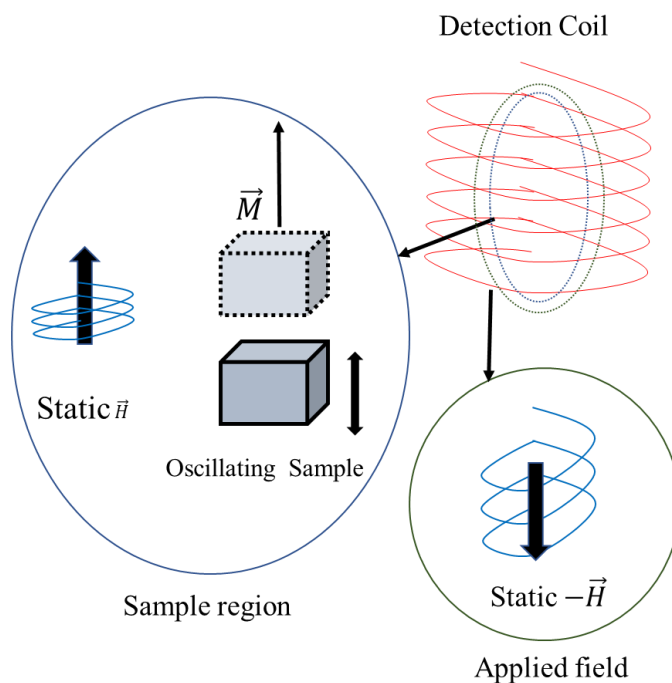


Figure 2-17 Schematic DC mode

As the magnetic field is applied on the sample, the sample generated its responding magnetic moment. With a motor attached to the sample rod, oscillation with fix rate is applied to the sample, and the responding magnetic moment with generate an induction current in the detection coil. The induction current can be used for calculating the responding magnetic moment in the sample with PPMS's build-in algorithm.

**2.2.4.2. Resistivity measurement.** In PPMS, the resistivity module uses the 4-probe sample pucks for resistivity measurements, as shown in Figure 2-18. Using four platinum wires to attach a sample to the sample puck greatly reduced the contribution of joints to the resistance measurement. Current is passing through the sample via two current joints and two separate voltage joints measure the potential difference across the sample. The voltmeter has an extremely high impedance, so the voltage joints draw very little current, and it has a high resolution of up to  $10^{-8}$  V. Thus, the PPMS can calculate the resistance with Ohm's law to a high degree of certainty. Ideally, the sample will be cut into a perfect rectangle shape with precise dimension parameters and resistivity can be converted.

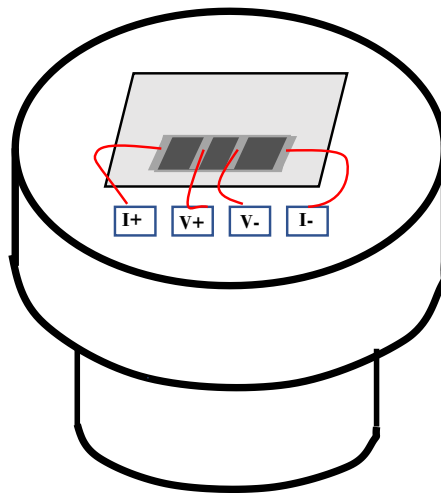


Figure 2-18 Sketch of a 4-probe sample puck

**2.2.4.3. Hall measurement.** PPMS uses the 5-probe setup in the AC Transport module as shown in Figure 2-19. The physical connection technique between the sample and sample puck is the same as the 4-probe measurement. The ACT module introduces a second negative voltage joint to help reject external fluxes. While the magnetic field is turned off, a potentiometer between the two voltage joints is used to null the offset from sample resistance. Then once a field is applied, the measured potential drop gives only the Hall potential, plus the components due to instrumental limitation. Such a component mentioned in the operation manual is claimed to be removed with the company's AC filtering techniques from the Model 7100 AC Transport Controller.

Noted that the sample's resistance may still contribute to the measured hall voltage even after balancing, the Hall measurement should be measured at both positive and negative fields so that the Hall resistivity at zero magnetic fields can be subtracted from the measured resistivity.

The hall resistance is calculated by  $R_{xy} = \frac{V_y}{I_x}$ , where  $V_y$  is the transverse hall voltage and  $I_x$  is the applied longitudinal current. The thickness  $t$  and voltage lead separation (width)  $w$  of the sample are recorded, and the cross-section area  $A = w * t$  is calculated from them. In situ Hall resistivity is confirmed by our test sample as  $\rho_{xy} = R_{xy} \frac{w}{A}$ . Notable this is different from the 2D electron gas Hall resistivity, hence, the quantitative result may require re-calculation from the raw data file. Noted the Hall measurement in PPMS provides both AC and DC current mode, and the current mode shows no impact on the data we collected.

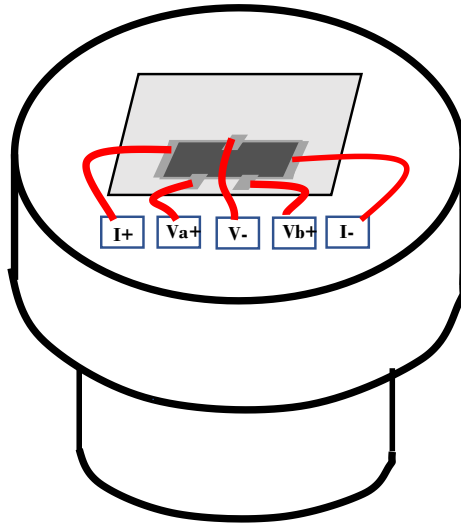


Figure 2-19 Sketch of 5-probe sample puck

### 3. MAGNETIC TOPOLOGICAL INSULATORS

With intentional doping of magnetic elements, such as Fe, Cr, V, and Mn, ferromagnetism can be introduced into the topological insulators while the surface state remains robust to the magnetic dopants. Such Topological insulators are classified as Magnetic Topological Insulators. Doping with 3d transition metal elements has been proved to be a practical [39] approach to introducing ferromagnetism into a material.

Two mechanisms have been considered as possible origins for ferromagnetism in magnetic Topological Insulators; the carriers-mediated Ruderman-Kittel-Kasuya-Yosida (RKKY) mechanism [40] [41] and the local valence-electron-mediated Bloembergen-Rowland, or Van Vleck mechanism [42].

Ruderman-Kittel-Kasuya-Yosida's (RKKY) mechanism is experimentally verified in the Mn-doped  $\text{Bi}_2\text{Te}_3$  systems [43]. With magnetic impurities introduced to break TR symmetry and suppresses the low energy local density of states, the Fermi level lies close to the Dirac point. It gives rise to a more vital ferromagnetic ground state on the surface, where a net spin is perpendicular to the surface. Another direct physical property predicted for such an RKKY mechanism is that the ferromagnetic moment increases dramatically as the concentration of magnetic impurity starts to be introduced [44] and remains unchanged for large enough dopant concentrations, as Figure 3-1(a) shows.

The Bloembergen-Rowland (BR) or Van Vleck mechanism is mainly explained for doping 3d transition metals. Thin films of Cr doped  $(\text{Bi}_x\text{Sb}_{1-x})_2\text{Te}_3$  supports the idea through the BR mechanism. The conduction and valence band are mixed and give rise to a considerable spin susceptibility by narrowing the exchange gap. In particular, the

ferromagnetic interaction mediated by valence electrons in a narrow-gap semiconductor has been proposed to host the quantum anomalous hall effect without invoking a large concentration of conduction carriers.

A simple comparison of these two mechanisms is shown in Figure 3-1. In the RKKY mechanism, the dopant raises the Fermi level, brings extra spin in the topological insulator, and generates ferromagnetism. While in the BR mechanism, the dopant will lower the bulk conduction band and allow more free spins with the same Fermi level. The main difference between these two similar effects is that the gap between the conduction and valence bands changes with dopants.

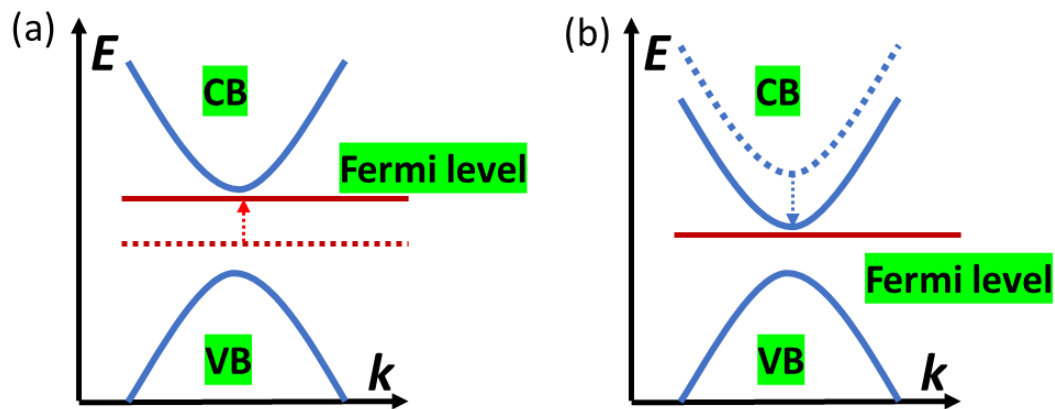


Figure 3-1 Comparison of RKKY and BR mechanisms: (a) RKKY (b) BR

### 3.1. BREAKING TIME-REVERSAL SYMMETRY

The gapless metallic surface state in 3D topological insulators is protected by time-reversal symmetry (TRS). By applying an out-of-plane magnetic field, introducing ferromagnetic order with perpendicular magnetization, or bring the sample in proximity to a magnetic insulator, the TRS could be broken.

The surface state of a 3D Topological insulators is described by the Hamiltonian [45] $H = v_F(-k_y\sigma_x + k_x\sigma_y) = R \cdot \sigma$ , with  $R = (-k_y\sigma_x + k_x\sigma_y)$ , where  $v_F$  is the Fermi velocity,  $\sigma_x, \sigma_y$  are Pauli matrices.

With broken TRS, Hamiltonian gain an exchange interaction term and can be described by the following:  $H = R \cdot \sigma + m\sigma_z$ , the term  $m\sigma_z \equiv -Jn_s\bar{S}_z\sigma_z$ , where  $J$  is the exchange coupling between the  $z$  component of the spin of the Dirac electrons and the localized spin  $S$  and  $n_s$  is the areal density of localized spins, which have average  $z$  component  $\bar{S}_z$ , and  $\sigma_z$  are Pauli matrices. [46]

Figure 3-2 shows the schematics of the surface state of a 3D Topological insulator for the time-reversal symmetry and broken time-reversal symmetry by effective magnetic interaction. This exchange interaction causes an opening gap in the Dirac surface state, which causes the Dirac fermions in the surface state to become massive. [47]

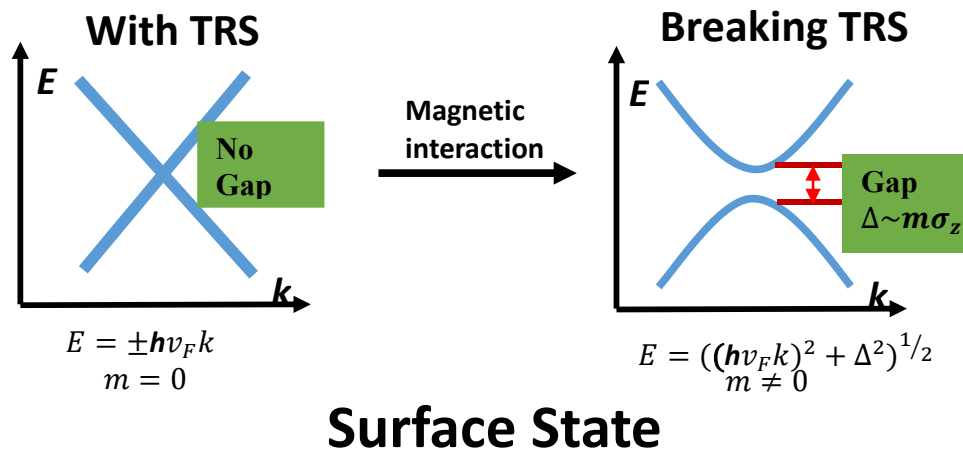


Figure 3-2 Massive Dirac Fermions by Magnetic Interaction

### 3.2. ANOMALOUS HALL EFFECT

The Anomalous Hall effect (AHE) occurs in ferromagnetic materials and has a productive history in the research of electricity and magnetism. Very early on, the experimental investigator learned the empirical relation of the Hall resistivity  $\rho_{xy} = R_o H_z + R_s M_z$ , where the hall resistivity  $\rho_{xy}$  in ferromagnet initially increases steeply in a weak magnetic field  $H_z$ , but saturates at a significant value that is nearly  $H_z$ -independent [48]. The saturates hall resistivity is intuitively proportional to the magnetization of the crystal  $M_z$ , and responds to the anisotropy with the crystal. In this empirical relation,  $R_o H_z$  stands for the original Hall effect contribution and  $R_s M_z$  stands for the contribution from spontaneous magnetization.

An all-encompassing framework for AHE has been laid out by Naoto Nagaosa [48] on both theoretical and experimental fronts. In his summary of the theoretical development of the mechanism that gives rise to AHE, they are the intrinsic deflection effect, side jump effect, and skew scattering effect. It is often the case that all three mechanisms appear simultaneously in AHE, and the Hall resistivity in AHE can be expressed as:  $\rho_{xy} = \rho_{xy}^{int} + \rho_{xy}^{Skew} + \rho_{xy}^{side}$ . Illustrations of these three mechanisms are shown in Figure 3-3.

In 1954, Karplus and Luttinger (KL) proposed a theory [49] for the Hall effect in a ferromagnet referred to as the intrinsic contribution to AHE. In this calculation, KL found that when an external magnetic field is applied, due to the spin-orbit interaction, a current perpendicular to the magnetic field and the mean direction of spins will have a group velocity. Furthermore, this velocity is proportional to the ratio of magnetization to

saturation magnetization. Additionally, the Hall constant in this theory heavily depends on the temperature, and proportional to the square of the resistivity ( $\rho_{xy}^{int} \propto \rho_{xx}^2$ ).

The skew scattering effect is discovered in the investigation on Ni alloys [50] [51] where the Hall resistivity shows a linear contribution from resistivity ( $\rho_{xy}^{skew} \propto \rho_{xx}$ ). In Smit's theory, the perturbation potential is asymmetric and chiral upon the introduction of transition metal atoms. When this mechanism dominates, the current due to spin-orbit interaction in KL theory will have the opposite sign and be proportional to the transport lifetime. However, such a case will require a perfect crystal with even distribution of impurities.

A side jump mechanism was proposed when an electron undergoes the scattering of impurity and phonon [52]. In quantum mechanics, a free electron can be viewed as a plane wave, which could be scattered by the potential created by the impurities in the AHE materials. The wave vector for the free electron will suffer a displacement transverse to itself, and the magnitude of the displacement turns out to be a constant. Moreover, the probability of the side jump cannot be determined in the traditional Boltzmann transport theory.

These three semi-classical effects have been integrated by Kondo [53], and the interaction between conductivity and magnetic impurities has been demonstrated through the Kondo formula for Hall conductivity:  $\sigma_{xy} = \frac{e^2}{h} \frac{1}{4\pi} \int dk_x \int dk_y \hat{\mathbf{d}} \cdot \left( \frac{\partial \hat{\mathbf{d}}}{\partial k_x} \times \frac{\partial \hat{\mathbf{d}}}{\partial k_y} \right)$ . With a given perturbation contribution from the magnetic impurities, the theoretical limit of Hall conductivity can be computed in accordance.

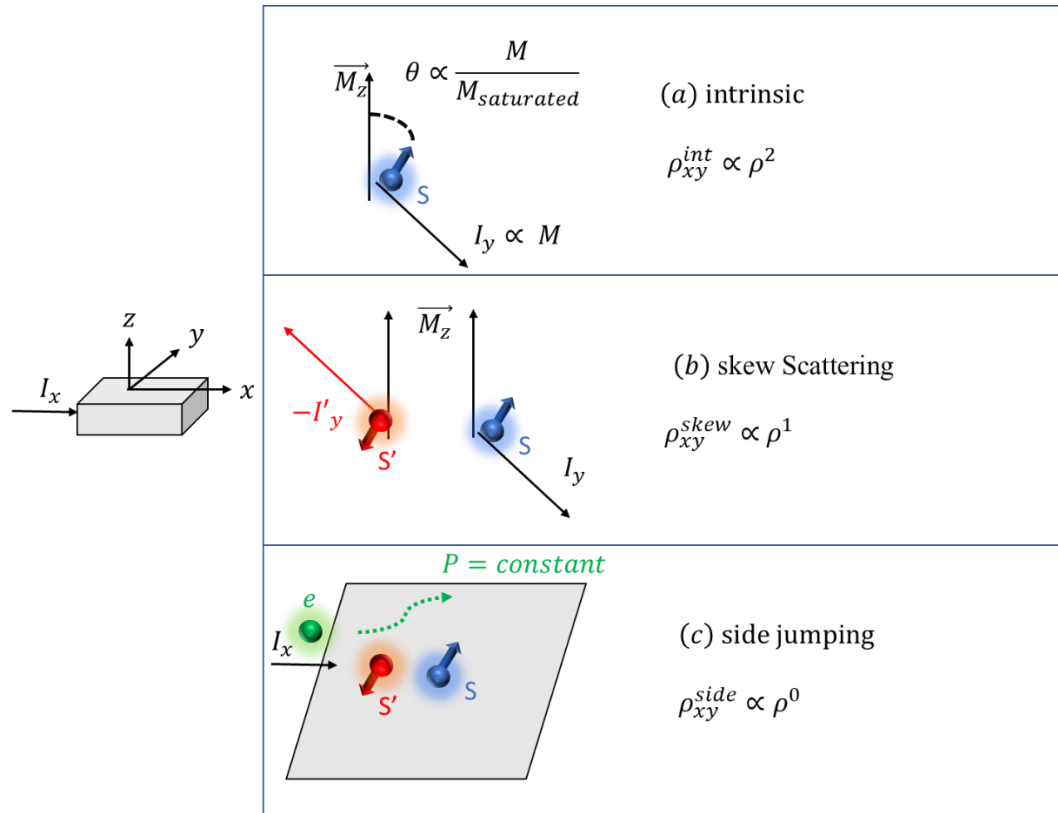


Figure 3-3 Intrinsic deflection effect, side jump effect, and skew scattering effect

### 3.3. QUANTUM ANOMALOUS HALL EFFECT (QAHE)

Modern interest in the Anomalous Hall effect is rekindled when it appears in topological insulators . [54]With the co-existence of ferromagnetic order and strong spin-orbit coupling in a Magnetic Topological Insulator, the Quantum Anomalous Hall effect (QAHE) is proposed, whose Hall conductivity can be quantized  $\sigma_{xy}^{QAHE} = (n + 1) \frac{e^2}{h}$ .

[55] [42] [56]

**3.3.1. The Quantum Hall Effect (QHE).** QHE was discovered in 1980 on silicon field effect transistors [57] by Klaus von Klitzing, for which he received a Nobel prize in 1985. The experiment was performed in shallow temperatures (millikelvins) and a strong magnetic field (several teslas). With fine-tuning of gate voltage, the hall resistance shows

a plateau ( $R_{xy} = \frac{V_{Hall}}{I_{channel}} = \frac{h}{e^2\nu}$ ), where the longitudinal resistance disappears ( $R_{xx} = 0$ ).

The divisor  $\nu$  can take on either integer or fraction as the QHE can. In the classical understanding,  $\nu$  is equal to the filling number of Landau levels. At low temperatures, all filled states below a specific Fermi energy, and as the magnetic field increase, the spacing of Landau levels increases proportionately, so fewer of these levels are filled [58], and the filling number  $\nu$  is constant.

This admittedly oversimplified explanation of the Quantum Hall effect only lasts for a while before TKNN invariant [59] is identified, also known as the first Chern number (topological invariant). With the adaption of the Berry phase [60] and Berry curvature in momentum-space coordinates, the integral of Bloch wavefunction over the first Brillouin zone is calculated. It is proved that the result (TKNN invariant) is identical to the constant in the Quantum Hall effect from the Kondo formula.

**3.3.2. Quantum Spin Hall Effect (QSH).** The QSH does not necessarily require an external magnetic field to achieve a quantized Hall resistance. In 1988, F.D.M. Haldane [61] proposed the famous Haldane model to realize the Quantum Hall effect using the spin-orbit coupling [20]. In Haldane's Hamiltonian, with adequate next-nearest hopping energy ( $t_2$ ) from Spin-orbit coupling to overcome the open-gap energy ( $M$ ), the topological phase can exist in a honeycomb lattice with Chern number ( $\nu = \pm 1$ ), and the time-reversal protected Hall conductivity from Kondo formula becomes  $\sigma_{xy}^{Spin} = \pm \frac{e^2}{h}$ . As the system is protected by time-reversal symmetry, the spin Hall conductivity consists of two parts and has the opposite sign for spin-up and spin-down electrons. Hence it cannot be detected by the traditional method ( $\sigma_{xy}^{Spin up} + \sigma_{xy}^{Spin down} = 0$ ). To detect this

spin Hall conductivity, Hirsch proposed a “transverse strip” method to manipulate the spin current between a ferromagnet and a paramagnet [62]. This method is later realized experimentally in HgTe/CdTe quantum wells [63].

**3.3.3. Realization of QAHE.** Soon after the observation of the Quantum spin Hall effect, attempts were made to break the time-reversal symmetry in the Haldane model. In the Mn-doped HgTe/CdTe quantum well [64] experiments, as the Mn magnetization is oriented, the magnitude of spin accumulated and resulted in a quantized Hall conductivity:  $\sigma_{xy}^{QAHE} = \sigma_{xy}^{Spin\ up} + \sigma_{xy}^{Spin\ down} = (n + 1) \frac{e^2}{h}$ . However, the Mn spin polarization decays to zero in spin-relaxation time, and the QAHE could only be observed in a narrow time window.

Magnetic doped 3D topological insulators are the next candidates to observe the QAHE for its non-trivial topological inverted band structure and ferromagnetic ordering [65] [66]. Based on first-principles calculations, [42] with fine-tuning of the chemical potential, the Hall conductivity has quantized value  $e^2/h$  and is proportional to  $[n(\uparrow) - n(\downarrow)]$ . The first experimental realization on Magnetic Topological Insulator was achieved in Cr-doped Bi (Sb)<sub>2</sub>Te<sub>3</sub> thin films. [67] The Hall conductivity is quantized to  $\pm \frac{e^2}{h}$  at zero external magnetic fields by applying a gate voltage to tune the Fermi level within the gap. The experiment condition is in the temperature of millikelvin.

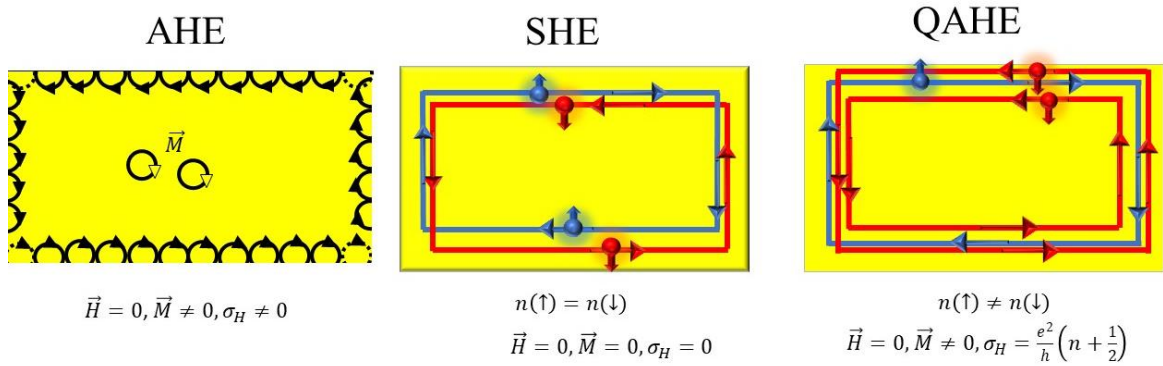


Figure 3-4 Comparison of AHE, SHE, and QAHE

A comparison of the AHE, QSH, and QAHE is described in Figure 3-4. In AHE, the sample maintains a net magnetization and gives rise to a chiral edge current and non-zero hall conductance without an external magnetic field. In SHE, a pair of spin currents in opposite directions is generated by strong spin-orbit coupling, and a spin Hall voltage  $V_{SH}$  would arise transverse to the current and it cannot be detected by the ordinary voltmeter. In QAHE, the ferromagnetism must be large enough to break the time-reversal symmetry, while the system has the spin currents channels from the strong spin-orbit coupling, the Hall voltage can now be measured due to the carrier density difference of spin-up and spin-down electrons.

### 3.4. MAGNETIZATION ANALYSIS

In this section, we report our result on the magnetization measurement on our Cr-doped  $\text{Sb}_2\text{Te}_3$  project. The samples of Cr-doped  $\text{Sb}_2\text{Te}_3$  are prepared with the modified Bridgeman method introduced in Section 2.1.1 and the final product is shown in Figure 3-5. The single crystal was cleaved from the bulk crystal for further measurements.



Figure 3-5 Samples of  $\text{Cr}_{0.2}\text{Sb}_2\text{Te}_3$

The DC magnetic moment of  $\text{Cr}_{0.2}\text{Sb}_2\text{Te}_3$  was measured as a function of temperature with an applied magnetic field of 0.1T and as shown in Figure 3-6 and Figure 3-7. The data was converted to a magnetization by dividing by the samples' mass.

The magnetization transition arises on cooling around 35K, and a 2<sup>nd</sup> order phase transition arises around 180K. This transition is heavily affected by the cooling process of the sample preparation and there is no 2<sup>nd</sup> order phase transition for slow cooling. Additionally, the phase transition is heavily dependent on the cooling speed during the crystallization. For fast cooling, the furnace was shut down and the cooling rate is about 10 degrees Celsius per minute and for slow cooling, the rate is 0.3 degree Celsius per minute.

During the doping in the lamellar crystals, intercalation, and substitution [68] would have an impact on the crystallographic texturization and result in transport

properties differences. The ratio of substitutional and intercalation ions is thermally influenced during the grain boundaries growth.

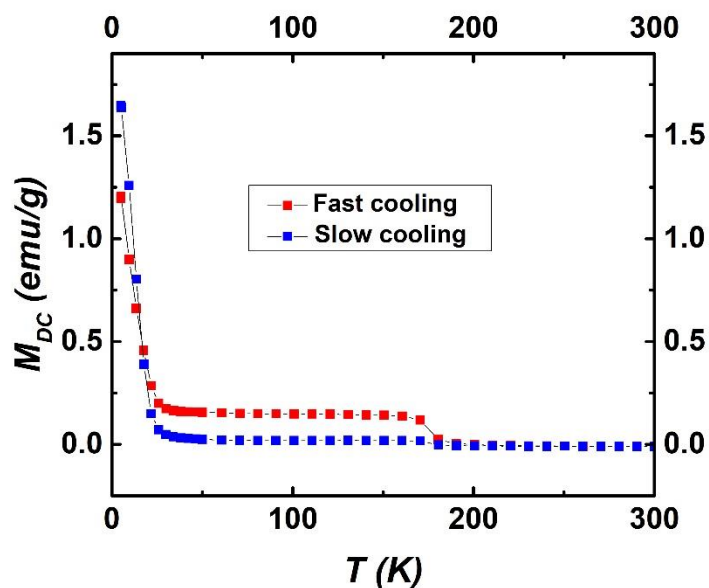


Figure 3-6  $M_{DC}$  vs  $T$  for  $Cr_{0.2}Bi_2Te_3$

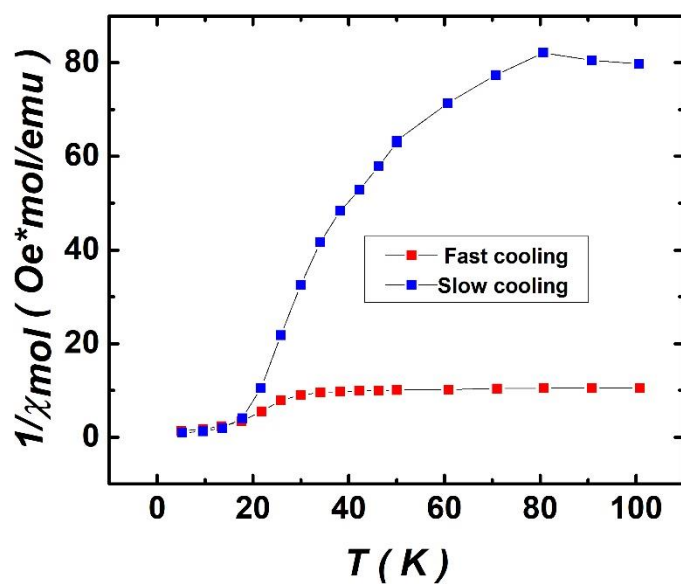


Figure 3-7  $1/X_{mol}$  for phase transition around 35K

It is noted that both substitutional and intercalation are happening during the growth of the  $\text{Cr}_x\text{Sb}_2\text{Te}_3$  bulk crystal, and we can apply the Curie-Weiss Law  $\frac{1}{\chi_{mol}} = \frac{T}{C} - \frac{\theta}{C} = MT + B$  on  $1/\chi_{mol}$  and linear fit [69], the results are shown in Table 3-1.

Table 3-1 linear fitting for different cooling speeds

	Fast Cooling	Slow Cooling
M(slope)	0.4897	1.899
B(intercept)	2.6615	-25.3
C	2.042	0.527
$\theta$	5.435	13.322
$\mu_{eff}$	4.042	2.053
Phase Transition	Anti-ferromagnetism	Ferromagnetism

It can be concluded that slow cooling during crystal growth has a better chance of introducing ferromagnetism into the systems. Hence, for the rest of the data, all samples are prepared using slow cooling during the Modified Bridgman method using a rate of 0.3 degree Celsius per minute.

The next investigation is to change the ratio of substitutional and intercalation ions by changing the stoichiometric ratio of the sample. The Tellurium concentration is reduced from 3 to 2.9 in  $\text{Cr}_{0.2}\text{Sb}_2\text{Te}_3$ . By reducing the stoichiometric amount of Tellurium before sealing the quartz ampoule, their XRD patterns show no significant difference. However, the magnetic properties and Hall effect behave differently in our in-situ samples.

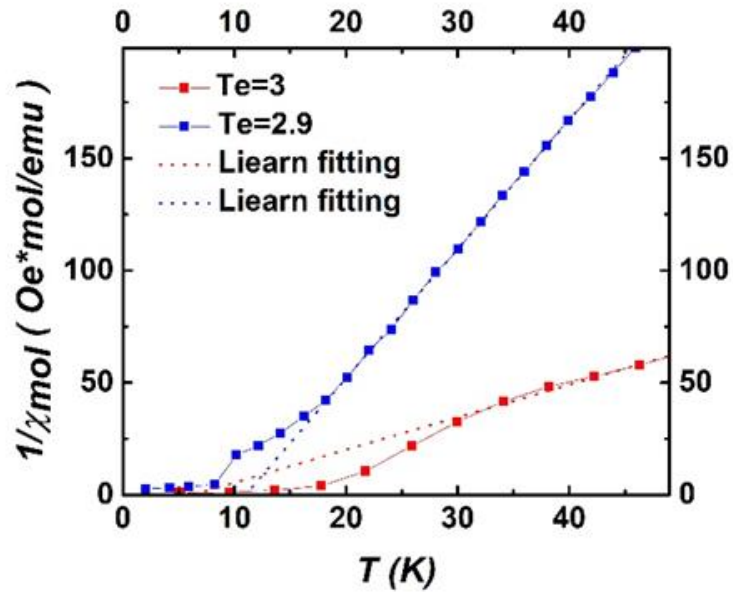


Figure 3-8  $1/\chi_{mol}$  Comparison of  $\text{Cr}_{0.2}\text{Sb}_2\text{Te}_3$  and  $\text{Cr}_{0.2}\text{Sb}_2\text{Te}_{2.9}$

A comparison of  $\text{Cr}_{0.2}\text{Sb}_2\text{Te}_3$  and  $\text{Cr}_{0.2}\text{Sb}_2\text{Te}_{2.9}$  Curie-Weiss Law is compared in Table 3-2 and Figure 3-8. In the  $\text{Te} = 2.9$  sample, with the same doping concentration of  $\text{Cr}=0.2$ . Each tested sample is prepared with the slowest cooling rate of  $0.3\text{C}/\text{min}$  for the ferromagnetic phase transition in the paramagnetic region. The effective magnetic moment per Cr atom is reduced from  $2.347\mu_B$  to  $1.179\mu_B$  on the ferromagnetic phase with the Curie temperature increases from  $T_C = 6.170\text{K}$  to  $10.974\text{K}$ . This suggests that ferromagnetism still exists during the Te concentration changes, which is agreed with the results on thin film [70].

Figure 3-9 shows the DC magnetization versus Magnetic field results at  $5\text{K}$ . A ferromagnetism transition shows a clear hysteresis loop for  $H//c$ , this hysteresis loop is found to vanish at a temperature above  $20\text{K}$ . The coercivity at  $T=5\text{k}$ ,  $H_c \sim 250\text{Oe}$ , indicates that the sample is a soft ferromagnet and it is completely untraceable for  $H//ab$ .

It is noticed the starting point for the measurement at zero magnetic field is off center, and this is most likely due to the trapped field with the PPMS superconducting coil.

Table 3-2 linear fitting for different Te concentrations

	Te = 3	Te = 2.9
M(slope)	5.756	1.4519
B(intercept)	-63.169	-8.958
C	0.17373	0.68875
$\theta$	10.97446	6.16985
$\mu_{eff}$	1.17892	2.34734
Phase Transition	Ferromagnetism	Ferromagnetism

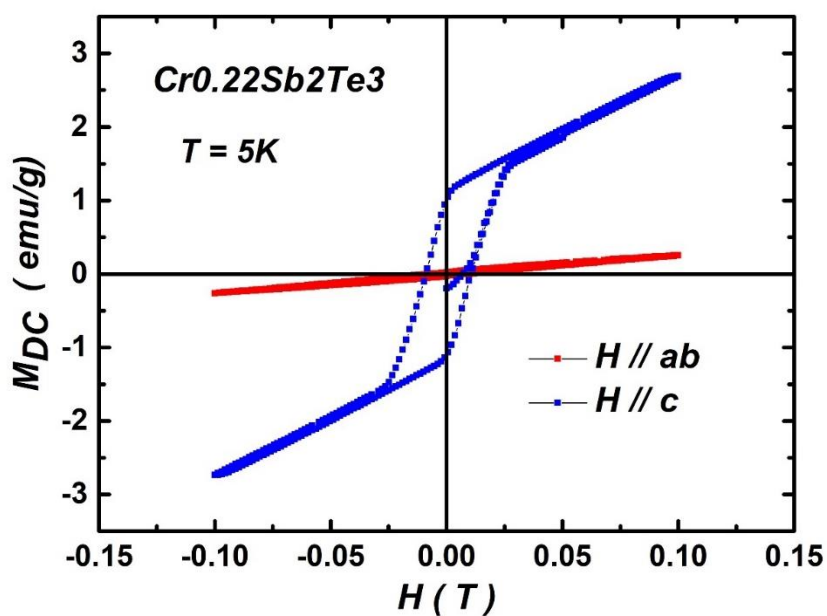


Figure 3-9 DC magnetization for Cr<sub>0.22</sub>Sb<sub>2</sub>Te<sub>3</sub>

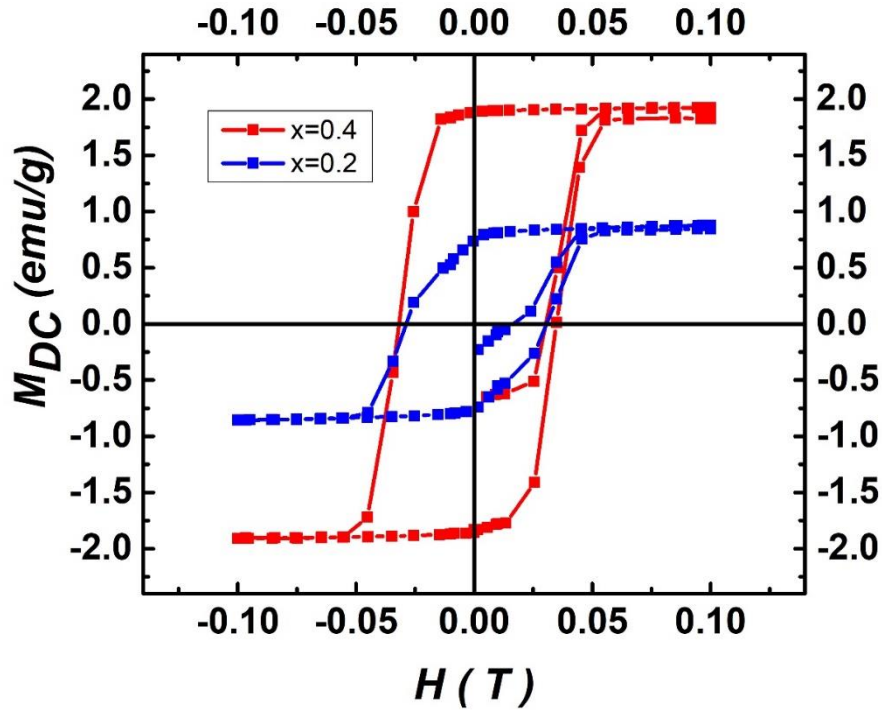


Figure 3-10 Magnetic hysteresis for  $\text{Cr}_x\text{Sb}_2\text{Te}_3$  with different Cr concentrations

As seen in Figure 3-10, the coercivity increases to 500 Oe at  $T=2\text{K}$  and shows no difference for different Cr concentration. This implies the change of chemical potential has no significant effect on ferromagnetism and the Bloembergen-Rowland (BR) mechanism dominates the origin of ferromagnetism.

### 3.5. HALL EFFECT ANALYSIS

This section reports the result on the Hall measurement on the Cr doped  $\text{Sb}_2\text{Te}_3$  project. The Hall resistance  $R_{xy} = \frac{V_y}{I_x}$  is measured at  $T=2\text{K}$  and both fast-cooling and slow-cooling samples are compared in Figure 3-11. An Anomalous Hall effect with zero Hall resistance is observed in both samples. From the fast-cooling sample to the slow-

cooling sample, the hall resistance is increased from  $0.0404 \times 10^{-3}$  ohm to  $0.107 \times 10^{-3}$  ohm while the carrier density is reduced from  $6.447 \times 10^{20}$  to  $5.099 \times 10^{20} / \text{cm}^3$ . In another word, the hall resistance is in the negative correlation of the carrier density and the fast cooling impairs the anomalous hall effect and has a higher carrier density but a lower zero-field Hall resistance.

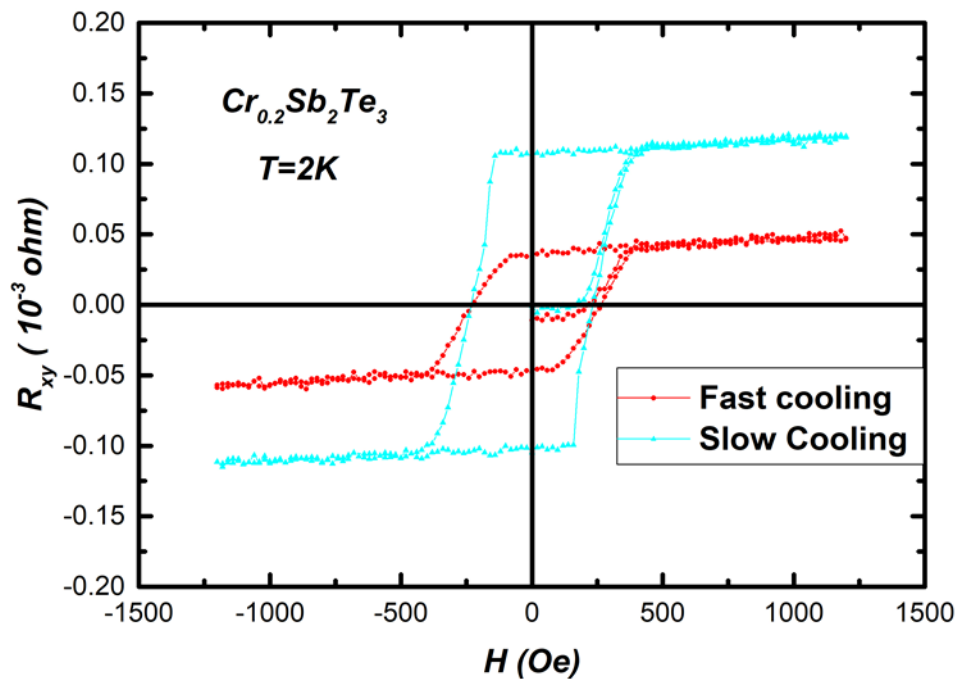


Figure 3-11 Anomalous Hall effect for  $\text{Cr}_{0.2}\text{Sb}_2\text{Te}_3$

Within the slow-cooling samples, an n-type  $\text{Cr}_{0.2}\text{Sb}_2\text{Te}_{2.9}$  has been discovered. The appearance of this n-type sample exhibits a dramatic random change and only appears in one of the five tested samples from the same synthesis patch. This could result from the different ratios of intercalation and substitution ions. And the single crystals tested n-type are selected from the bulk p-type sample.

It has been reported with Bi doping at the Sb sites,  $\text{Cr}_x(\text{Bi}_y\text{Sb}_{1-y})_2\text{Te}_3$  thin film could change its carrier type from p-type to n-type [70] with anomalous hall effect. In-situ hall resistivity is measured at various temperatures and the negative slope in hall resistivity indicates with  $\text{Cr}_{0.2}\text{Sb}_2\text{Te}_{2.9}$  is dominated by n-type carriers.

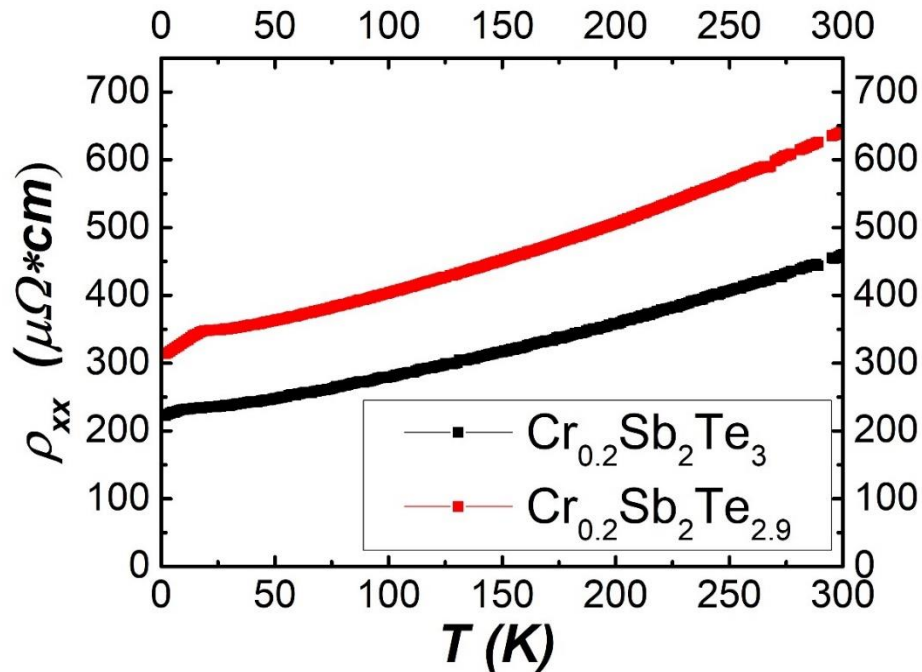


Figure 3-12 Resistivity comparison For  $\text{Cr}_{0.2}\text{Sb}_2\text{Te}_3$  and  $\text{Cr}_{0.2}\text{Sb}_2\text{Te}_{2.9}$

In Figure 3-12, there is a noticeable drop in the longitudinal resistivity  $\rho_{xx}$  around 35K. This marks the boundary between the QAH insulator and AH insulator phases.

[56]It has been studied that the longitudinal resistivity  $\rho_{xx}$  is affected by the magnetic disorder and could cause an isothermal magnetization step related to the timescale for re-equilibration for quantized hall resistance. [71]With the shorter time scale for re-equilibration,  $\text{Cr}_{0.2}\text{Sb}_2\text{Te}_{2.9}$  is a better candidate for observing the QAHE.

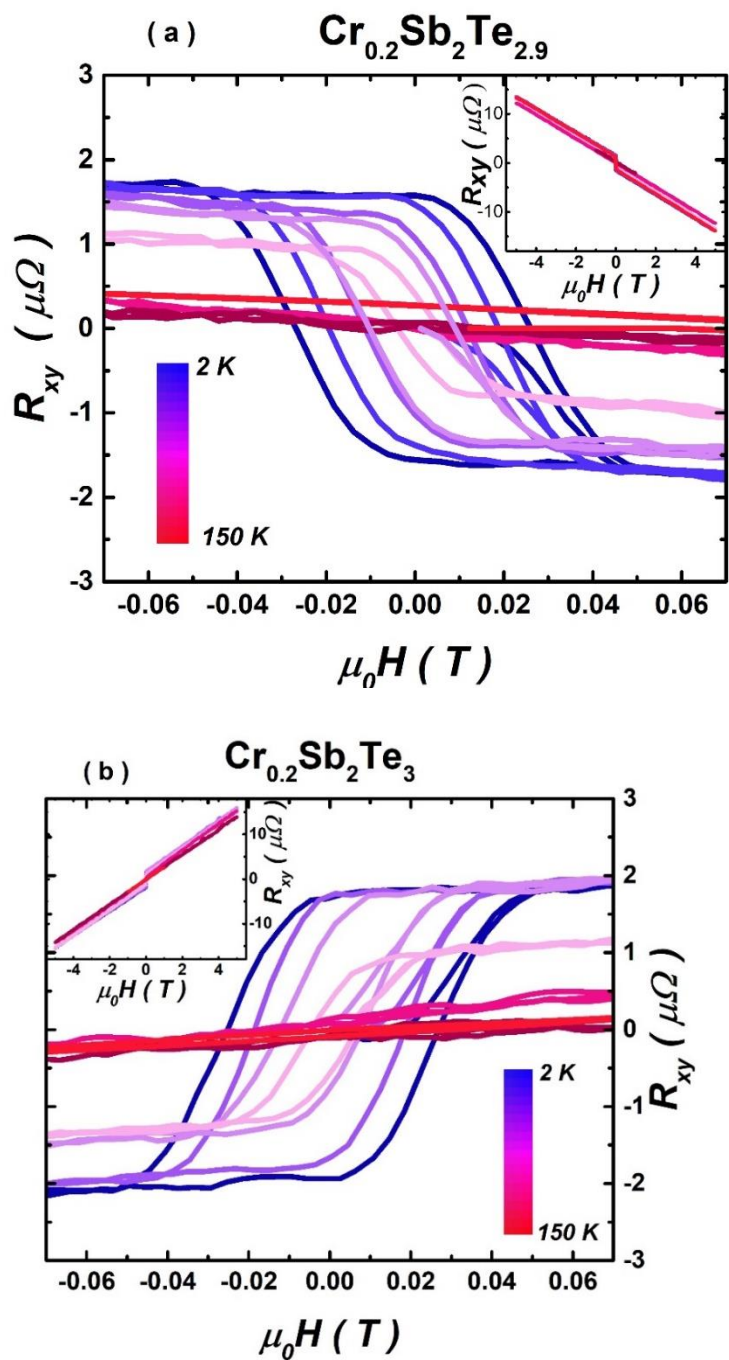


Figure 3-13 Hall resistance: (a)  $\text{Cr}_{0.2}\text{Sb}_2\text{Te}_{2.9}$  (b)  $\text{Cr}_{0.2}\text{Sb}_2\text{Te}_3$

Figure 3-13 shows the Hall resistance up to 5T at various temperatures. Both tested single crystals are cut into the same size for measurement and measured at the same time. The dimensional error is less than 0.01mm.

In the low magnetic field region, the Anomalous Hall effect is observed at zero magnetic fields with a non-zero Hall resistance, and the hysteresis-like loop vanishes at temperatures above 20K.

One distinguishing difference between the p-type and n-type Anomalous Hall effect is that non-zero hall resistance at zero magnetic fields. This non-zero hall resistance remains the same until the 20K for p-type, while it immediately reduces as temperature increases.

From the direction of the slope, we can conclude for  $\text{Cr}_{0.2}\text{Sb}_2\text{Te}_3$ , the carriers' type is p-type, this is because the Fermi level of naturally grown  $\text{Sb}_2\text{Te}_3$  lies in the bulk valence band continuum and does not cut through the surface states due to a high level of intrinsic doping [72].

Several attempts [73] [74] have been made to tune the fermi level of  $\text{Sb}_2\text{Te}_3$  into the conduction band for the observation of the Dirac surface state, but none had succeeded. However, in our selected single crystals from the  $\text{Cr}_{0.2}\text{Sb}_2\text{Te}_{2.9}$  bulk crystals, a negative slope in the Hall resistance implies the carriers' type is n-type.

In the high magnetic field region, the hall resistance has been linear fitted to get the carrier density, as shown in Figure 3-14. On the p-type  $\text{Cr}_{0.2}\text{Sb}_2\text{Te}_3$  the carrier density is thermally stable, but on the n-type  $\text{Cr}_{0.2}\text{Sb}_2\text{Te}_{2.9}$  fluctuates with temperature.

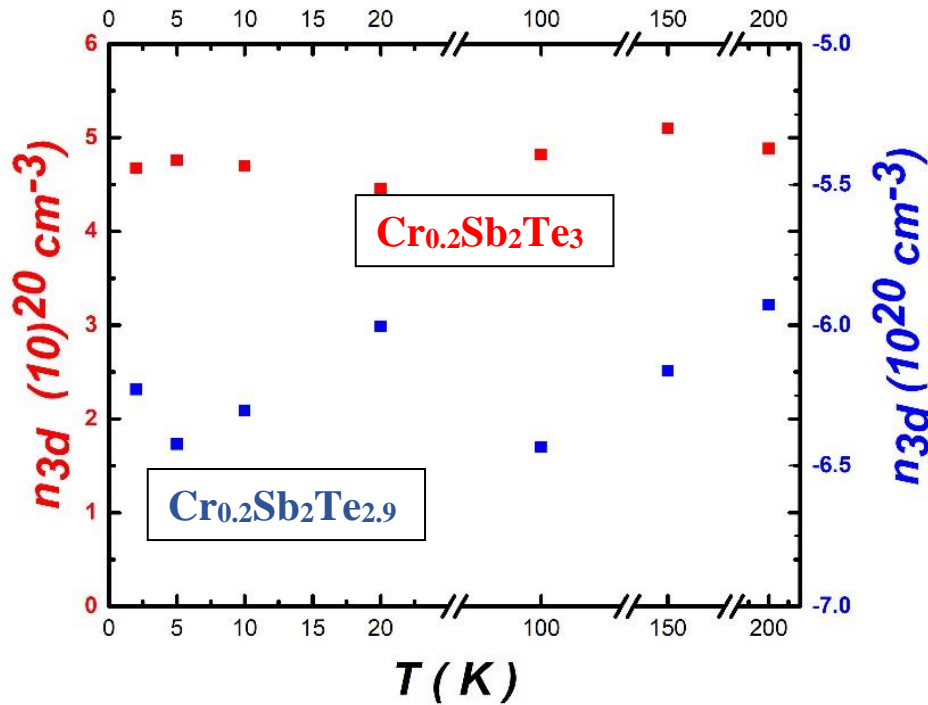


Figure 3-14 Carrier density for  $\text{Cr}_{0.2}\text{Sb}_2\text{Te}_{3/2.9}$

It should be noted that the carrier density value can only be treated semi-quantitatively because they are determined by the hall voltage equation  $V_H = \frac{I_x B_z}{nte}$ , where  $t$  is the thickness and  $R_{xy} = \frac{V_H}{I_x}$  in the high magnetic field region. Also, the charge carrier density is almost constant [67] with temperature in the previously reported Cr-doped magnetic topological insulator micro flakes.

The cause of the n-type remains uncertain and possible mechanisms fall into three categories:

- During the sample preparation for the test, Chromium compounds ( $\text{Cr}_2\text{O}_3$ ,  $\text{Cr}_3\text{O}_4$ ) are most likely formed on the cleaved surface, especially the stepwise oxygen-evolving reactions related to  $\text{Cr}_2\text{O}_3$ , it is noted that  $\text{Cr}^{4+}$

ion is formed at the reported X-ray diffraction. [75] While  $\text{Cr}_2\text{O}_3$  is an oxygen-excess semiconductor, it is found the addition of  $\text{M}^{4+}$  ion impurity can reduce the number of acceptor states and lead to n-type conduction. [76] In addition, although samples with the visible green region is discarded for further measurements, non-visible  $\text{Cr}_2\text{O}_3$  would still be in contained within the tested sample.

- Another possible cause for the n-type is due to the small band gap ( $\sim 0.161\text{eV}$ ) in the  $\text{Sb}_2\text{Te}_3$  systems. Phase transition for  $\text{Sb}_2\text{Te}_3$  has been reported by pressure [77] Respectively, recent reports show a novel strategy of engineering the van der Waals heterostructure and lead to different band structures for Cr-involved layer materials. [78] The single crystal extracted from the slow-cooling sample is extremely soft and can be deformed easily. While preparing the single crystal for measurement, multiple cleavages are necessary for the perfect rectangle shape. And this may be the random appearance of the n-type conduction.
- It has been reported the tellurium gas pressure during crystal growth can change the conductivity of cadmium telluride ( $\text{CdTe}$ ) from p-type to n-type [79]. It is unfortunate that no detailed theoretical analysis of the results. In the Modified Bridgeman method, the vacuum quartz ampoule can create tellurium gas beyond the melted liquid during the heating process. Even though a stoichiometric mixture of elements is put into the quartz tube before sealing, the heating time and the volume of the quartz ampoule can cause various tellurium gas pressure as the crystal chuck is

growing. This causes an alternating ratio of substitution and intercalation doping effect during the crystal growth. And this ratio can be triggered with Te deficiency scenario.

## 4. TOPOLOGICAL SUPERCONDUCTORS

Shortly after the experimental realization of TI, TSC emerges without any notice. The Cu-doped  $\text{Bi}_2\text{Se}_3$  shows type II superconductivity while preserving the non-trivial topological nature in its host. The TSC preceded the theoretical understanding of the topological quantum systems and combine the properties of superconductor and topological materials and is predicted to be the perfect candidate for experimental realization of Majorana Fermions. [80]

### 4.1. MAJORANA FERMION

In 1928, Dirac predicts the existence of positrons, which has the same mass but opposite charges with electrons, and when a positron collides with an electron, the pair can annihilate each other and produce photons. The concept of antiparticle reveals the symmetry in the laws of nature and enlightens every researcher, especially those who work in particle physics.

In 1937, Majorana found that the eigenstates for Dirac equations  $|\psi_1\rangle$  and  $|\psi_2\rangle$  can be arranged in the following mathematical transformations:

$$|\varphi_1\rangle = \frac{1}{2}(|\psi_1\rangle + i|\psi_2\rangle), |\varphi_2\rangle = \frac{1}{2}(|\psi_2\rangle - i|\psi_1\rangle) \quad (1)$$

and the new eigenstates still obey the Dirac equation:

$$i\frac{\hbar}{c}\partial_t\psi(x, t) = [-i\hbar\alpha \cdot \partial_x + \beta mc]\psi(x, t) \quad (2)$$

where  $m$  is the mass of a particle, and  $\alpha$  and  $\beta$  are  $4 \times 4$  matrices obeying the anti-commutation relations. And now the new eigenstates have

$$|\varphi_1\rangle = |\varphi_2\rangle^* \text{ and } |\varphi_2\rangle = |\varphi_1\rangle^* \quad (3)$$

These self-conjugate eigenstates suggest the particles in this state are their antiparticles. Considering the nature of the Dirac equation, some existing spin  $\frac{1}{2}$  particles could be their antiparticles with high energy. And these fermions are called Majorana Fermions. These conditions are naturally met in TSC, it has been proposed that TSC could be the possible host of such particles. [81] The gapless surface state in TSC has a linear dispersion relation that obeys the Dirac equation. and in the superconducting state, the Cooper pair formed near the topological defect can contain magnetic flux tubes and alter the equations for the electrons. In particular, [82] systems with Cooper pairs with orbital angular momentum  $l = 1$  ( $p = p_x + ip_y$  -wave) or for s-wave Cooper pairs with Dirac-like electrons, would mostly be likely to host the Majorana Fermions.

## 4.2. SUPERCONDUCTIVITY

Superconductor was first observed in 1911 when its resistance suddenly disappeared after being cooled down to the temperature of liquid helium. [83]The first significant milestone in understanding this behavior is the discovery of Meissner effect in 1933 [84]This section will introduce widely accepted concepts with our experiment confirmation of the  $\text{Nb}_x\text{Bi}_2\text{Se}_3$  superconductivity.

**4.2.1. Meissner Effect.** Meissner Effect is a miraculous levitation phenomenon in which a superconductor floats on a magnet when the superconductor (SC) is cooled down at a temperature below its transition temperature ( $T_c$ ). In some literature, this transition temperature is also called critical temperature. The mechanism for Meissner effect were explained through the magnetic flux model and shown in the Figure 4-1.

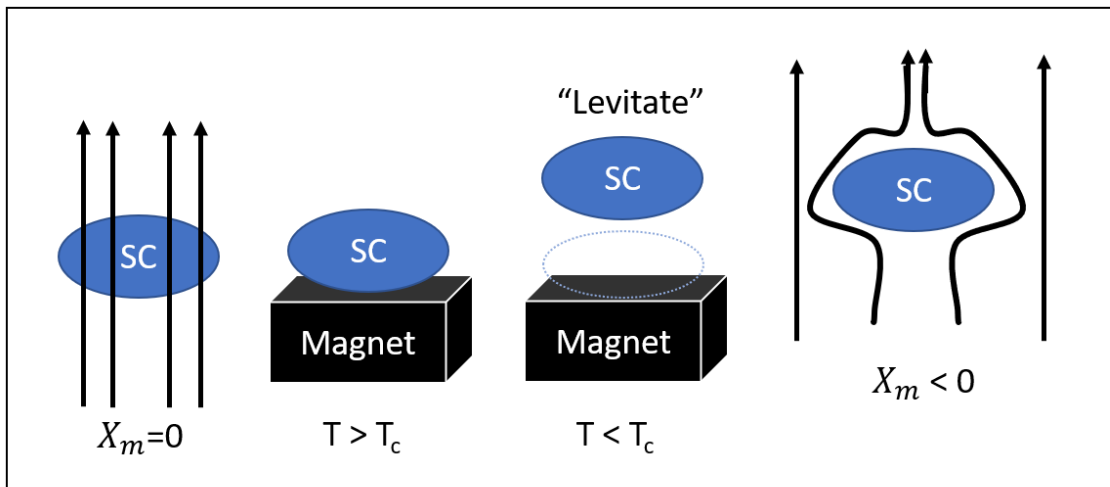


Figure 4-1 Magnet Flux model for Meissner effect

When the temperature is below  $T_c$ , in the presence of an applied magnetic field, internal magnetic vortices will form and “expels” the external magnet flux. The superconductor becomes a perfect diamagnetic material, and it could generate a repelling force against the magnet to overcome gravity. As the temperature is raised above  $T_c$ , these vortices start to disappear and allow the external magnet flux to penetrate the superconductor. As a direct result, the magnetic susceptibility ( $X_m$ ) for SC will be perfect zero and the levitation phenomena disappear.

**4.2.2. Type II Superconductor.** Based on the magnetic response of the Meissner effect, superconductors are classified into Type-I SC and Type-II SC. They both have the Meissner effect and have zero resistance below their  $T_c$ . As shown in Figure 4-2, the Type-II SC has two critical fields (upper and lower), while Type-I SC only has one.

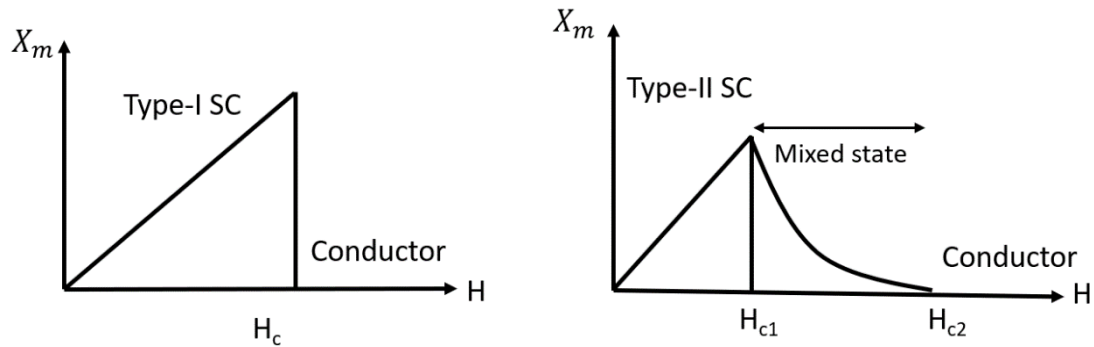


Figure 4-2 Comparison of Type-I and Type-II superconductors

In Type-I SC, the Meissner state breaks down when the applied magnetic field reaches the critical field ( $H_c$ ). It perfectly obeys the Meissner effect perfectly and becomes a conductor after  $H_c$ .  $H_c$  is normally in the range of few-Gausses and Type-I SC are also known as soft superconductors for this reason. Type-I SC materials are mostly pure metals, and some are covalent superconductors. [85]

In Type-II SC, when the applied magnetic field is between the upper and lower critical field ( $H_{c1} < H_0 < H_{c2}$ ), a mixed-state Meissner Effect is present. In this state, the magnetic field inside the SC is given by  $H(x) = H_0 \exp\left(-\frac{x}{\lambda_L}\right)$ , where  $\lambda_L$  is the London penetration length and characterizes the distance to which a magnetic field penetrates a superconductor [86]

**4.2.3. P-wave Superconductivity.** As Cooper pairs are formed with  $2N$  spin  $\frac{1}{2}$  ( $m_s = \pm \frac{1}{2}$ ) electrons, the total angular momentum  $l$  can only take the value of  $0, 1, 2, 3, \dots$  In analogy with atomic orbitals, Cooper pairs having  $l = 0, 1, 2$  are called s-wave, p-wave, and d-wave, respectively. [80] In addition, the s-wave and d-wave are spin-singlets, while

the p-wave is spin-triplets. The potential for spin-singlets and spin-triplets has different Hamiltonian expressions due to the sensitivity of electron correlation and it could be essential for understanding the unconventional superconductivity [87] The superconductivity of the cuprates is now confirmed to be d-wave and the topological superconductor is confirmed to be p-wave. [88]

**4.2.4. Experiment Confirmation.** To confirm the superconductivity in our  $\text{Nb}_{0.25}\text{Bi}_2\text{Se}_3$ , we measure the resistivity and the Meissner effect (see in Section 4.4.1.). The resistivity measurement is done on the PPMS using a 4-probe resistivity measurement. The longitudinal resistivity  $\rho$  vs temperature  $T$  at zero applied magnetic fields is shown in Figure 4-3. The superconducting transition starts at 3.6K on cooling and drops to zero at 3.2K within the PPMS experiment section. From room temperature to 3.6K, the sample shows metallic resistivity behavior.

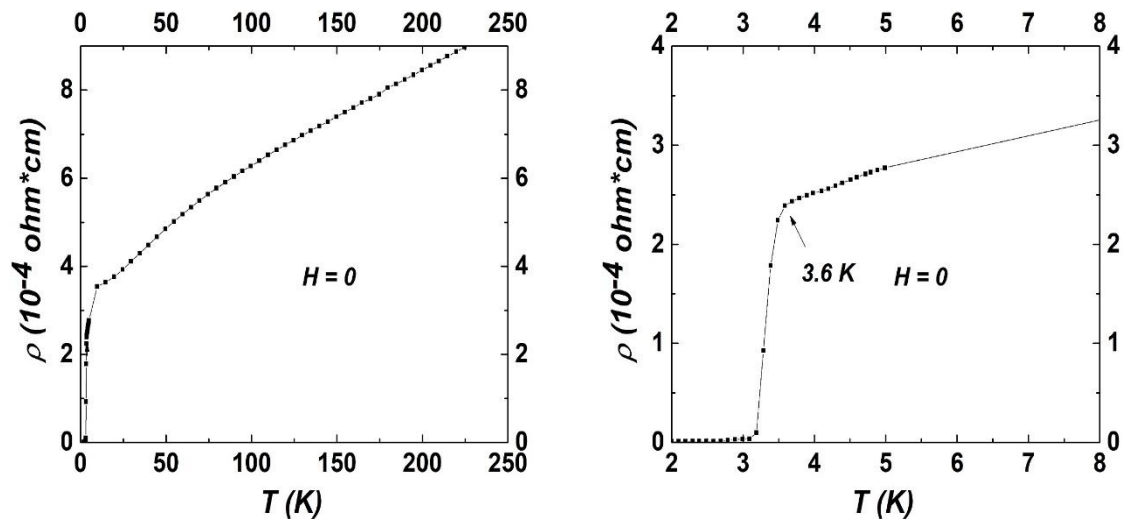


Figure 4-3 Resistivity vs Temperature at zero magnetic fields for  $\text{Nb}_{0.25}\text{Bi}_2\text{Se}_3$

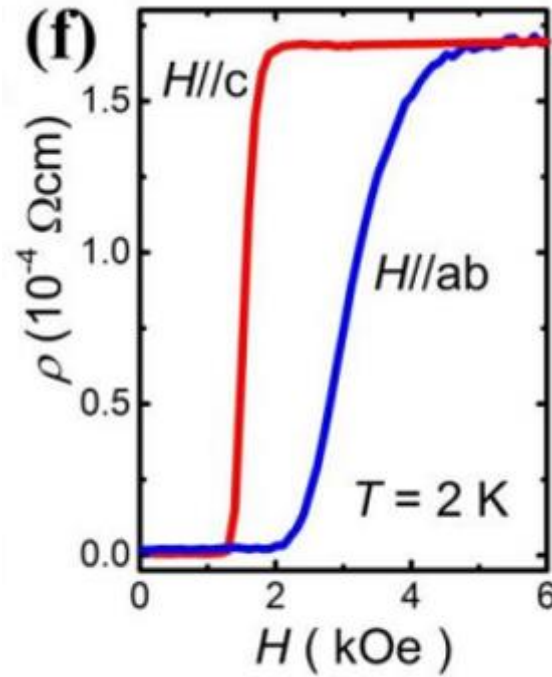


Figure 4-4 Resistivity vs Magnetic field at 2K for  $\text{Nb}_{0.25}\text{Bi}_2\text{Se}_3$

Figure 4-4 shows the longitudinal resistivity vs Applied magnetic field at 2K. An anisotropic behavior is shown for applied fields parallel to the crystallographic c-axis and ab-plane. This anisotropic behavior is expected for layer compounds [89] and implies  $\text{Nb}_x\text{Bi}_2\text{Se}_3$  is a type II superconductor. The upper critical field can be obtained from the empirical condition [90]  $\rho(T) = 0.5\rho_{onset}$  and yields to  $B_{c2//c}(2 K) = \mu_0 H_{c2//c}(2 K) \approx 0.15 T$  and  $B_{c2//ab}(2 K) = \mu_0 H_{c2//ab}(2 K) \approx 0.31 T$ .

Derived from the Werthamer-Halfand-Hohenberg formula, [91], the transition width for  $\rho$  vs  $H$  plot is valid for extrapolation to zero temperature and gives  $B_{c2//c}(0 K) \approx 0.2 T$  and  $B_{c2//ab}(0 K) \approx 0.4 T$ .

Using the Ginzburg-Landau formula for the anisotropic superconductor,

$$H_{c2//c}(0 K) = \Phi_0(2\pi\xi_{ab}^2) \text{ and } H_{c2//ab}(0 K) = \frac{\Phi_0}{2\pi\xi_{ab}\xi_c}, \text{ where } \Phi_0 \text{ is the Flux quantum,}$$

we estimate the ab-plane coherence length  $\xi_{ab} \approx 40nm$  and c-axis coherence length  $\xi_c \approx 20nm$ . Here we conclude the superconducting anisotropy ratio  $\xi_{ab}/\xi_c \approx 2$ .

Respectively, from our collaborators [92], the angular dependence of the superconducting signal shows a periodic pattern with a period of  $60^\circ$  and the effective anisotropy ratio is expected to have a different value from the hexagonal lattice of the sample.

### 4.3. SURFACE STATE

A sketch diagram of the full bulk 3D Brillouin zone (BZ) of  $\text{Bi}_2\text{Se}_3$  is shown in Figure 4-5(a). The Brillouin zone for  $\text{Bi}_2\text{Se}_3$  is with space group  $R\bar{3}m$ .  $k_z$  direction corresponding to the [111] direction. The Four inequivalent time-reversal-invariant points  $\Gamma, L, F, Z$  are labeled. And the high-symmetry k points,  $\bar{\Gamma}, \bar{K}$ , and  $\bar{M}$  are labeled. The APRES data is taken at 12.8K along the  $\bar{\Gamma} - \bar{M}$  direction.

As expected, [93] we found the Dirac surface state at  $\bar{\Gamma}$  point due to the inversion between the conduction band and valence band by SOC. The Fermi level (FL) of the  $\text{Bi}_2\text{Se}_3$  is in the bulk band gap, which differs from the APRES data obtained by the initial discovery [12]. This is because we used the Modified Bridgman method with a different temperature profile and reduce the defects caused by the selenium vacancies. [90]

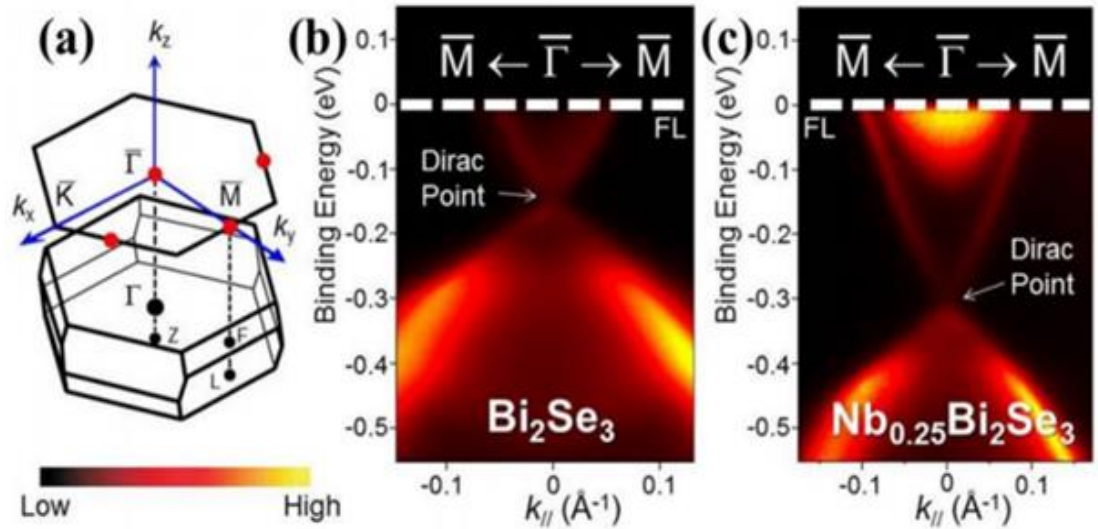


Figure 4-5 ARPES result for TSC

In contrast, the FL of the Nb<sub>0.25</sub>Bi<sub>2</sub>Se<sub>3</sub> is located in the conduction band and a complete picture of the Dirac surface state is observed. This is direct evidence for the retention of non-trivial topological properties after Nb doping. With the relocation of FL, we can conclude that Nb doping introduces excess electrons into Bi<sub>2</sub>Se<sub>3</sub> and turn it into n-type. Remarkably, the relationship between the critical temperature and pressure was measured by one of our collaborators. [94], contrary to the other two known TSCs, the critical temperature continually increases with pressure up to 0.6 Gpa. This indicates the carrier density would be increased with pressure and leading causing more electrons.

The surface band and bulk band do not overlap suggesting the non-degenerate relativistic surface state, which could lead to Andreev-bound states with a finite bulk gap. [95] [96] It is worth noting that through Josephson junction contracts, the spin state of the Dirac surface state can be utilized in quantum information processing devices based on Andreev reflection.

#### 4.4. MAGNETIZATION

During our confirmation of Meissner effect for  $\text{Nb}_x\text{Bi}_2\text{Se}_3$ , a symbiosis of magnetic order and superconductivity is observed. The magnetic order is mediated by superconductivity and gives rise to a zero-field Hall effect. [97] This section will introduce the procedure we use to analyze this symbiosis state.

**4.4.1. AC Meissner Effect.** This is measured in PPMS magnetization AC mode. The applied oscillating magnetic field is 10Oe with 1000Hz.

As shown in Figure 4-6, the AC magnetic moment shows the Meissner effect with a critical temperature of around 3.2K. Upon zero field cooling (ZFC) and field cooling (FC) process, the AC magnetization is overlapping, leading to a superconducting volume fraction close to 100%. This indicates the full sample becomes superconducting and the superconductivity is obtained from single-phase materials.

At the initial discovery of  $\text{Nb}_{0.25}\text{Bi}_2\text{Se}_3$ , the single crystal size is small, and stacks of single crystals are used for measurement, and there are sights of Nb-Se nanostructure as an impure byproduct. Even after remelting the nanostructure byproduct, the AC magnetic moment for a large single crystal has a low magnetic moment. It is plausible to assume that the Nb atoms were not uniformly distributed in the sample due to their high melting point.

A two-step growth method enables the enhanced magnetic moment. The first step is to grow the  $\text{Bi}_2\text{Se}_3$  single crystals using the modified Bridgeman method. A large chunk of  $\text{Bi}_2\text{Se}_3$  single crystal is selected for the second step as a precursor and was added stoichiometric amounts of Nb through a second modified Bridgeman method.

With the 2-step growth method, the Nb-Se byproduct is greatly reduced and the magnetic moment for the Meissner effect is greatly enhanced as shown in Figure 4-7.

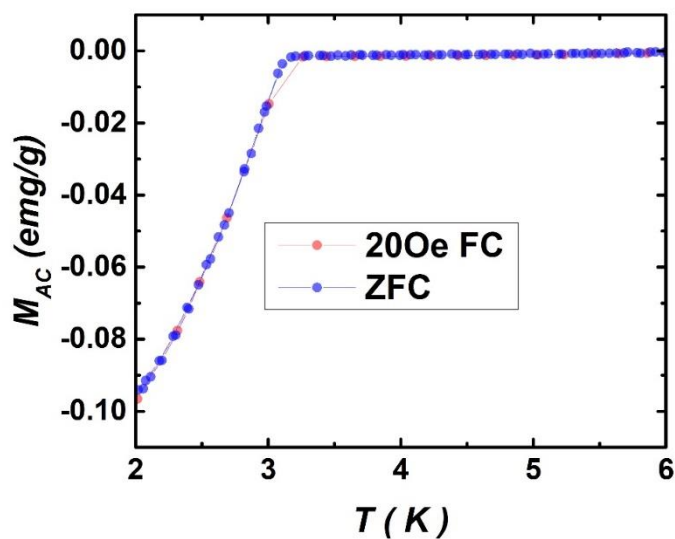


Figure 4-6 AC magnetization for  $Nb_{0.25}Bi_2Se_3$  with FC and ZFC

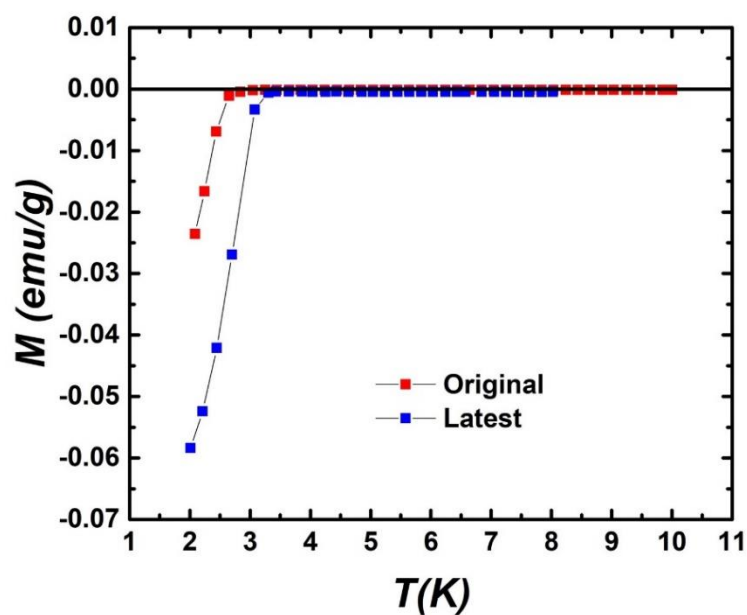


Figure 4-7 AC magnetization for  $Nb_{0.25}Bi_2Se_3$  with 2-step growth method

**4.4.2. Ferromagnetic-like Order.** Figure 4-8 shows the DC magnetization measure for several applied magnetic fields. Upon the field cooling process, interesting phenomena of positive DC magnetic moment appear. A positive DC magnetization is detected at zero magnetic fields. This normally suggests the sample is ferromagnetic. The strength of this DC magnetic moment seems unpredictable at the first discovery.

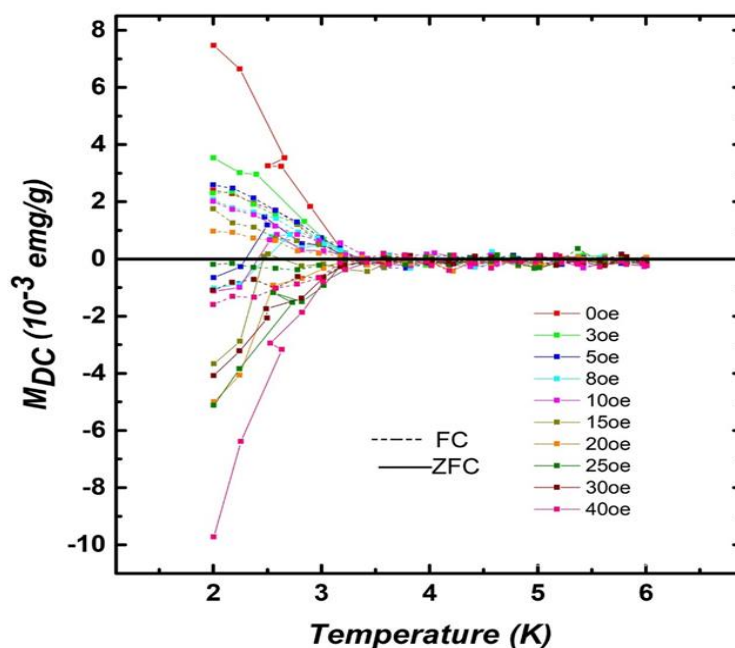


Figure 4-8 DC magnetization for  $\text{Nb}_{0.25}\text{Bi}_2\text{Se}_3$

Ferromagnetism is well known to have a deleterious effect on superconductivity. And yet similar results have been reported in BiPd superconductor with a critical temperature of 4K. [98], and in  $\text{ErNi}_2\text{B}_2\text{C}$  superconductor with a critical temperature of 11K [99].

To solve the speculation of the magnetic history of the sample, we perform a “magnetic field loop treatment” and measure the corresponding DC magnetic moment, as shown in Figure 4-9. The sample is cooled down to 2K at zero magnetic fields. Then DC magnetic moment is measured in a loop of  $0 \rightarrow 17 \rightarrow -17 \rightarrow 17$  with 10Oe per step and forms a magnetic field loop. As a result of the loop treatment, the sample is undergoing a pseudo-AC measurement of 170e with the magnetic moment measured during the oscillation ( $f \ll 1Hz$ ).

From multiple loop treatment, the DC magnetization forms a hysteresis loop and saturates after 5 loops, as shown in Figure 4-9. It is worth noting that the saturated hysteresis loop depends on the magnetic field range. magnetic field loop treatment permits manipulation of the positive DC magnetic moment in Figure 4-8 and allows a ferromagnetic magnetic moment in the superconducting sample.

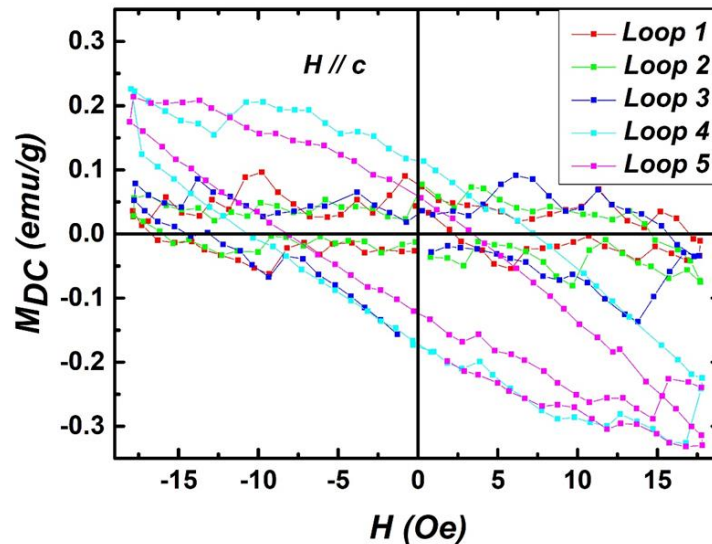


Figure 4-9 Magnetic field loop treatment

To reconcile these two seemingly contradictory results, we performed a combination of AC and DC magnetic moment analysis. The applied AC field strength is varied from 1-17 Oe and the ac magnetic moment is subtracted from the saturated hysteresis loop. As shown in Figure 4-10, the subtracted magnetic moment behaves exactly like the common ferromagnetism hysteresis loop. Thus, Figure 4-10 can be interpreted as a total magnetic moment from the superconductivity and ferromagnetism.  $M_{Total} = M_{AC} + M_{DC} = M_{SC} + M_{FM}$ . Where  $M_{SC}$  is the Messner effect moment and  $M_{FM}$  is the ferromagnetic moment.

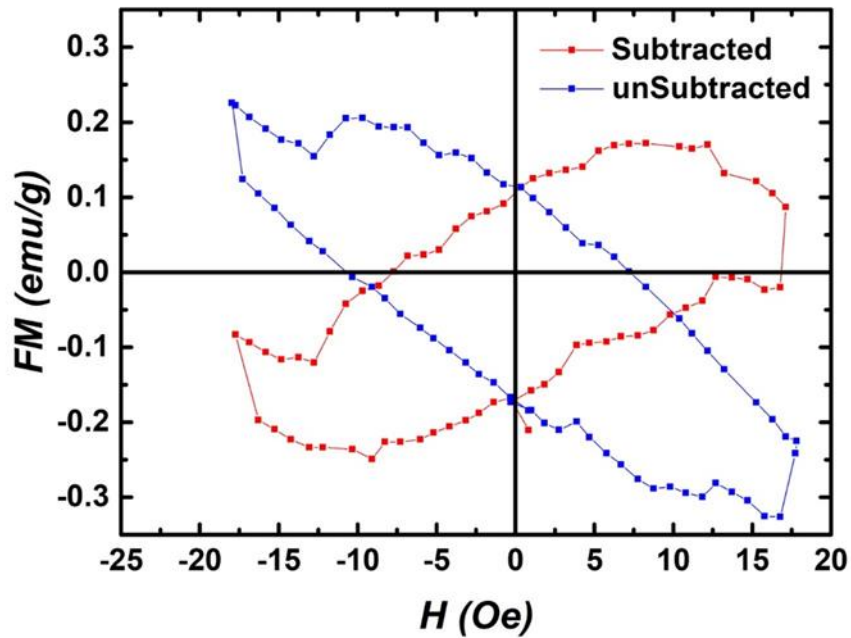


Figure 4-10 Total magnetic moment for  $\text{Nb}_{0.25}\text{Bi}_2\text{Se}_3$

In addition, the Topological Superconductor is related to the p-wave ( $l = 1$ ) superconductor [80] due to the topologically protected surface state. It is a good assumption that the total magnetic moment is due to the Cooper pairs ( $l = 1$ ) taking up

the spin current channel from the strong spin-orbit coupling. In some other theoretical interpretations [100], this formation of Cooper pairs is also referred to as spin-triplets pairing.

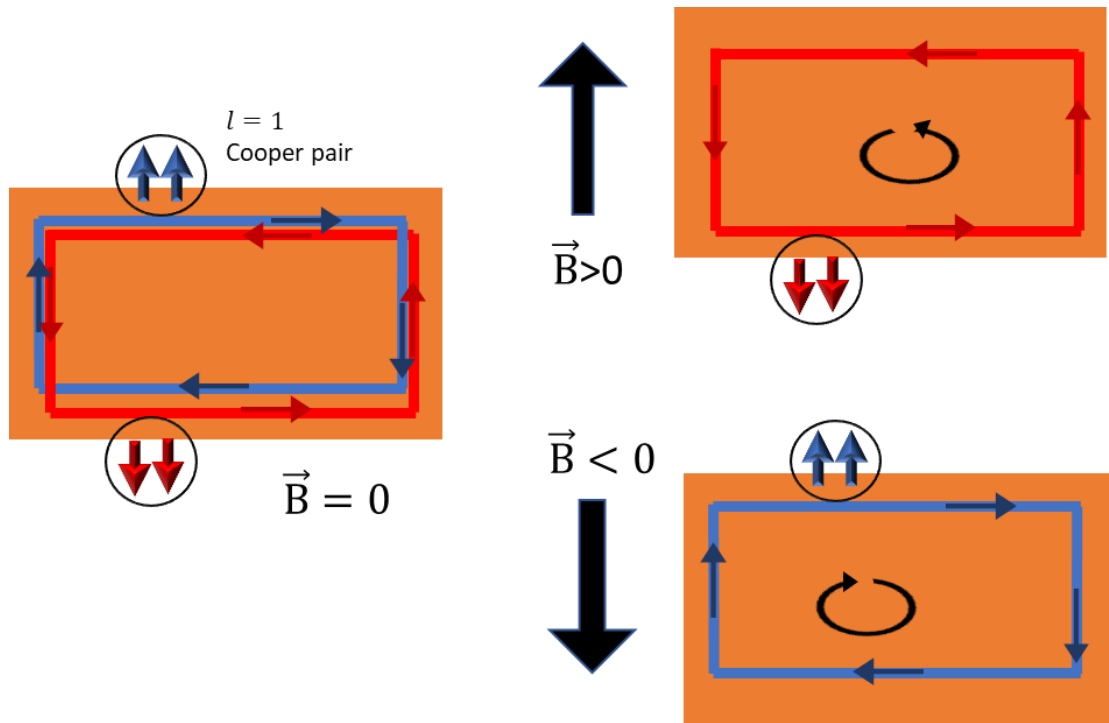


Figure 4-11 The cause of ferromagnetic moment

Figure 4-11 is a schematic explanation for the non-zero DC magnetic moment at zero magnetic fields. The system is protected by time-reversal symmetry and has the current channels for spin-up and spin-down electrons in opposite directions. During the superconducting doping, the electrons are forming cooper pairs ( $l = 1$ ). These Cooper pairs are the sources of the Meissner effect signals. And now the current channels become the Cooper pairs channels for  $l = 1$  and  $-1$ , instead of spin-up and spin-down.

Under the variation of the external magnetic field, the Meissner effect is manifested and causing generates a “vortex current” to repel the external magnetic field. However, this “vortex current” is taking the cooper pair channels. As the Meissner effect increase, more and more cooper channels are taken. Leaving an unbalanced number of cooper channels. And the cooper pairs on the extra channels are now inducing a net magnetic moment in the systems.

#### 4.5. HALL MEASUREMENT

The Hall effect on the superconductor has been studied for the relationship between the Hall coefficient and critical temperature for the nature of the superconducting mechanism. [101] The existing hall resistivity measurements [102] [103] [104] show zero Hall voltage when the superconductor is below the critical temperature and within its lower critical field. However, a novel Hall effect caused by the spin-polarized current in superconductors has been proposed. [105] When spin-polarized electrons flow within the superconductor, they can be deflected by spin-orbit coupling and yield a transverse charge imbalance, and this can produce a Hall voltage. In this proposal, the hall effect on the superconductor will require an injection of Spin current from ferromagnet (FM) through a double FM/SC/FM Josephson junction. Since we observed the coexisting state of superconductivity and ferromagnetism,  $\text{Nb}_x\text{Bi}_2\text{Se}_3$  is a ready-made alternative for this novel Hall effect.

Another spontaneous hall effect is also proposed in the chiral p-wave superconductor. [106] Through the solution of Bogoliubov-de Gennes (B-dG) equation for edge state, a quantized hall resistivity  $\rho_{xy} = \frac{3h}{2\pi^2 T k_B^2}$  would appear in a two-

dimensional superconductor with  $p_x + ip_y$  symmetry. It has been shown that [107] recent theoretical development [108] suggests topological superconductor supports p-wave pairing.

Here we report our Hall measurement results on  $\text{Nb}_x\text{Bi}_2\text{Se}_3$ . The Hall measurement is done on the PPMS using 5-probe Hall measurement. The sample prepared for measurement has been confirmed with the AC Meissner effect for quality insurance. In-situ hall conductivity is taken in AC current mode with 10mA at 2K.

Figure 4-12 shows the in-situ hall resistivity result for applied fields parallel to the crystallographic c-axis and ab-plane at 2K. The hall resistivity  $\rho_{xy}$  shows a non-zero value. Compared to the reported hall resistivity in other SC, this non-zero value is believed to be an exclusive property in TSC and has isotropic behavior.

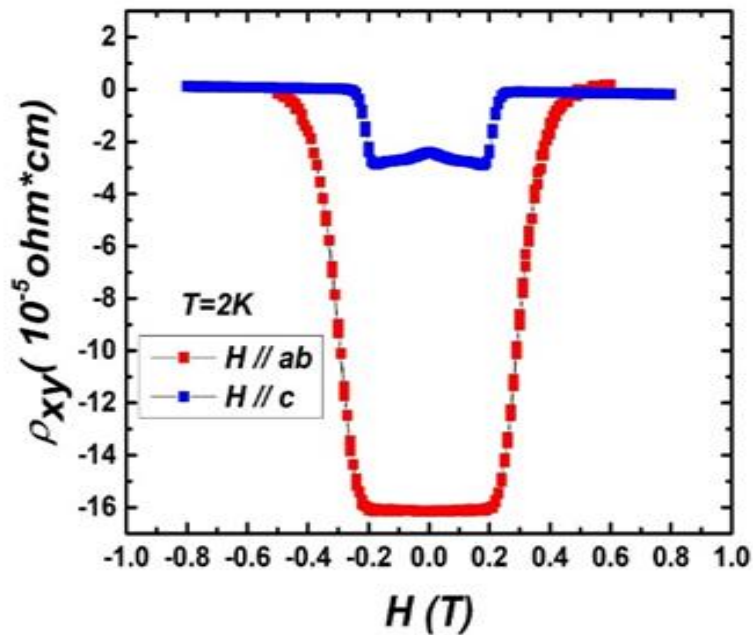


Figure 4-12 Hall resistivity for  $\text{Nb}_{0.25}\text{Bi}_2\text{Se}_3$

To find the correlation between the superconductivity and non-zero hall resistivity, the field strength is divided by the upper critical fields, where  $B_{c2//c}(2 K) = \mu_0 H_{c2//c}(2 K) \approx 0.15T$  and  $B_{c2//ab}(2 K) = \mu_0 H_{c2//ab}(2 K) \approx 0.31T$ .

With this modification, the refined plot is shown in Figure 4-13. The onset and offset for the area now have the same relative transition field strength around  $H/H_{c2} \approx 1$ . This implies the non-zero hall resistivity is strongly correlated with the friction coefficient  $\eta \approx BH_{c2}/c^2\rho$  in Bardeen-Stephen expression [109] in the theory of vortex.

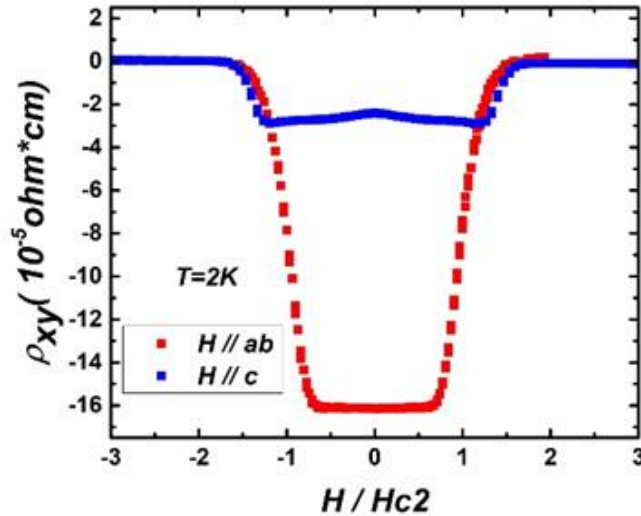


Figure 4-13 Refined Hall resistivity for  $Nb_{0.25}Bi_2Se_3$

To analyze the desired property of this hall data, a phase diagram is constructed similar to the mean-field phase diagram and shown in Figure 4-14. As the temperature and applied magnetic field changes, we define three different phases: A Topological Insulator phase (TI), a Topological superconductor phase (TSC) and a mixed phase of both.

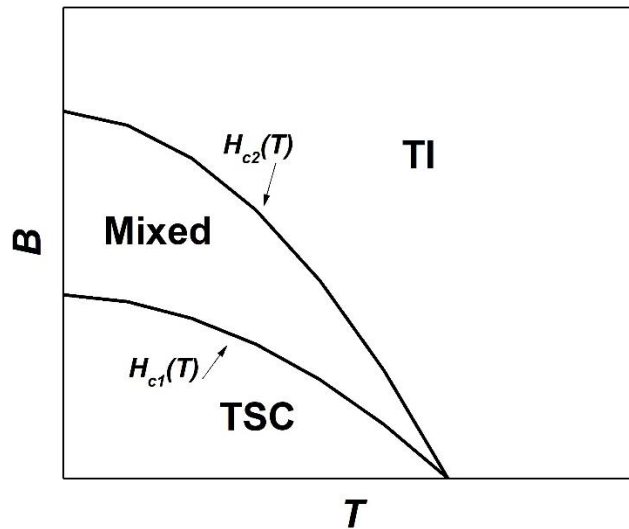


Figure 4-14 Mean-field phase diagram for  $\text{Nb}_{0.25}\text{Bi}_2\text{Se}_3$

A normal Topological insulator phase at high fields and temperatures, separated by the upper critical field line  $H_{c2}(T)$  and the lower critical field line  $H_{c1}(T)$ . At low temperatures and fields, the Topological superconductor phase is present. Within  $-1 \leq H/H_{c2} \leq 1$  below the critical temperature, a mixed phase is present similar to the vortex state in a type II superconductor [109].

To confirm the existence of this spontaneous hall effect, Figure 4-15 shows the comparison of the zero-field hall voltage between the sample  $\text{Nb}_x\text{Bi}_2\text{Se}_3$  and another confirmed type II superconductor  $\text{NbSe}_2$ . The  $\text{NbSe}_2$  is grown in our lab using the iodine-assisted chemical vapor deposition and the measured sample is also confirmed for superconductivity with AC Meissner effect with a critical temperature around 6.8K. Both samples are balanced above their critical temperature.

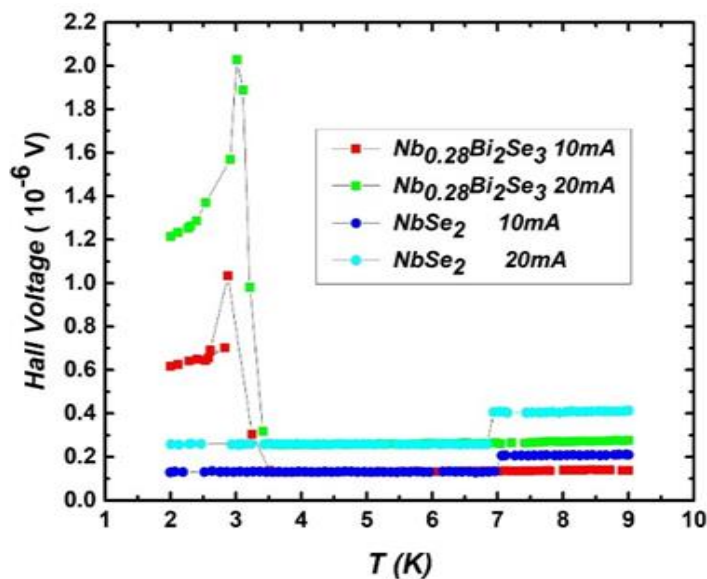


Figure 4-15 Hall voltage comparison with NbSe<sub>2</sub>

As the temperature reached below its critical temperature, NbSe<sub>2</sub> shows zero hall voltage in the absence of an applied magnetic field. This agrees with the previous reports in type II superconductor hall measurement. And there is an increase in hall voltage after the temperature is above the critical temperature. This is due to the imperfect balance in  $R_{xx}$ . However, in the Nb<sub>x</sub>Bi<sub>2</sub>Se<sub>3</sub> sample, in the absence of an applied magnetic field, the hall voltage is zero until the critical temperature. A creep-like increment of Hall voltage appears as the temperature continues to be cooled down below the critical temperature. Following a drop in Hall voltage. This hall voltage is proportional to the applied current and it is noted there is no difference in the applied field direction since the applied magnetic field is zero. It is also noted the warming up and cooling down process results in the same data.

The plot of this hall voltage vs  $T/T_c$  is plotted in Figure 4-16 and shows the non-zero hall voltage only appears in the topological superconductor when  $T < T_c$ . And it is roughly proportional to  $\left(1 - \frac{T}{T_c}\right)^{-1}$ , this suggests the hall voltage is proportional to penetration depth. This creep-like transition to zero implies there is a thermally activated motion of the vortices [110].

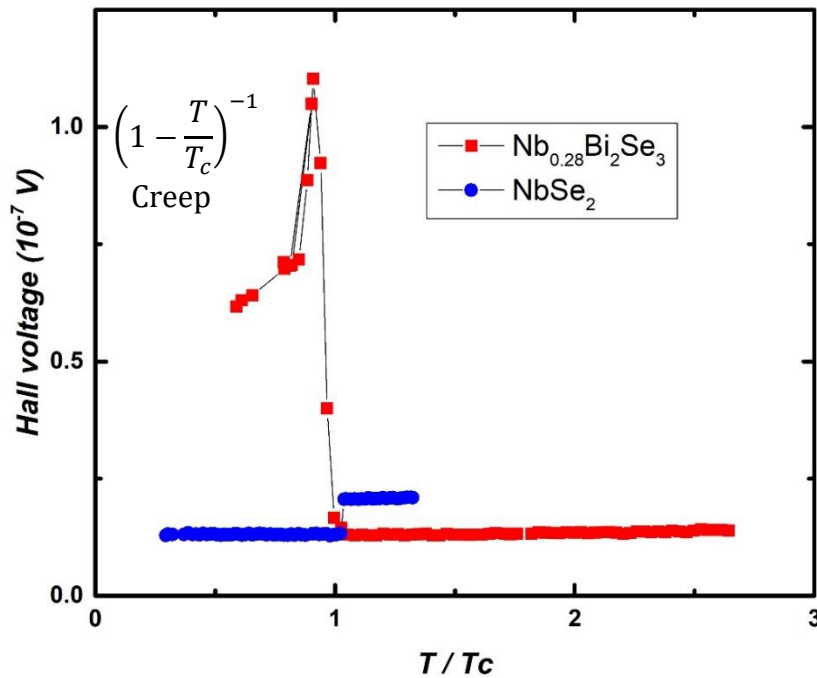


Figure 4-16 Refined Hall voltage comparison

As the bulk of TSC is superconducting and has zero resistance and the surface is still conducting. Here we can assume this non-zero hall voltage must originate from the surface resistance, meaning *this non-zero  $\rho_{xy}$  is the  $\rho_{surface}$* . To be more specific,

electrons from the applied current is taking the vortex line and “diffuse” to the surface.

The schematic picture is shown in Figure 4-17.

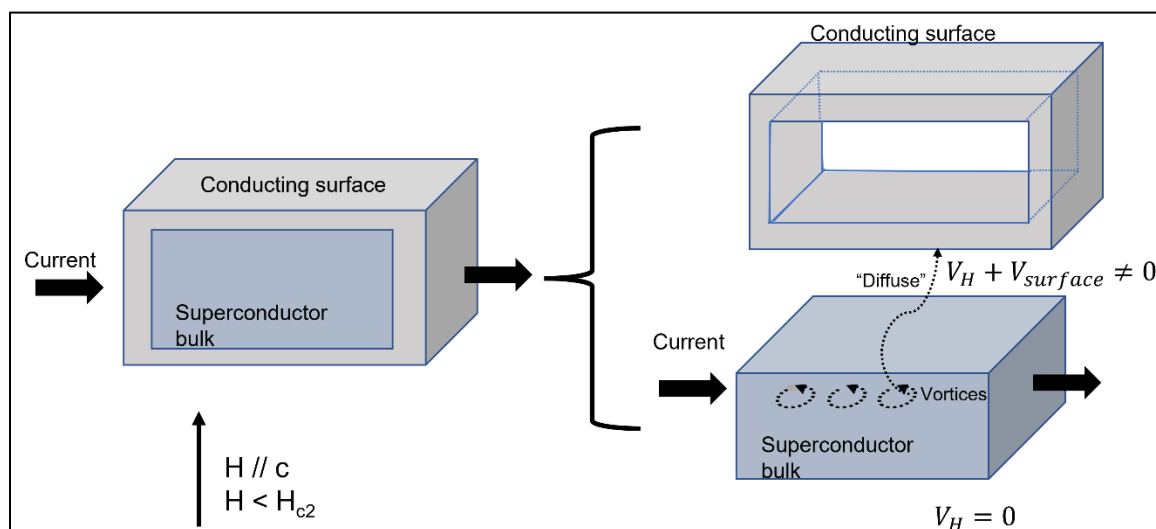


Figure 4-17 Schematic for the cause of non-zero Hall voltage

At this point, we can explain the difference in Figure 4-17 when the magnetic field is applied in the c-axis and ab-plane direction. In H//c, when magnetic field strength increase, the vortex line decreases, and fewer vortices can “diffuse” to the surface and causing an increase in the surface resistance. Hence the “W”-symmetry to applied magnetic fields is compatible with the assumptions.

The vortex line path is confined in the ab-plane due to the Nb atoms are intercalated between the quintuple layers of  $\text{Bi}_2\text{Se}_3$  and cannot diffuse due to crystal orientation. When H//ab, the non-zero hall resistivity is due to the conducting surface resistance.

It is worth mentioning that the Hall effect of TSC should behavior the same as regular TI once the  $H > H_{c2}$  or  $T > T_c$ , but the magnitude difference for the surface resistance is determined by the area of the surface.

## 5. HIGH TEMPERATURE SUPERCONDUCTORS

After the establishment of BCS theory [111], 30K was thought to be the theoretical limit for superconductor critical temperature ( $T_c$ ). Continuous advance has been seen to push this limit with the debut of Cuprite ceramic high  $T_c$  superconductor, and the  $T_c$  for SC has been pushed above the temperature of liquid Nitrogen. Nevertheless, Iron-based superconductors with  $T_c$  up to 43K were reported [112] and this non-copper oxide high  $T_c$  superconductor inevitably expands the framework for the future theoretical mechanism. [113] [114]

With the great potential of reducing energy consumption and the current tendency of modern technology development, room temperature  $T_c$  superconductor is and will always be the pursuit of perfection in the research field of condensed matter physics. Up to now, the superconductor with the highest critical temperature is around 203K at 150GPa. And yet the mechanism behind high  $T_c$  superconductor is still under indefatigable exploration. To verify the booming candidates, bloomers and fantastic methods would be essential to reveal this mystery.

### 5.1. $\text{CuO}_2$ PLANE

Perovskite  $\text{YBaCu}_3\text{O}_{9-\delta}$  (YBCO) [115] shows zero resistance near 90K, and despite world-wide efforts in the past decades, the physics community has still not reached a consensus on what causes  $T_c$  so high [107]. Both oxides-based cuprate superconductors have a particular structure—the  $\text{CuO}_2$  planes. This coincidence can help uncover the elusive superconductivity mechanism in these high-temperature

superconductors [116]. Possible mechanisms from  $\text{CuO}_2$  planes are under considerable debate and further research.

Polycrystalline pellets of the YBCO were initially fabricated by solid-state reaction of the constituent oxides. Later, the single crystals of  $\text{YBa}_2\text{C}_3\text{O}_{7-\delta}$  [117] and  $\text{La}_{2-x}\text{Sr}_x\text{CuO}_4$  (LSCO) [118] are obtained with the flux method. The study on single crystals reveals their highly anisotropic electrical properties. [119] Although the temperature dependence of  $\rho_{ab}$  shows metallic in most cases,  $\rho_c$  exhibits a marked change in magnitude with changing hole concentration. Additionally, the anisotropy  $\rho_c/\rho_{ab}$  varies from 1700 ( $T_c \sim 60\text{K}$ ,  $y \sim 0.18$ ) to 70 ( $T_c \sim 90\text{K}$ ,  $y \sim 0$ ) for  $\text{YBa}_2\text{C}_3\text{O}_{7-\delta}$  and from 8000 ( $T_c \sim 25\text{K}$ ,  $x \sim 0.08$ ) to 100 ( $T_c \sim 4.2\text{K}$ ,  $x \sim 0.34$ ) for  $\text{La}_{2-x}\text{Sr}_x\text{CuO}_4$ .

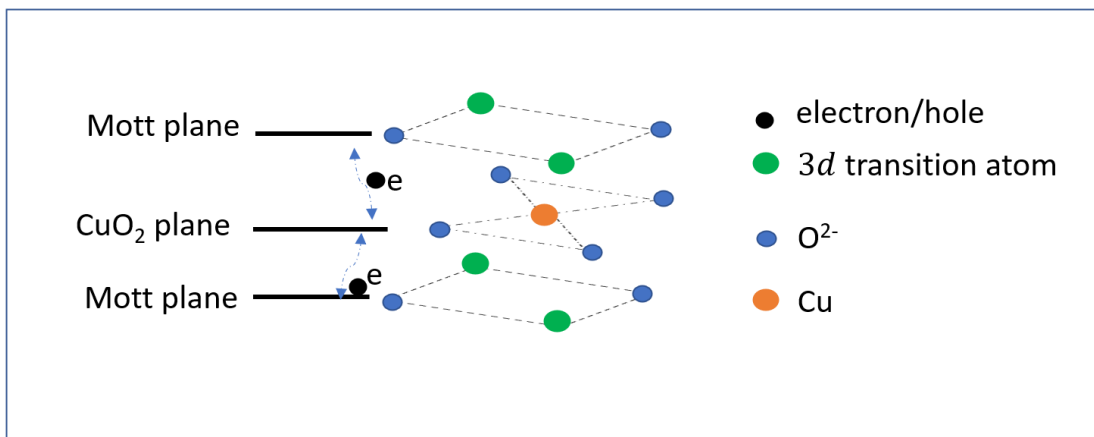


Figure 5-1 Schematic picture for Parent Mott insulator with  $\text{CuO}_2$  plane

**5.1.1. Mott Insulator.** This class of materials expected to be conductors by their electronic band structure but are insulators due to the strong Coulomb interactions among the  $3d$  band electrons. It most likely happens in the  $3d$  transition metal oxides. The

Hubbard model describes the pseudo potential caused by the coulomb repulsion and is referred to as the Hubbard bands. Its anti-ferromagnetic properties are explained through the t-J model.

The sandwiched crystal structure of oxides-based cuprate superconductors is observed by the Scanning Tunnel microscopy, as shown in Figure 5-1. It is widely believed that the Mott Insulator layers are the hole/electron dopant source for the  $\text{CuO}_2$  planes.

**5.1.2. Experiment Frontier.** Current interest in  $\text{CuO}_2$  planes is in the charge ordering and spin ordering at the superconducting states. [120] Scanning tunneling microscopy has probed the surface charges in high-temperature superconductors with bias voltage. The differential conductance ( $dI/dV$ ) was used to verify the theoretical attempts. In particular, the charge behavior on high-temperature superconductor films upon deposition is studied [121] Neutron scattering is used to study the spin texture of the  $\text{CuO}_2$  plane and shows some alternating spin patterns on the lattice positions. [122]

## 5.2. HOLE DOPING

Doping parent Mott insulators of the cuprates has been reported to induce superconductivity [123], and the concentration of dopant show a similar parabolic effect on superconductivity in the  $\text{La}_{2-x}\text{Sr}_x\text{CuO}_4$  [124] and  $\text{Ca}_{2-x}\text{Na}_x\text{CuO}_2\text{Cl}_2$  case. [125]

Figure 5-2 shows that by partial replacing  $\text{La}^{3+}$  with  $\text{Sr}^{2+}$  and  $\text{Ca}^{2+}$  with  $\text{Na}^+$ , the parent Mott insulator with  $\text{CuO}_2$  planes shows a parabolic superconductivity with sufficient hole doping. A similar scenario occurs in  $\text{CaLaBaCu}_3\text{O}_x$  when  $6.69 < x < 6.94$  [126] and in  $\text{YBaCu}_3\text{O}_y$  when  $y > 6.4$ . Additionally, with y increase (more  $\text{O}^{2-}$  as electron

acceptor), the c-axis constant decreases and enhances the superconductivity with higher critical temperature. [127]

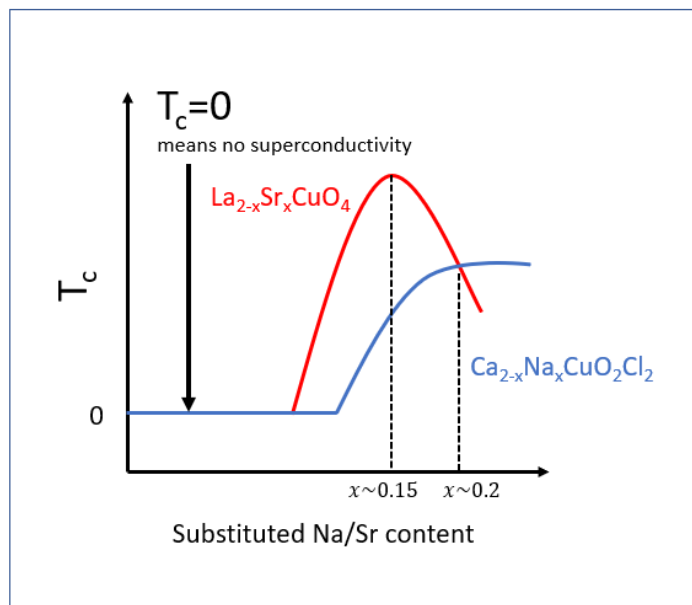


Figure 5-2 Sketch for hole doping effect on Parent Mott insulator

The electron doping effect on the  $\text{CuO}_2$  planes is also under intense investigation, particularly in  $\text{Ln}_{2-x}\text{Ce}_x\text{CuO}_4$  ( $\text{Ln}=\text{Pr}, \text{Nd}, \text{Sm}$ ) systems [128] [129]. In the n-type cuprate superconductor  $\text{Nd}_{2-x}\text{Ce}_x\text{CuO}_{4-x}$ , the superconductivity is suppressed when  $\text{Nd}^{2+}$  is substituted by  $\text{Ce}^{4+}$  or when reducing the  $\text{O}^{2-}$  concentration [130].

Although the superconductivity is enhanced by hole doping [131], several reports show that electron doping enhances the superconductivity in the iron-based high-temperature superconductor [132]. The fundamental superconductivity mechanism

between their different behavior is still a mystery, and the Hall angle may play a crucial role in the carrier-type investigation.

### 5.3. DELAFOSSITE OXIDE

Delafossite Oxide has a chemical formula of  $Cu^{1+}M^{3+}O_2^-$ . The atoms ratio for monovalent copper ( $Cu^{1+}$  and trivalent elements  $M^{3+}$  and Oxygen  $O^{2-}$  are 1:1:2.

Trivalent elements  $M^{3+}$  : Fe, Cr, and Al has been studied for their applications for solar cells and batteries. Its conductivity varies from insulating to the metallic range.

Delafossite compounds [133] belong to a family of ternary oxides. The delafossite structure consists of two alternating layers, A planar layer of Cu cations in a triangular pattern and a layer of  $MO_6$  octahedra layer normal to the c-axis. This structure has two possible space group symmetry of  $R\bar{3}m$  or  $P6$ , depending on how the two planar layers are stacking.

With the innovation of the laser ablation method, polycrystalline thin films of delafossite  $CuAlO_2$  were prepared and shows excellent p-type conductivity (up to  $1 \text{ S cm}^{-1}$ ). In addition, the thin film is transparent in the visible wavelength region with a band gap of about 3.5 eV. [134] This large band gap allows a strong electron-phonon interaction. A series of first-principal calculations were performed [135] [136] featuring a rigidly shifted Fermi level. And it suggests that, with highly p-type doping,  $CuAlO_2$ -based delafossite would be a possible transparent superconductor with  $T_c$  up to 50K.

Attempts on crystal growth for delafossite have been reported using oxidizing flux synthesis [137], wet chemical synthesis [138], spray technique [139], and

hydrothermal reactions [140]. And yet up to now, only small size thin films were produced and none of them shows superconductivity.

In this project, we start with a solid-state reaction method and create initial-new approaches to replicate the high conductivity result reported previously, including the Swagelok method and pressure seal, which are introduced in the Experiment Method section.

#### **5.4. SOLID STATE REACTION**

Stoichiometric compound  $\text{Cu}_2\text{O}$ ,  $\text{Al}_2\text{O}_3$  in the ratio of 1:1 is mixed and ground for 1 hour in the agate mortar and then compressed into a pellet at the pressure of 6Mpa using a 10mm diameter pressing die, as shown in the following Figure 5 -3.

The compressed pellet appears in dark red due to the natural color of  $\text{Cu}_2\text{O}$ , and after the sintering heating process, the pellet is visibly whitened. The sintering heating process was performed twice for individual pellets in both open-air crucible and vacuum-sealed quartz ampoules. Tracible copper color is observed in the edge of the crucible used for sintering as well as on the inner wall of the quartz ampoule.

It is plausible to surmise that the bleaching process could be the decomposition of  $\text{Cu}_2\text{O}$  into  $\text{CuO}$  and  $\text{Cu}$  on heating. Hence a second formula with  $\text{CuO}:\text{Al}_2\text{O}_3$  in the ratio of 2:1 is used with excess Oxygen atom is used. The compressed pellet appears in dark black as an immediate consequence because of the  $\text{CuO}$  black color and the pellet is greater whitened more after repeating sintering heat treatments.



Figure 5-3 Results of Traditional Solid-State Reaction

The pale sample is tested with a multimeter and the resistance reading is over 200M ohm and recorded as infinity.

Both heating temperatures are 800 degrees Celsius while the thermal decomposition of Copper (I) Oxide takes place at a temperature near 1800 degrees Celsius. [141] Thus, the copper vaporization is caused by the thermodynamic stability of  $\text{CuAlO}_2$ , it has been reported [142]. This is related to varying the partial pressure and the chemical potentials. To avoid the loss of Cu atoms in the sintering process, we decided to use the Swagelok and applied pressure on the compressed pellet.

## 5.5. PRESSURE-SEAL SWAGELOK

The pressure-seal Swagelok is introduced in Section 2.1.3. and were used in our next attempt. The pressure-seal Swagelok are heating up to 800 degrees Celsius in both open-air and vacuum-seal quartz ampoules. Visible decomposition of the external coating is observed in both situations. The sealed Swagelok nut is impossible to unlock due to the thermal expansion of the Swagelok. Inside the quartz ampoule, no visible copper vapor is noticeable.



Figure 5-4 Results of Pressure-Seal Swagelok

With the help of cutting tools, the sample pellet is extracted from the remaining. Most of the Tantalum foil is stuck to the inner wall of the Swagelok while some remained in contact with the pellet. The picture was taken and shown in Figure 5-4. It can be

inferred that the Tantalum foil shattered after the applied pressure or during the heating process.

The final pellet was measured with a multimeter and the resistance is improved to 20M ohms. The method improves the original solid-state method, but the foil used to separate the sample pellet from the inner wall needs to be another material.

## 5.6. DOUBLE-SEAL AMPOULE

The double-seal method is introduced in Section 2.1.4. and were used. The double-seal ampoule is placed in the furnace for 72 hours and the temperature was set at 700 degrees Celsius at the rate of 0.3 degrees Celsius per minute. After heating, the ampoule is cooled to room temperature at the same rate. The ampoule is then open and shown in Figure 5-5.

Without the quartz wool, the Pyrex glass ampoule melted and leaked for the sulfur gas to contaminate the sample pellet. A trace of blue  $\text{CuAlS}_2$  crystal [143] is observed after the ampoules are open. Previous studies on  $\text{CuAlS}_2$  showed that polycrystals of  $\text{CuAlS}_2$  appear in blue and our byproduct matches the color, we can infer that's the cause of the dark blue appearing on the inner Pyrex glass ampoule wall. However, with the quartz wool protection, we notice that the Pyrex glass ampoule was expanding despite the pressure from the sulfur gas and the cause of this expansion is red copper gas. This means that the thermal decomposition of the  $\text{CuAlO}_2$  is releasing more gas pressure than the sulfur we put in. This brings a dilemma between the sample size and added sulfur. The gas released from the sample is proportional to the sample size. The maximum pressure for the quartz tube is about 5 atm and this limits the amount of

sulfur added. If we cannot put any more sulfur to overwhelm the copper gas pressure, then the applied pressure on the sample pellet is very limited.

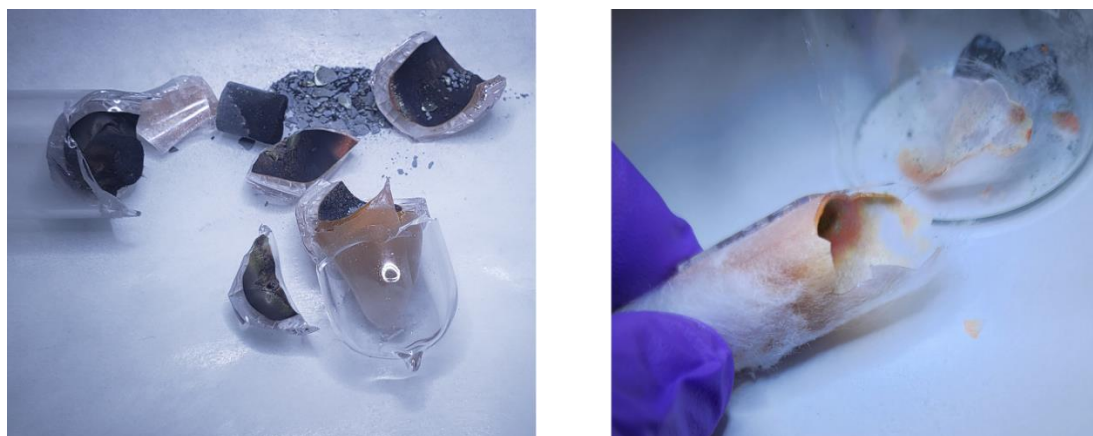


Figure 5-5 Picture of the open ampoule.

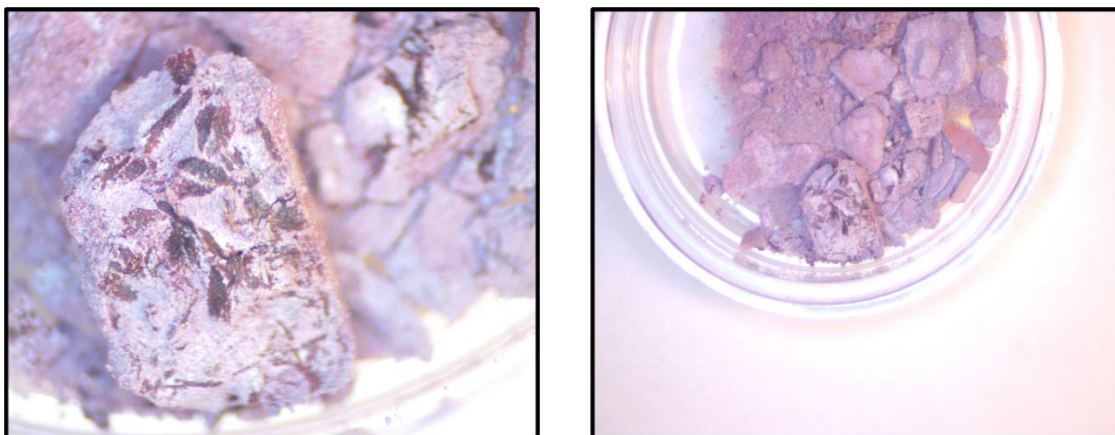


Figure 5-6 Crystals of  $\text{CuAlO}_2$

As the best result of the double seal method, the final product is shown in Figure 5-6. A red mirror-like crystal surface can be observed after the pellet is disassembled, but

the pellet is not homogeneous, and the single crystal cannot be extracted. To further improve the quality of the crystal, bigger and thicker Pyrex glass and quartz tubes could be the key. The resistance of the crystal surface can reach as low as 15M ohms.

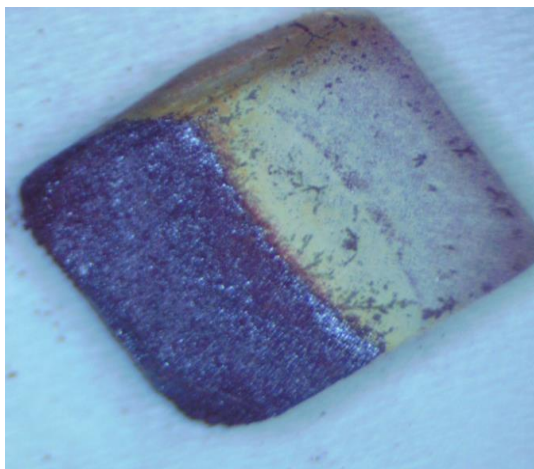


Figure 5-7 Crystals of  $\text{CuAlO}_2$  after second sintering

After the second sintering, clear polycrystals are obtained and shown in Figure 5-7. The compressing mark from the Pyrex glass ampoule is yellow and can be scratched off to reveal the polycrystal surface. The resistance of the polycrystals is measured and are still in Mega ohms region. Transparency of the polycrystals is observed and transmission behavior should be in 700-1000 nm wavelength region.

### **5.7. CRYSTAL THERMAL TRANSPORT**

In developing the method to grow the  $\text{CuAlO}_2$  delafossite crystal, the Cu gas vapor is the main obstacle to causing defect formation and leading to high resistance. The growth of delafossite is a non-equilibrium process, and to compensate for the loss of Cu

atoms, we make an important decision to increase the CuO in the original formula and have the Cu: Al atom in the ratio of 2:1. An important consideration here is that not all Cu atom will remain in the final crystals and the sufficient Cu atom will reach the formation energy while keeping in close range of Al atoms.



Figure 5-8 Results after Crystal Thermal Transport

The precursor for Crystal Thermal Transport was prepared with the solid-state sintering process 3 times to increase the polycrystal concentration. In this process, Cu vapor is generated and reaches equilibrium in a vacuum quartz ampoule and after the third sintering heating, the weight on the compressed pellet is no longer changed. The final pellet is then grounded into a fine powder and placed in the long quartz ampoule for Crystal Thermal Transport (CTT) with a temperature profile of 800-600-600 degrees Celsius for 168 hours. The Crystal thermal transport has been introduced in Section 2.

CTT-grown materials are shown in Figure 5-8 and the enlarged picture for transported crystals is shown in Figure 5-9. The transparent single-crystal film is acquired at the temperature gradient zone while some tiny single crystals are found at the cold zone. With the transport agent  $I_2$  added, the precursor becomes whole white color,

and we can infer they are the  $\text{Al}_2\text{O}_3$ . For the Cu: Al atoms 1:1 ratio sample pellet, no crystal is transported. The single crystals are flimsy, and the resistance of the films is over 200 M ohms.

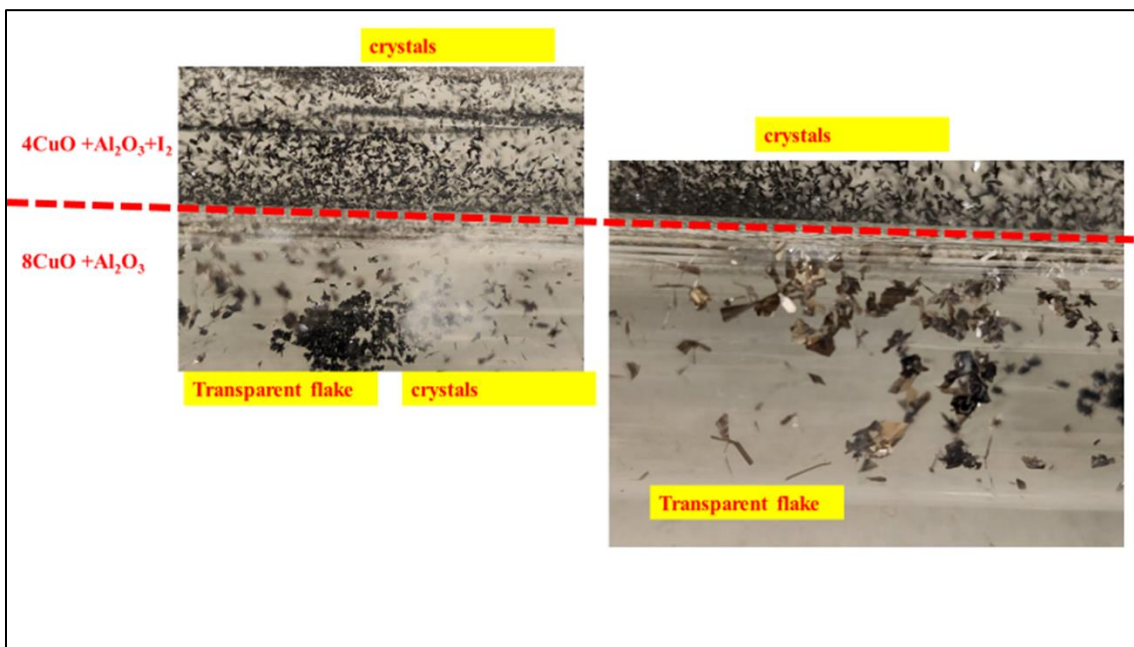


Figure 5-9 Zoomed Crystal Thermal Transport results

## 6. CONCLUSIONS

### 6.1. MAGNETIC TOPOLOGICAL INSULATOR PROJECT

This work has shown that high-quality Cr-doped  $\text{Sb}_2\text{Te}_3$  are grown using the Modified Bridgeman methods. The obtained XRD pattern shows the in-situ samples are highly crystallized and match the JCPD database for  $\text{Sb}_2\text{Te}_3$ . No structural phase change is observed from the Cr atoms. However, the cooling rate during crystallization affects the electronic properties of the Cr-doped  $\text{Sb}_2\text{Te}_3$ .

For the Magnetic properties of Cr-doped  $\text{Sb}_2\text{Te}_3$ , DC magnetization measurements are performed in both c-axis and ab-plane of the lamellar crystals. The Ferromagnetism shows isotropic behaviour, and the magnetic moment is located along the c-axis plane with a coercivity of 250 Oe at the temperature of 5K and vanishes at the temperature above 20K. Additional Cr atoms have no significant effect on the coercivity field strength, and the origin of Ferromagnetism is identified as dominating by the Bloembergen-Rowland mechanism. During crystallization, the effective magnetic moment per Cr atom varies from 2.053 (slow cooling) to 4.042 (fast cooling). The ferromagnetic to diamagnetic transition temperature is around 35 K, and a 2nd order phase transition appears with a faster cooling rate. With Te deficiency, the samples show a higher effective magnetic moment per Cr atoms.

For the Hall measurements of Cr-doped  $\text{Sb}_2\text{Te}_3$ , a slow cooling rate gives a higher zero-field Hall resistance with smaller carrier density. The Anomalous Hall effect vanishes at temperatures above 20K, and the carrier density shows no significant changes upon temperature changes at the average of  $4.7 \times 10^{20} \text{ cm}^{-3}$ . An n-type  $\text{Cr}_{0.2}\text{Sb}_2\text{Te}_3$  is

observed with a carrier density of  $-6.5 \times 10^{20} \text{ cm}^{-3}$  to  $-5.8 \times 10^{20} \text{ cm}^{-3}$  and fluctuates with temperatures. The appearance of the n-type behaviour indicates that the Te deficiency could give rise to a Quantum Anomalous Hall effect. The leading cause of the n-type formation is caused by the ratio of intercalation and substitution of Cr atoms.

## 6.2. TOPOLOGICAL SUPERCONDUCTING PROJECT

This work has shown that high-quality Nb-doped  $\text{Bi}_2\text{Se}_3$  are grown using the Modified Bridgeman methods. The obtained XRD pattern shows the in-situ samples are highly crystallized. Compared with the JCPD database for  $\text{Bi}_2\text{Se}_3$ , Nb-Se bonding is introduced, and the dopant Nb atoms are identified as intercalation. Related  $\text{NbSe}_2$  is grown using chemical vapour transport method for this project as the control group and proves the discovery is not interfered with by impurity.

The superconducting properties of Nb-doped  $\text{Bi}_2\text{Se}_3$  are confirmed by the AC Meissner effect and resistivity measurement, with the critical onset temperature of 3.6K and the critical offset temperature of 3.2K. The upper critical field is around 0.31T, and lower critical field is around 0.15T at the temperature of 2K. The coherence length is calculated from extrapolation to zero temperature for resistivity measurement. The superconductivity has an anisotropy ratio of 2, and the sample is confirmed as a type II superconductor. Respectively, our collaborators found out the angular dependence of the superconductivity shows a periodic pattern of 60

For the symbiosis state of Ferromagnetism and superconductivity, the magnetic field loop treatment successfully introduces the non-zero magnetic moment in the sample. The Cooper pairs channel model is proposed to explain the possible intrinsic mechanism.

The ARPES results confirm the Dirac surface state. At 12.8K, the Dirac point is observed at point and -0.3 eV below the Fermi level, which is located at the conduction band. Additionally, the carrier density of the sample increases with applied pressure.

For the Hall measurements of Nb-doped  $\text{Bi}_2\text{Se}_3$ , an unconventional non-zero Hall resistivity is observed within the upper critical field and behaves isotopically. The cause of this spontaneous Hall resistivity is explained with the vortex diffusion model.

### **6.3. HIGH TC SUPERCONDUCTOR PROJECT**

This work has shown several attempts at the Delafossite  $\text{CuAlO}_2$  single-crystal synthesis. The major challenge is to prevent Cu vapour generation due to thermal instability through the conventional solid-state reaction. To compensate for the Cu loss during the solid-state reaction, we used new methods to apply pressure during the heat sintering process and have a progressive result on the crystal quality and conductivity.

The pressure-seal Swagelok method provides maximum pressure on the pellet but can only produce multi-crystals. The applied pressure is uncontrollable quantitatively due to the individual modification on the Swagelok. However, the extracted sample yields the highest conductivity. Despite its difficulty to retreat the sample after sintering, the Tantalum foil is diffused and causes impurity in the system. An alternative foil would be more suitable for impurity reduction.

The double-seal ampoule method provides controllable pressure by changing the amount of additive Sulfur. Though the applied pressure is limited by the strength of the quartz ampoule, the impurity is prevented. and single crystal planes are observed after the pellet is dissembled.

A combination of conventional solid-state reaction and crystal vapour transport method is used. Additional Cu atoms are added during the grinding process to compensate for the Cu loss. The thin film of single crystals is obtained, but the number of Cu atoms cannot be controlled, and the temperature profile for crystals vapour transport may depend on the cause.

Each method has advantages and disadvantages, and the results are posted for further improvement. Table 6-1 is for the comparison of different growth methods.

Our results show that it is possible to reduce the thermal instability of the  $\text{CuAlO}_2$  by applying external pressure on the compressed pellet during the sintering heating process. We have managed to make some progress on the crystal forming with our innovative approaches. Our procedure has been described and illustrated at this stage. In all reported cases [144] we see that the crystal growth method for delafossite material does not begin to settle down until a perfect solution is available.

At this point, we have productive results to have confidence that the new methods have an effect on the applied pressure and can be used for other delafossite crystal growth. Perhaps one further improvement in the growth techniques would be the final piece of this path.

Table 6-1 Comparison of used methods

Method	Product Status	Resistance
Solid state reaction	No Crystal	>200M ohm
Pressure-seal Swagelok	Small Poly-Crystal	40M ohm
Double Sealing	Large Poly-Crystal	15M ohm
Crystal Thermal Transport	Single Crystal Film	>200M ohm

## BIBLIOGRAPHY

- [1] Y. S. Hor, A. J. Williams, J. G. Checkelsky, P. Roushan, J. Seo, Q. Xu, H. W. Zandbergen, A. Yazdani, N. P. Ong and R. J. Cava, "Superconductivity in  $\text{Cu}_x\text{Bi}_2\text{Se}_3$  and its implications for pairing in the undoped topological insulator," *Phys. Rev. Lett.*, vol. 104, p. 057001, 2010.
- [2] B. A. Volkov and O. A. Pankratov, "Two-dimensional massless electrons in an inverted contact," *Sov. Phys. JETP. Lett.*, vol. 42, p. 178, 1985.
- [3] L. Fu, C. L. Kane and E. J. Mele, "Topological insulators in three dimensions," *Phys. Rev. Lett.*, vol. 98, p. 106803, 2007.
- [4] D. Hsieh, D. Qian, L. Wray, Y. Xia, Y. S. Hor, R. J. Cava and M. Z. Hasan, "A Topological Dirac Insulator In A Quantum Spin Hall Phase," *Nature*, vol. 452, p. 970–974, 2008.
- [5] M. Z. Hasan and J. E. Moore, "Three-dimensional topological insulators," *Annu. Rev. Condens. Matter Phys.*, vol. 2, p. 55–78, 2011.
- [6] G. Du, Y. Li, J. Schneeloch, R. D. Zhong, G. Gu, H. Yang, H. Lin and H.-H. Wen, "Superconductivity With Two-fold Symmetry In Topological Superconductor  $\text{Sr}_x\text{Bi}_2\text{Se}_3$ ," *SCI. CHINA. PHYS. MECH.*, vol. 60, p. 1–6, 2017.
- [7] C.-Z. Chang, J. Zhang, X. Feng, J. Shen, Z. Zhang, M. Guo, K. Li, Y. Ou, P. Wei, L.-L. Wang and others, "Experimental Observation Of The Quantum Anomalous Hall Effect In A Magnetic Topological Insulator," *Science*, vol. 340, p. 167–170, 2013.
- [8] G. Mathys and J. O. Stenflo, "Anomalous Zeeman Effect And Its Influence On The Line Absorption And Dispersion Coefficients," *Astron Astrophys*, vol. 171, p. 368–377, 1987.
- [9] W. Tian, W. Yu, J. Shi and Y. Wang, "The Property, Preparation And Application Of Topological Insulators: A Review," *Materials*, vol. 10, p. 814, 2017.
- [10] S.-Q. Shen, W.-Y. Shan and H.-Z. Lu, "Topological Insulator And The Dirac Equation," in *Spin*, 2011.
- [11] L. Fu and C. L. Kane, "Topological insulators with inversion symmetry," *Phys Rev B*, vol. 76, p. 045302, 2007.

- [12] Y. Xia, D. Qian, D. Hsieh, L. Wray, A. Pal, H. Lin, A. Bansil, D. H. Y. S. Grauer, Y. S. Hor, R. J. Cava and others, "Observation Of A Large-gap Topological-insulator Class With A Single Dirac Cone On The Surface," *Nat. Phys.*, vol. 5, p. 398–402, 2009.
- [13] Z. Zhu, Y. Cheng and U. Schwingenschlögl, "Band Inversion Mechanism In Topological Insulators: A Guideline For Materials Design," *Phys Rev B*, vol. 85, p. 235401, 2012.
- [14] M. Zhao, X. Zhang and L. Li, "Strain-driven Band Inversion And Topological Aspects In Antimonene," *Sci. Rep.*, vol. 5, November 2015.
- [15] S. Chege, P. Ning'i, J. Sifuna and G. O. Amolo, "Origin Of Band Inversion In Topological Bi<sub>2</sub>Se<sub>3</sub>," *AIP Adv.*, vol. 10, p. 095018, 2020.
- [16] E. U. Condon, E. U. Condon and G. H. Shortley, *The theory of atomic spectra*, Cambridge University Press, 1951.
- [17] C. L. Kane and E. J. Mele, "Z<sub>2</sub> Topological Order And The Quantum Spin Hall Effect," *Phys. Rev. Lett.*, vol. 95, p. 146802, 2005.
- [18] X.-L. Qi and S.-C. Zhang, "The quantum spin Hall effect and topological insulators," *arXiv preprint arXiv:1001.1602*, 2010.
- [19] C. L. Kane and E. J. Mele, "Quantum Spin Hall Effect In Graphene," *Phys. Rev. Lett.*, vol. 95, p. 226801, 2005.
- [20] B. A. Bernevig, T. L. Hughes and S.-C. Zhang, "Quantum Spin Hall Effect And Topological Phase Transition In HgTe Quantum Wells," *Science*, vol. 314, p. 1757–1761, 2006.
- [21] Y.-M. Lin, O. Rabin, S. B. Cronin, J. Y. Ying and M. S. Dresselhaus, "Semimetal–semiconductor Transition In Bi<sub>1-x</sub>Sb<sub>x</sub> Alloy Nanowires And Their Thermoelectric Properties," *Appl. Phys. Lett.*, vol. 81, p. 2403–2405, 2002.
- [22] S. Augustine and E. Mathai, "Growth, Morphology, And Microindentation Analysis Of Bi<sub>2</sub>Se<sub>3</sub>, Bi<sub>1.8</sub>In<sub>0.2</sub>Se<sub>3</sub>, And Bi<sub>2</sub>Se<sub>2.8</sub>Te<sub>0.2</sub> Single Crystals," *Mater. Res. Bull.*, vol. 36, p. 2251–2261, 2001.
- [23] B. Büttner, C. X. Liu, G. Tkachov, E. G. Novik, C. Brüne, H. Buhmann, E. M. Hankiewicz, P. Recher, B. Trauzettel, S. C. Zhang and others, "Single Valley Dirac Fermions In Zero-gap HgTe Quantum Wells," *Nat. Phys.*, vol. 7, p. 418–422, 2011.

- [24] F. Schindler, A. M. Cook, M. G. Vergniory, Z. Wang, S. S. P. Parkin, B. A. Bernevig and T. Neupert, "Higher-order topological insulators," *Sci. Adv.*, vol. 4, p. 0346, 2018.
- [25] M. Jin, H. Shao, H. Hu, D. Li, H. Shen, J. Xu and J. Jiang, "Growth And Characterization Of Large Size Undoped P-type SnSe Single Crystal By Horizontal Bridgman Method," *J. Alloys Compd.*, vol. 712, p. 857–862, 2017.
- [26] O. Oda, *Compound Semiconductor Bulk Materials And Characterizations*, World Scientific, 2007.
- [27] Q. Zhang, Y. Xiao, T. Zhang, Z. Weng, M. Zeng, S. Yue, R. G. Mendes, L. Wang, S. Chen, M. H. Rummeli and others, "Iodine-mediated Chemical Vapor Deposition Growth Of Metastable Transition Metal Dichalcogenides," *Chem. Mater.*, vol. 29, p. 4641–4644, 2017.
- [28] W. A. Harrison, "Tunneling From An Independent-particle Point Of View," *Phys. Rev.*, vol. 123, p. 85, 1961.
- [29] A. research, "Scanning Tunneling Microscopy (STM)," Oxford Instruments, [Online]. Available: <https://afm.oxinst.com/modes/scanning-tunneling-microscopy-stm>. [Accessed 17 Jan 2023].
- [30] S. Urazhdin, D. Bilc, S. H. Tessmer, S. D. Mahanti, T. Kyratsi and M. G. Kanatzidis, "Scanning Tunneling Microscopy Of Defect States In The Semiconductor Bi<sub>2</sub>Se<sub>3</sub>," *Phys Rev B*, vol. 66, p. 161306, 2002.
- [31] C. Mann, D. West, I. Miotkowski, Y. P. Chen, S. Zhang and C.-K. Shih, "Mapping The 3d Surface Potential In Bi<sub>2</sub>Se<sub>3</sub>," *Nat. Commun.*, vol. 4, p. 1–6, 2013.
- [32] R. F. Frindt, "Superconductivity in Ultrathin NbSe<sub>2</sub> Layers," *Phys. Rev. Lett.*, vol. 28, p. 299–301, January 1972.
- [33] A. Nader, A. Briggs and Y. Gotoh, "Superconductivity in the misfit layer compounds (BiSe)<sub>1.10</sub>(NbSe<sub>2</sub>) and (BiS)<sub>1.11</sub>(NbS<sub>2</sub>)," *Solid State Commun.*, vol. 101, p. 149–153, January 1997.
- [34] D. Byrne, A. Cowley, P. McNally and E. McGlynn, "Dellafossite CuAlO<sub>2</sub> film growth and conversion to Cu–Al<sub>2</sub>O<sub>3</sub> metal ceramic composite via control of annealing atmospheres," *CrystEngComm*, vol. 15, p. 6144, 2013.

- [35] K. T. JACOB and C. B. ALCOCK, "Thermodynamics of  $\text{CuAlO}_2$  and  $\text{CuAl}_2\text{O}_4$  and Phase Equilibria in the System  $\text{Cu}_2\text{O-CuO-Al}_2\text{O}_3$ ," *J. Am. Ceram. Soc.*, vol. 58, p. 192–195, May 1975.
- [36] R. W. G. Wyckoff, *Crystal Structures*, Krieger, Malabar, 1986.
- [37] B. Lv, T. Qian and H. Ding, "Angle-resolved Photoemission Spectroscopy And Its Application To Topological Materials," *Nature Reviews Physics*, vol. 1, p. 609–626, 2019.
- [38] V. N. Strocov, M. Shi, M. Kobayashi, C. Monney, X. Wang, J. Krempasky, T. Schmitt, L. Patthey, H. Berger and P. Blaha, "Three-dimensional Electron Realm In Vse 2 By Soft-x-ray Photoelectron Spectroscopy: Origin Of Charge-density Waves," *Phys. Rev. Lett.*, vol. 109, p. 086401, 2012.
- [39] Y. Tokura, K. Yasuda and A. Tsukazaki, "Magnetic Topological Insulators," *Nature Reviews Physics*, vol. 1, p. 126–143, 2019.
- [40] Q. Liu, C.-X. Liu, C. Xu, X.-L. Qi and S.-C. Zhang, "Magnetic Impurities On The Surface Of A Topological Insulator," *Phys. Rev. Lett.*, vol. 102, p. 156603, 2009.
- [41] D. A. Abanin and D. A. Pesin, "Ordering Of Magnetic Impurities And Tunable Electronic Properties Of Topological Insulators," *Phys. Rev. Lett.*, vol. 106, p. 136802, 2011.
- [42] R. Yu, W. Zhang, H.-J. Zhang, S.-C. Zhang, X. Dai and Z. Fang, "Quantized Anomalous Hall Effect in Magnetic Topological Insulators," *Science*, vol. 329, p. 61–64, July 2010.
- [43] J.-J. Zhu, D.-X. Yao, S.-C. Zhang and K. Chang, "Electrically Controllable Surface Magnetism On The Surface Of Topological Insulators," *Phys. Rev. Lett.*, vol. 106, p. 097201, 2011.
- [44] Y. S. Hor, P. Roushan, H. Beidenkopf, J. Seo, D. Qu, J. G. Checkelsky, L. A. Wray, D. Hsieh, Y. Xia, S.-Y. Xu and others, "Development Of Ferromagnetism In The Doped Topological Insulator  $\text{Bi}_2\text{-X Mn X Te}_3$ ," *Phys Rev B*, vol. 81, p. 195203, 2010.
- [45] J. Teng, N. Liu and Y. Li, "Mn-doped Topological Insulators: A Review," *J. Semicond.*, vol. 40, p. 081507, August 2019.
- [46] K. Nomura and N. Nagaosa, "Surface-quantized Anomalous Hall Current And The Magnetoelectric Effect In Magnetically Disordered Topological Insulators," *Phys. Rev. Lett.*, vol. 106, p. 166802, 2011.

- [47] M. Z. Hasan and C. L. Kane, "Colloquium: Topological Insulators," *Rev. Mod. Phys.*, vol. 82, p. 3045, 2010.
- [48] N. Nagaosa, J. Sinova, S. Onoda, A. H. MacDonald and N. P. Ong, "Anomalous hall effect," *Rev. Mod. Phys.*, vol. 82, p. 1539, 2010.
- [49] R. Karplus and J. M. Luttinger, "Hall Effect In Ferromagnetics," *Phys. Rev.*, vol. 95, p. 1154, 1954.
- [50] J. Smit, "The Spontaneous Hall Effect In Ferromagnetics I," *Physica*, vol. 21, p. 877–887, 1955.
- [51] J. Smit, "The Spontaneous Hall Effect In Ferromagnetics II," *Physica*, vol. 24, p. 39–51, 1958.
- [52] L. Berger, "Side-jump Mechanism For The Hall Effect Of Ferromagnets," *Phys. Rev. B*, vol. 2, p. 4559, 1970.
- [53] J. Kondo, "Resistance Minimum In Dilute Magnetic Alloys," *Prog. Theor. Phys.*, vol. 32, p. 37–49, 1964.
- [54] D. Culcer, "The Anomalous Hall Effect," *arXiv:2204.02434*, 2022.
- [55] K. L. Tiwari, W. A. Coish and T. Pereg-Barnea, "Magnetoeconductance Signatures Of Chiral Domain-wall Bound States In Magnetic Topological Insulators," *Phys. Rev. B*, vol. 96, p. 235120, December 2017.
- [56] C. Liu, Y. Ou, Y. Feng, G. Jiang, W. Wu, S. Li, Z. Cheng, K. He, X. Ma, Q. Xue and Y. Wang, "Distinct Quantum Anomalous Hall Ground States Induced by Magnetic Disorders," *Phys. Rev. X*, vol. 10, p. 041063, December 2020.
- [57] K. von Klitzing, "Essay: Quantum Hall Effect And The New International System Of Units," *Phys. Rev. Lett.*, vol. 122, p. 200001, 2019.
- [58] o. K. Likharev, *Essential Graduate Physics-Quantum Mechanics*, Stony Brook University, 2020.
- [59] D. J. Thouless, M. Kohmoto, M. P. Nightingale and M. den Nijs, "Quantized Hall Conductance In A Two-dimensional Periodic Potential," *Phys. Rev. Lett.*, vol. 49, p. 405, 1982.
- [60] D. Xiao, J. Shi and Q. Niu, "Berry Phase Correction To Electron Density Of States In Solids," *Phys. Rev. Lett.*, vol. 95, p. 137204, 2005.

- [61] F. D. M. Haldane, "Model For A Quantum Hall Effect Without Landau Levels: Condensed-matter Realization Of The" Parity Anomaly", " *Phys. Rev. Lett.*, vol. 61, p. 2015, 1988.
- [62] J. E. Hirsch, "Spin Hall Effect," *Phys. Rev. Lett.*, vol. 83, p. 1834–1837, August 1999.
- [63] M. König, S. Wiedmann, C. Brüne, A. Roth, H. Buhmann, L. W. Molenkamp, X.-L. Qi and S.-C. Zhang, "Quantum Spin Hall Insulator State In HgTe Quantum Wells," *Science*, vol. 318, p. 766–770, November 2007.
- [64] C.-X. Liu, X.-L. Qi, X. Dai, Z. Fang and S.-C. Zhang, "Quantum Anomalous Hall Effect In Hg 1- Y Mn Y Te Quantum Wells," *Phys. Rev. Lett.*, vol. 101, p. 146802, 2008.
- [65] X.-L. Qi, Y.-S. Wu and S.-C. Zhang, "Topological Quantization Of The Spin Hall Effect In Two-dimensional Paramagnetic Semiconductors," *Phys. Rev. B*, vol. 74, p. 085308, 2006.
- [66] S. Murakami, N. Nagaosa and S.-C. Zhang, "Spin-hall Insulator," *Phys. Rev. Lett.*, vol. 93, p. 156804, 2004.
- [67] S. Zhang, Z. Li, X. Pan, X. Wang and F. Song, "Anomalous Hall study of magnetic topological insulator Cr<sub>0.15</sub>(Bi<sub>0.1</sub>Sb<sub>0.9</sub>)<sub>1.85</sub>Te<sub>3</sub> microflakes," *Solid State Commun.*, vol. 223, p. 45–49, 2015.
- [68] R. Daou, H. Takahashi, S. Hébert, M. Beaumale, E. Guilmeau and A. Maignan, "Intrinsic effects of substitution and intercalation on thermal transport in two-dimensional {TiS}<sub>2</sub> single crystals," *J. Appl. Phys.*, vol. 117, p. 165101, April 2015.
- [69] S. Mugiraneza and A. M. Hallas, "Tutorial: A Beginner's Guide To Interpreting Magnetic Susceptibility Data With The Curie-weiss Law," *Commun. Phys.*, vol. 5, April 2022.
- [70] C.-Z. Chang, J. Zhang, M. Liu, Z. Zhang, X. Feng, K. Li, L.-L. Wang, X. Chen, X. Dai, Z. Fang, X.-L. Qi, S.-C. Zhang, Y. Wang, K. He, X.-C. Ma and Q.-K. Xue, "Thin Films of Magnetically Doped Topological Insulator with Carrier-Independent Long-Range Ferromagnetic Order," *Adv. Mater.*, vol. 25, p. 1065–1070, January 2013.
- [71] A. J. Bestwick, E. J. Fox, X. Kou, L. Pan, K. L. Wang and D. Goldhaber-Gordon, "Precise Quantization Of The Anomalous Hall Effect Near Zero Magnetic Field," *Phys. Rev. Lett.*, vol. 114, p. 187201, 2015.

- [72] D. Hsieh, Y. Xia, D. Qian, L. Wray, F. Meier, J. H. Dil, J. Osterwalder, L. Patthey, A. V. Fedorov, H. Lin and others, "Observation Of Time-reversal-protected Single-dirac-cone Topological-insulator States In Bi<sub>2</sub>Te<sub>3</sub> And Sb<sub>2</sub>Te<sub>3</sub>," *Phys. Rev. Lett.*, vol. 103, p. 146401, 2009.
- [73] H. Zou, D. M. Rowe and G. Min, "Preparation And Characterization Of P-type Sb<sub>2</sub>Te<sub>3</sub> And N-type Bi<sub>2</sub>Te<sub>3</sub> Thin Films Grown By Coevaporation," *J. Vac. Sci. Technol. A: Vac. Surf. Films*, vol. 19, p. 899–903, 2001.
- [74] L. R. Testardi, J. N. Bierly Jr and F. J. Donahoe, "Transport Properties Of P-type Bi<sub>2</sub>Te<sub>3</sub>□Sb<sub>2</sub>Te<sub>3</sub> Alloys In The Temperature Range 80–370° K," *J. Phys. Chem. Solids*, vol. 23, p. 1209–1217, 1962.
- [75] S. Kittaka, R. Fujinaga, K. Morishige and T. Morimoto, "Adsorption of water on the surfaces of α-HCrO<sub>2</sub> and Cr<sub>2</sub>O<sub>3</sub>," *J. Colloid Interface Sci.*, vol. 102, p. 453–461, 1984.
- [76] D. De Cogan, "Carrier Mobility In Cr<sub>2</sub>O<sub>3</sub>," *J. Phys. Chem. Solids*, vol. 38, p. 333–334, 1977.
- [77] N. Sakai, T. Kajiwara, K. Takemura, S. Minomura and Y. Fujii, "Pressure-induced Phase Transition In Sb<sub>2</sub>Te<sub>3</sub>," *Solid State Commun.*, vol. 40, p. 1045–1047, 1981.
- [78] H. Tian, C. Xu, X. Li, Y. Yang, L. Bellaiche and D. Wu, "Band Structure Engineering Of Van Der Waals Heterostructures Using Ferroelectric Clamped Sandwich Structures," *Phys Rev B*, vol. 103, p. 125426, 2021.
- [79] M. Shamsuddin, A. Nasar and V. B. Tare, "Electrical Conductivity Of Tellurium Deficient Cadmium Telluride," *J. Appl. Phys.*, vol. 74, p. 6208–6211, 1993.
- [80] M. Sato and Y. Ando, "Topological Superconductors: A Review," *Rep. Prog. Phys.*, vol. 80, p. 076501, 2017.
- [81] F. Wilczek, "Majorana Returns," *Nat. Phys.*, vol. 5, p. 614–618, 2009.
- [82] N. Read and D. Green, "Paired states of fermions in two dimensions with breaking of parity and time-reversal symmetries and the fractional quantum Hall effect," *Phys Rev B*, vol. 61, p. 10267, 2000.
- [83] H. K. Onnes, "The Superconductivity of Mercury," *Commun. Phys. Lab. Univ. Leiden, Nos.*, vol. 119, pp. 122-124, 1991.

- [84] W. Meissner and R. Ochsenfeld, "Ein neuer Effekt bei Eintritt der Supraleitfähigkeit," *Die Naturwissenschaften*, vol. 21, p. 787–788, November 1933.
- [85] M. Tinkham, *Introduction To Superconductivity* (second Edition), McGraw-Hill, 1996.
- [86] C. Kittel, P. McEuen and P. McEuen, *Introduction To Solid State Physics*, vol. 8, Wiley New York, 1996.
- [87] L. A. Pérez, J. S. Millán and C. Wang, "A Unified Description Of S-, P- And D-wave Superconductivity," *Phys. B: Condens. Matter*, Vols. 359-361, p. 569–571, April 2005.
- [88] A. P. Mackenzie and Y. Maeno, "P-wave Superconductivity," *Phys. B: Condens. Matter*, vol. 280, p. 148–153, May 2000.
- [89] R. C. Morris and R. V. Coleman, "Anisotropic Superconductivity In Layer Compounds," *Phys Rev B*, vol. 7, p. 991, 1973.
- [90] M. D. Lan, J. Z. Liu, Y. X. Jia, L. Zhang, Y. Nagata, P. Klavins and R. N. Shelton, "Resistivity And Upper Critical Field Of  $Yb_{1-x}Cu_3-xFe_xO_{7-y}$  Single Crystals," *Phys Rev B*, vol. 47, p. 457, 1993.
- [91] R. C. Morris, R. V. Coleman and R. Bhandari, "Superconductivity And Magnetoresistance In  $NbSe_2$ ," *Phys Rev B*, vol. 5, p. 895, 1972.
- [92] T. Asaba, B. J. Lawson, C. Tinsman, L. Chen, P. Corbae, G. Li, Y. Qiu, Y. S. Hor, L. Fu and L. Li, "Rotational Symmetry Breaking In A Trigonal Superconductor Nb-doped  $Bi_2Se_3$ ," *Phys. Rev. X*, vol. 7, p. 011009, 2017.
- [93] H. Zhang, C.-X. Liu, X.-L. Qi, X. Dai, Z. Fang and S.-C. Zhang, "Topological insulators in  $Bi_2Se_3$ ,  $Bi_2Te_3$  and  $Sb_2Te_3$  with a single Dirac cone on the surface," *Nat. Phys.*, vol. 5, p. 438–442, 2009.
- [94] M. P. Smylie, K. Willa, K. Ryan, H. Claus, W.-K. Kwok, Y. Qiu, Y. S. Hor and U. Welp, "An Increase In  $T_c$  Under Hydrostatic Pressure In The Superconducting Doped Topological Insulator  $Nb_{0.25}Bi_{2.75}Se_3$ ," *Phys. C: Supercond. Its Appl.*, vol. 543, p. 58–61, 2017.
- [95] L. A. Wray, S.-Y. Xu, Y. Xia, Y. S. Hor, D. Qian, A. V. Fedorov, H. Lin, A. Bansil, R. J. Cava and M. Z. Hasan, "Observation of topological order in a superconducting doped topological insulator," *Nat. Phys.*, vol. 6, p. 855–859, 2010.

- [96] L. Fu and E. Berg, "Odd-parity topological superconductors: theory and application to  $\text{Cu}_x\text{Bi}_{2-x}\text{Se}_3$ ," *Phys. Rev. Lett.*, vol. 105, p. 097001, 2010.
- [97] Y. Qiu, K. N. Sanders, J. Dai, J. E. Medvedeva, W. Wu, P. Ghaemi, T. Vojta and Y. S. Hor, "Time Reversal Symmetry Breaking Superconductivity In Topological Materials," *arXiv*, 2015.
- [98] R. Jha, R. Goyal, P. Neha, V. K. Maurya, A. K. Srivastava, A. Gupta, S. Patnaik and V. P. S. Awana, "Weak Ferromagnetism In A Noncentrosymmetric Bipd 4 K Superconductor," *Supercond. Sci. Technol.*, vol. 29, p. 025008, 2015.
- [99] S.-M. Choi, J. W. Lynn, D. Lopez, P. L. Gammel, P. C. Canfield and S. L. Bud'Ko, "Direct Observation Of Spontaneous Weak Ferromagnetism In The Superconductor  $\text{ErNi}_2\text{B}_2\text{C}$ ," *Phys. Rev. Lett.*, vol. 87, p. 107001, 2001.
- [100] C. M. Puetter and H.-Y. Kee, "Identifying spin-triplet pairing in spin-orbit coupled multi-band superconductors," *EPL (Europhysics Letters)*, vol. 98, p. 27010, 2012.
- [101] Y. Iye, S. Nakamura and T. Tamegai, "Hall effect in high temperature superconductors near  $T_c$ ," *Phys. C: Supercond. Appl.*, vol. 159, p. 616–624, 1989.
- [102] X. Zhu, H. Yang, L. Fang, G. Mu and H.-H. Wen, "Upper Critical Field, Hall Effect And Magnetoresistance In The Iron-based Layered Superconductor  $\text{LaFeAsO}_{0.9f0.1-\delta}$ ," *Supercond. Sci. Technol.*, vol. 21, p. 105001, 2008.
- [103] X. C. Yang, X. Luo, J. J. Gao, Z. Z. Jiang, W. Wang, T. Y. Wang, J. G. Si, C. Y. Xi, W. H. Song and Y. P. Sun, "Planar Hall Effect In The Quasi-one-dimensional Topological Superconductor  $\text{TaSe}_3$ ," *Phys Rev B*, vol. 104, p. 155106, 2021.
- [104] D. LeBoeuf, N. Doiron-Leyraud, B. Vignolle, M. Sutherland, B. J. Ramshaw, J. Levallois, R. Daou, F. Laliberté, O. Cyr-Choiniere, J. Chang and others, "Lifshitz Critical Point In The Cuprate Superconductor  $\text{YBa}_2\text{Cu}_3\text{O}_Y$  From High-field Hall Effect Measurements," *Phys Rev B*, vol. 83, p. 054506, 2011.
- [105] W. A. Reed, E. Fawcett and Y. B. Kim, "Observation Of The Hall Effect In Superconductors," *Phys. Rev. Lett.*, vol. 14, p. 790, 1965.
- [106] T. Senthil, J. B. Marston and M. P. A. Fisher, "Spin Quantum Hall Effect In Unconventional Superconductors," *Phys Rev B*, vol. 60, p. 4245, 1999.
- [107] F.-C. Zhang, "Superconductivity In  $\text{CuO}_2$  Monolayer On Cuprate Substrates," *Sci. Bull.*, vol. 61, p. 1236–1238, 2016.

- [108] L.-F. Zhang, L. Covaci and M. V. Milošević, "Topological Phase Transitions In Small Mesoscopic Chiral P-wave Superconductors," *Phys. Rev.B*, vol. 96, p. 224512, 2017.
- [109] J. Bardeen and M. J. Stephen, "Theory of the motion of vortices in superconductors," *Phys. Rev. Lett.*, vol. 140, p. 1197, 1965.
- [110] G. Blatter, M. V. Feigel'man, V. B. Geshkenbein, A. I. Larkin and V. M. Vinokur, "Vortices In High-temperature Superconductors," *Rev. Mod. Phys.*, vol. 66, p. 1125, 1994.
- [111] L. N. Cooper and D. Feldman, *Bcs: 50 Years*, World scientific, 2010.
- [112] Y. Kamihara, T. Watanabe, M. Hirano and H. Hosono, "Iron-based layered superconductor La [O<sub>1-x</sub> F<sub>x</sub>] FeAs (x= 0.05- 0.12) with T<sub>c</sub>= 26 K," *J. Am. Chem. Soc.*, vol. 130, p. 3296–3297, 2008.
- [113] G. Burns, *High-temperature superconductivity*, San Diego, CA (United States); Academic Press Inc., 1992.
- [114] C. Q. Choi, "Iron Exposed as High-Temperature Superconductor," *Sci. Am.*, 2008.
- [115] J. G. Bednorz and K. A. Müller, "Possible High T<sub>c</sub> Superconductivity In The Ba-La- Cu- O System," *Z. PHYS. B CON. MAT.*, vol. 64, p. 189–193, 1986.
- [116] I. Vishik, "A coexistence that CuO<sub>2</sub> planes can see," *Science*, vol. 369, p. 775–776, 2020.
- [117] G. Balestrino, S. Barbanera and P. Paroli, "Growth Of Single Crystals Of The High-temperature Superconductor Yba<sub>2</sub>cu<sub>3</sub>o<sub>7-x</sub>," *J. Cryst. Growth*, vol. 85, p. 585–587, 1987.
- [118] R. T. Collins, Z. Schlesinger, G. V. Chandrashekhar and M. W. Shafer, "Infrared Study Of Anisotropy In Single-crystal La 2- X Sr X Cu O 4," *Phys. Rev. B*, vol. 39, p. 2251, 1989.
- [119] T. Ito, H. Takagi, S. Ishibashi, T. Ido and S. Uchida, "Normal-state Conductivity Between CuO<sub>2</sub> Planes In Copper Oxide Superconductors," *Nature*, vol. 350, p. 596–598, 1991.
- [120] B. G. Levi, "New Experiments Highlight Universal Behavior In Copper Oxide Superconductors.," *Phys. Today*, vol. 57, p. 24–27, 2004.

- [121] Y. Zhong, Y. Wang, S. Han, Y.-F. Lv, W.-L. Wang, D. Zhang, H. Ding, Y.-M. Zhang, L. Wang, K. He and others, "Nodeless Pairing In Superconducting Copper-oxide Monolayer Films On  $\text{Bi}_2\text{Sr}_2\text{CaCu}_2\text{O}_{8+\delta}$ ," *Sci. Bull.*, vol. 61, p. 1239–1247, 2016.
- [122] J. Rossat-Mignod, L. P. Regnault, C. Vettier, P. Bourges, P. Burllet, J. Bossy, J. Y. Henry and G. Lapertot, "Neutron Scattering Study Of The  $\text{YBa}_2\text{Cu}_3\text{O}_{6+X}$  System," *Physica C Supercond.*, vol. 185, p. 86–92, 1991.
- [123] P. Cai, W. Ruan, Y. Peng, C. Ye, X. Li, Z. Hao, X. Zhou, D.-H. Lee and Y. Wang, "Visualizing the evolution from the Mott insulator to a charge-ordered insulator in lightly doped cuprates," *Nature Physics*, vol. 12, p. 1047–1051, 2016.
- [124] J. B. Torrance, A. Bezingue, A. I. Nazzari, T. C. Huang, S. S. P. Parkin, D. T. Keane, S. J. LaPlaca, P. M. Horn and G. A. Held, "Properties That Change As Superconductivity Disappears At High-doping Concentrations In  $\text{La}_{2-x}\text{Sr}_x\text{CuO}_4$ ," *Phys. Rev. B*, vol. 40, p. 8872, 1989.
- [125] C. Ye, P. Cai, R. Yu, X. Zhou, W. Ruan, Q. Liu, C. Jin and Y. Wang, "Visualizing The Atomic-scale Electronic Structure Of The  $\text{Ca}_2\text{CuO}_2\text{Cl}_2$  Mott Insulator," *Nat. Commun.*, vol. 4, p. 1–7, 2013.
- [126] S. Katano, K. Yamaya, J. A. Fernandez-Baca and S. Funahashi, "Crystal Structure Of The Tetragonal Superconductor  $\text{Ca}_{1-x}\text{Ba}_x\text{Cu}_3\text{O}_7$  ( $6.69 \leq x \leq 6.94$ )," *Physica C Supercond.*, vol. 217, p. 73–78, 1993.
- [127] H. Y. Zhai, Z. H. Zhang and W. K. Chu, "Accurate Comparative Measurement Of Oxygen Content Variations In  $\text{YBa}_2\text{Cu}_3\text{O}_{7-\delta}$  Films Due To Postdeposition Annealing," *Appl. Phys. Lett.*, vol. 78, p. 649–651, 2001.
- [128] E. M. & R. L. G. P. Fournier, Current Research Issues for the Electron-Doped Cuprates, Part of the NATO Science Series: B: book series (NSSB, volume 371).
- [129] M. A. Crusellas, J. Fontcuberta, S. Piñol, J. Beille and T. Grenet, "Transport Properties Of  $\text{Ln}_{2-x}\text{Ce}_x\text{CuO}_{4-y}$  Single Crystals Under High Pressure," *Physica C Supercond.*, vol. 209, p. 537–548, 1993.
- [130] H. Takagi, S. Uchida and Y. Tokura, "Superconductivity Produced By Electron Doping In  $\text{CuO}$  2-layered Compounds," *Phys. Rev. Lett.*, vol. 62, p. 1197, 1989.
- [131] Y. Dagan and R. L. Greene, "Hole Superconductivity In The Electron-doped Superconductor  $\text{Pr}_{2-x}\text{Ce}_x\text{CuO}_4$ ," *Phys. Rev. B*, vol. 76, p. 024506, 2007.

- [132] X. Shi, Z. Q. Han, X. L. Peng, P. Richard, T. Qian, X. X. Wu, M. W. Qiu, S. C. Wang, J. P. Hu, Y. J. Sun and others, "Enhanced Superconductivity Accompanying A Lifshitz Transition In Electron-doped Fese Monolayer," *Nat. Commun.*, vol. 8, p. 1–6, 2017.
- [133] M. A. Marquardt, N. A. Ashmore and D. P. Cann, "Crystal Chemistry And Electrical Properties Of The Delafossite Structure," *Thin Solid Films*, vol. 496, p. 146–156, 2006.
- [134] H. Kawazoe, M. Yasukawa, H. Hyodo, M. Kurita, H. Yanagi and H. Hosono, "P-type electrical conduction in transparent thin films of CuAlO<sub>2</sub>," *Nature*, vol. 389, p. 939–942, 1997.
- [135] J. Pellicer-Porres, A. Segura, A. S. Gilliland, A. Munoz, P. Rodríguez-Hernández, D. Kim, M. S. Lee and T. Y. Kim, "On The Band Gap Of Cualo<sub>2</sub> Delafossite," *Appl. Phys. Lett.*, vol. 88, p. 181904, 2006.
- [136] A. Nakanishi and H. Katayama-Yoshida, "Computational Materials Design For Superconductivity In Hole-doped Delafossite Cualo<sub>2</sub>: Transparent Superconductors," *Solid State Commun.*, vol. 152, p. 24–27, 2012.
- [137] J. S. Yoon, Y. S. Nam, K. S. Baek, C. W. Park, H. L. Ju and S. K. Chang, "Growth And Properties Of Transparent Conducting Cualo<sub>2</sub> Single Crystals By A Flux Self-removal Method," *J. Cryst. Growth.*, vol. 366, p. 31–34, 2013.
- [138] Z. Deng, X. Zhu, R. Tao, W. Dong and X. Fang, "Synthesis Of Cualo<sub>2</sub> Ceramics Using Sol-gel," *Mater. Lett.*, vol. 61, p. 686–689, 2007.
- [139] C. Bouzidi, H. Bouzouita, A. Timoumi and B. Rezig, "Fabrication And Characterization Of Cualo<sub>2</sub> Transparent Thin Films Prepared By Spray Technique," *Mater. Sci. Eng. B*, vol. 118, p. 259–263, 2005.
- [140] S. Gao, Y. Zhao, P. Gou, N. Chen and Y. Xie, "Preparation Of Cualo<sub>2</sub> Nanocrystalline Transparent Thin Films With High Conductivity," *Nanotechnology*, vol. 14, p. 538, 2003.
- [141] F. Yi, J. B. DeLisio, N. Nguyen, M. R. Zachariah and D. A. LaVan, "High Heating Rate Decomposition Dynamics Of Copper Oxide By Nanocalorimetry-coupled Time-of-flight Mass Spectrometry," *Chem. Phys. Lett.*, vol. 689, p. 26–29, 2017.
- [142] D. O. Scanlon and G. W. Watson, "Conductivity Limits In Cualo<sub>2</sub> From Screened-hybrid Density Functional Theory," *J. Phys. Chem. Lett.*, vol. 1, p. 3195–3199, 2010.

- [143] L. Roa, J. C. Chervin, J. P. Itie, A. Polian, M. Gauthier and A. Chevy, "High-pressure Structural Study Of CuAlS<sub>2</sub> And CuAlSe<sub>2</sub>," *Physica Status Solidi (b)*, vol. 211, p. 455–459, 1999.
- [144] A. P. Mackenzie, "The Properties Of Ultrapure Delafossite Metals," *Rep. Prog. Phys.*, vol. 80, p. 032501, 2017.
- [145] Y. S. Hor, A. Richardella, P. Roushan, Y. Xia, J. G. Checkelsky, A. Yazdani, M. Z. Hasan, N. P. Ong and R. J. Cava, "P-type Bi<sub>2</sub>Se<sub>3</sub> For Topological Insulator And Low-temperature Thermoelectric Applications," *Phys Rev B*, vol. 79, p. 195208, 2009.
- [146] W. A. Harrison, "Tunneling from an Independent-Particle Point of View," *Phys. Rev.*, vol. 123, p. 85–89, July 1961.
- [147] C.-Z. Chang, W. Zhao, J. Li, J. Jain, C. Liu, J. S. Moodera and M. H. Chan, "Observation of the Quantum Anomalous Hall Insulator to Anderson Insulator Quantum Phase Transition and its Scaling Behavior," *Phys. Rev. Lett.*, vol. 117, p. 126802, September 2016.
- [148] S. Chikazumi and C. D. Graham, *Physics Of Ferromagnetism*, Oxford university press, 1997.
- [149] R. J. Cava, B. Batlogg, R. B. Van Dover, D. W. Murphy, S. Sunshine, T. Siegrist, J. P. Remeika, E. A. Rietman, S. Zahurak and G. P. Espinosa, "Bulk Superconductivity At 91 K In Single-phase Oxygen-deficient Perovskite Ba<sub>2</sub>YCu<sub>3</sub>O<sub>9- $\delta$</sub> ," *Phys. Rev. Lett.*, vol. 58, p. 1676, 1987.

## VITA

Yunsheng Qiu was in China, Guangdong Province, Lufeng city, Jiazi town. He was relocated by his family to Guangzhou, which is one of the major port cities in Southeast China and received elementary education. He received his pre-college educations from the Affiliated High School of South China Normal University in 2010. He received a Bachelor of Science in Physics from Missouri University of Science and Technology in May 2014 and a Bachelor of Engineering in Composite Materials and Engineering from Harbin Institute of Technology in June 2016 through the double degree program hosted by these two universities. In August 2015, he began his Ph.D in Physics under the guidance of Dr. Yew San Hor at Missouri University of Science and Technology. In May 2023, Yunsheng Qiu was awarded his Ph.D. degree in Physics from Missouri University of Science and Technology.